

2014-01-01

Characterization of High-purity Niobium Structures Fabricated Using the Electron Beam Melting Process

Cesar Adrian Terrazas

University of Texas at El Paso, caterrazas2@miners.utep.edu

Follow this and additional works at: https://digitalcommons.utep.edu/open_etd

 Part of the [Materials Science and Engineering Commons](#), [Mechanical Engineering Commons](#), and the [Mechanics of Materials Commons](#)

Recommended Citation

Terrazas, Cesar Adrian, "Characterization of High-purity Niobium Structures Fabricated Using the Electron Beam Melting Process" (2014). *Open Access Theses & Dissertations*. 1360.
https://digitalcommons.utep.edu/open_etd/1360

This is brought to you for free and open access by DigitalCommons@UTEP. It has been accepted for inclusion in Open Access Theses & Dissertations by an authorized administrator of DigitalCommons@UTEP. For more information, please contact lweber@utep.edu.

CHARACTERIZATION OF HIGH-PURITY NIOBIUM STRUCTURES FABRICATED USING THE ELECTRON BEAM MELTING PROCESS

César Adrián Terrazas Nájera, M.S.M.E.

Materials Science and Engineering

APPROVED:

Ryan B. Wicker, Ph.D. Chair

Lawrence E. Murr, Ph.D.

Eric MacDonald, Ph.D.

Russell R. Chianelli, Ph.D.

Cristian E. Botez, Ph.D.

Charles Ambler, Ph.D.
Dean of the Graduate School

Copyright ©

by

César Adrián Terrazas Nájera

2014

Dedication

To all my Family, to my wife Viviana, and to my little angel Miranda

CHARACTERIZATION OF HIGH-PURITY NIOBIUM STRUCTURES
FABRICATED USING THE ELECTRON BEAM MELTING PROCESS

by

CÉSAR ADRIÁN TERRAZAS NÁJERA, M.S.M.E

DISSERTATION

Presented to the Faculty of the Graduate School of

The University of Texas at El Paso

in Partial Fulfillment

of the Requirements

for the Degree of

DOCTOR OF PHILOSOPHY

Materials Science and Engineering

THE UNIVERSITY OF TEXAS AT EL PASO

August 2014

Acknowledgements

Many people have made the work presented here possible.

First of all, I would like to express my infinite gratitude for my nuclear Family as they always supported this dream starting more than a decade ago in 2002. The financial assistance as well as emotional support during difficult times were fundamental to reach this goal. To my parents Miguel and Araceli for allowing me to pursue this dream even when the economic situation of the family was hard. My parents also deserve recognition for taking care of me when illness seemed to put a halt to this path I was following. Gracias Mamá! I also express gratitude to my siblings Miguel, Carina and Chely for their support in many aspects of life during my time as a doctoral student. I would like to also acknowledge my wife Viviana for her patience, encouragement and emotional support and for giving me the greatest joy I have in life so far; that of being a father.

I express my most sincere gratitude and respect to Dr. Ryan Wicker and Dr. Francisco Medina for providing me with the utmost opportunity of becoming a researcher at the Keck Center and for providing financial support during my time in this amazing place. Very sincere thanks to many of my fellow students and researchers at the Keck for making this possible; to Sara Gaytan, Jorge Mireles and David Espalin for providing words of support when I needed them most. Thanks to Jonathan Minjares and Carmen Rocha for their friendship and the many moments we talked about different subjects that eventually allowed me to gain strength to finish and present this work when the task seemed impossible. I would also like to express my infinite gratitude to Diego Mejorado, Phillip Morton, Alejandro Hinojos, Heimdall Mendoza, Shakerur Ridwan and Mohammad Hossain for helping in the completion of several tasks of the project. Very special thanks to Jose Gonzalez whom, although we met for just a few months, proved to be a friend with whom I enjoyed very constructive talks and for bringing his tablet to the office

so we could watch some of the matches of the 2014 FIFA Soccer World Cup. Without the helping hand of all you fellow students, the work would have been much more difficult.

Very sincere thanks to Mr. Pedro Frigola from RadiaBeam Technologies for giving me the opportunity to work in this amazing project. Last but not least, I would like to thank the members of the committee, including Dr. Eric MacDonald, Dr. Russell Chianelli, and Dr. Cristian Botez, for accepting the invitation to supervise my work and providing constructive criticism during my dissertation defense. Special thanks to Dr. Larry Murr who became a mentor and friend at the exact moment I needed it most. My appreciation also goes to Dr. Roberto Osegueda at the Office of Research and Sponsored Projects at UTEP for hiring me as an undergraduate research assistant, making it possible for me to continue my college education.

Last but not least, I thank God for always intervening in my path to make it possible to meet the correct people at the right times. The faith and hope I have for you is greater than ever for you rescued me from despair through the many angels you sent to my side.

– El barco está seguro en el muelle... pero los barcos se hicieron para navegar–

Abstract

Additive Manufacturing (AM) refers to the varied set of technologies utilized for the fabrication of complex 3D components from digital data in a layer-by-layer fashion. The use of these technologies promises to revolutionize the manufacturing industry. The electron beam melting (EBM) process has been utilized for the fabrication of fully dense near-net-shape components from various metallic materials. This process, catalogued as a powder bed fusion technology, consists of the deposition of thin layers (50 – 120 μ m) of metallic powder particles which are fused by the use of a high energy electron beam and has been commercialized by Swedish company Arcam AB.

Superconducting radio frequency (SRF) cavities are key components that are used in linear accelerators and other light sources for studies of elemental physics. Currently, cavity fabrication is done by employing different forming processes including deep-drawing and spinning. In both of the latter techniques, a feedstock high-purity niobium sheet with a thickness ranging from 3-4 mm is mechanically deformed and shaped into the desired geometry. In this manner, half cavities are formed that are later joined by electron beam welding (EBW). The welding step causes variability in the shape of the cavity and can also introduce impurities at the surface of the weld interface. The processing route and the purity of niobium are also of utmost importance since the presence of impurities such as inclusions or defects can be detrimental for the SRF properties of cavities.

The focus of this research was the use of the EBM process in the manufacture of high purity niobium parts with potential SRF applications. Reactor grade niobium was plasma atomized and used as the precursor material for fabrication using EBM. An Arcam A2 system was utilized for the fabrication. The system had all internal components of the fabrication chamber replaced and was cleaned to prevent contamination of niobium powder. A mini-vat, developed at the W.M. Keck Center for 3D Innovation was used for fabrication due to the

limited amount of niobium powder available. Sifting of the material for reuse was done inside a glovebox conditioned to sustain a positive pressure using nitrogen gas and help in delaying moisture adsorption by the powder.

The initial step in the research was the optimization of the fabrication parameters to obtain nearly fully dense (% Relative density > 99%) components followed by the fabrication of application-specific parts to be used for measuring mechanical and physical properties. Such parts, which included a probe or antenna measuring ~85mm tall, were used in the characterization of the thermal conductivity and the residual resistivity ratio of the material; both properties are important in SRF applications. The purity of the material was monitored at different stages from the niobium stock, to the plasma atomized powder, and finally, in the EBM-fabricated parts. For the niobium stock, niobium powder, and in EBM-fabricated parts, chemical analysis was performed using ICP fusion and LECO combustion. A residual gas analyzer (RGA) was used to monitor the vacuum environment during EBM fabrication. X-ray diffraction (XRD) was also used to assess the purity of EBM-fabricated niobium.

A second milestone was the characterization of the tensile properties of EBM-fabricated niobium for the first time. These properties included the average yield and ultimate tensile strengths that measured 140MPa and 255MPa respectively. Measurements of the percent elongation were done using visual feedback from a video camera. Similarly, a boundary detection algorithm was used to approximate the percent reduction in area, because only rectangular specimens were available for experimentation. The measured values averaged 34% elongation and 98% reduction in area.

Microscopy was also employed to characterize the microstructure of the EBM niobium and SEM images of the fractured specimens utilized in a fractography analysis. The microstructure observed in the horizontal plane of reference was of nearly equiaxed grains with a measured size of roughly 250 μ m. In the vertical plane, the microstructure was of columnar

grains that elongated parallel to the EBM build direction. The fractography images revealed the ductile nature of the material with the presence of micro-void coalescence in the fracture surface.

The mechanical properties and microstructure of EBM-fabricated niobium were compared against those of reactor grade niobium. As will be detailed later, the reactor grade niobium had yield and ultimate tensile strengths of 135MPa and 205MPa respectively. The percent elongation was measured at 45.2% and the percent reduction in area at 97.2% for the reactor grade niobium.

Table of Contents

Dedication	iii
Acknowledgements	v
Abstract	vii
Table of Contents	x
List of Tables	xiii
List of Figures	xiv
Statement of the Problem	1
Proposal	2
Justification	2
Chapter 1: Introduction	4
1.1 Physics Background	4
1.2 Project Overview - Additive Manufacturing for Niobium SRF Cavities	5
1.3 Research Facilities Involved	5
1.4 Dissertation Focus	6
1.5 Summary of Obtained Results	7
1.6 Organization of Dissertation	8
Chapter 2: Literature Review	9
2.1 Additive Manufacturing	9
2.2 Electron Beam Melting	10
2.3 Sintering	16
2.4 Particle Charging and Powder Spreading	17
2.5 Superconductivity	19
2.6 SRF Cavities for Accelerators	20
2.7 Traditional SRF Cavity Fabrication Methods	21
2.8 Issues with Current Generation Cavities	25
2.9 Niobium	28

Chapter 3: Experimental Methods	33
3.1 Introduction.....	33
3.2 Upgrading Arcam A2 Interior.....	33
3.3 Cleaning of Chamber Components.....	35
3.4 Steps to Improve the Vacuum During Fabrication	36
3.5 System Calibration.....	37
3.6 Mini-vat.....	41
3.7 Material Handling	44
3.8 Monitoring the Material Purity	46
3.9 Material Characterization.....	48
3.10 Mechanical Properties.....	51
3.11 Physical Properties.....	55
Chapter 4: Fabrication of Niobium in EBM	60
4.1 Previous Work	60
4.2 Processing Conditions in Phase II.....	61
4.3 Fabrication of Niobium Components.....	64
4.4 Complications During Part Fabrication	67
4.5 Causes of Arc-rips and Corrective Measures.....	68
4.6 Part Warping and Powder Overflow	73
Chapter 5: Experimental Results and Discussion	75
5.1 Fabrication of Niobium.....	75
5.2 Material Purity	76
5.3 Material Characterization.....	82
5.4 Mechanical Properties.....	90
5.5 Physical Properties.....	101
Chapter 6: Conclusions and Recommendations	107
6.1 Conclusions.....	107
6.2 Recommendations.....	109

References	111
Appendix A: List of upgraded components for the Arcam A2 system.....	115
Appendix B: Plots of linear region for stress-strain diagrams obtained from tensile testing experiments	117
Appendix C: Grid of parameters explored for densification of EBM niobium and measured values of apparent and relative densities	122
Curriculum Vita	124

List of Tables

Table 2.1 - Properties of reactor grade niobium.	28
Table 2.2 - Specifications of niobium for superconducting cavity production.....	32
Table 4.1 – Properties obtained for EBM Phase I niobium parts	61
Table 5.1 – Chemical Analysis results (in weight %) for niobium powders used.....	77
Table 5.2 – Calculated apparent density for niobium powders	83
Table 5.3 – Calculated values for powder flow rate	83
Table 5.4 – Results from the tension test of EBM and WRG niobium materials.....	94
Table A-1- Components upgraded in Arcam A2 system.....	115
Table C-1 – Fabrication parameters and density measurements for Experiment # 1	122
Table C-2 – Fabrication parameters and density measurements for Experiment # 2	122
Table C-3 – Fabrication parameters and density measurements for Experiment # 3	123
Table C-4 – Density measurements for five sections of EBM square bar using the best fabrication parameters from previous experiments.....	123

List of Figures

Figure 2.1 – Arcam electron beam melting system	11
Figure 2.2 – Stages of sintering. From: (German, 1996)	16
Figure 2.3 – Schematic illustrating particle charging and powder spreading effect.	17
Figure 2.4 – Superconducting transition of mercury as measured in the classical experiment by Onnes.	19
Figure 2.5 – Elliptical SRF cavity assembly. From: (Palmieri, 1997).....	21
Figure 2.6 - Deep-drawing and spinning schematics for niobium sheets into cavity half cells. From: (Padamsee, 2001).	23
Figure 2.7- Hydroforming of niobium tubes. From: (Palmieri, 1997).....	24
Figure 2.8 – Development of the Lorentz pressure in the cavity wall.	25
Figure 2.9 – Trajectories of bent electrons striking the surface of a cavity during field emission. From: (Padamsee, 2001).	26
Figure 2.10 – a) At low fields, the temperature of the near the defect remains below T_c but at higher fields b) T_c is surpassed and power dissipation by niobium causes field breakdown. From: (Padamsee, 2001).	27
Figure 2.11 - Electron beam furnace for niobium purification. From: (Padamsee, 1998)	30
Figure 3.1 - Photograph of the A2 interior listing the major components upgraded during PM..	34
Figure 3.2 - Photograph of the A2's chamber after removal of oxidation and metallization.....	35
Figure 3.3 Rake calibration process.	38
Figure 3.4 - Beam calibration plate showing an amplified view of two calibration holes.	39
Figure 3.5 – Focus and astigmatism calibration of EBM system.	40
Figure 3.6 - Verification plate used in beam calibration of the A2 system.	41
Figure 3.7 - CAD models of the A2's stock vat and the mini-vat cylinder used for fabrication. .	42

Figure 3.8 – CAD rendering of the mini-vat configuration in the Arcam A2 system used for niobium fabrication.....	43
Figure 3.9 – Glovebox unit used for handling and sifting niobium powder in a N ₂ atmosphere. 45	
Figure 3.10 – RGA unit installed on the Arcam A2 system.	47
Figure 3.11 – Hall Flowmeter funnel and density cup.....	49
Figure 3.12 – Tensile test setup utilized showing tensile specimen held by the grips in the MTS machine.	52
Figure 3.13 – Nominal dimensions of fabricated E8/E8M tension specimens.....	52
Figure 3.14 – Original and final areas of square specimens after tension test has been performed. From: (Davis, 2004).....	54
Figure 3.15 – Schematic of fabrication parameter space explored during experimentation to improve the density of EBM niobium.	56
Figure 3.16 – Density measurement kit used for EBM niobium parts.	57
Figure 3.17 – TPS setup used by ThermTest Inc. showing the double metal spiral between the niobium and insulating material discs.....	58
Figure 3.18 – Cavity fabricated at JLab and sample niobium probe used for SRF tests. From: (Ciovati <i>et al.</i> , 2007).....	59
Figure 4.1 – Microstructures of EBM niobium in the vertical a) and horizontal b) directions. Image b) corresponds to the top of the columnar grains.....	60
Figure 4.2 – Powder bed with tracks left by rake due to powder agglomeration. Study carried out during Phase I.	62
Figure 4.3 – Top: temperature profile captured by thermocouple during EBM fabrication of niobium. Bottom: Close-up view.....	63
Figure 4.4 – a) Grid of 9 parts used in density experiments. b) Rectangular bars used for RRR measurements. c) Niobium discs used for thermal and electrical conductivity measurements....	64
Figure 4.5 – EBM fabricated niobium antenna for RF testing.	66

Figure 4.6 – Prototype half cavity design with supporting mesh structures.	66
Figure 4.7 – Fabricated antennas showing the contrast between a part with and without arc-trips or powder smoke during processing.	68
Figure 4.8 – ROIs and relative temperature values captured by the IR camera on the powder bed during niobium fabrication.	69
Figure 4.9 – SEM images for sintered niobium powders. Pictures a) through c) corresponding to currents of 6.5, 15 and 23.5mA, and d) Ti-6Al-4V.	70
Figure 4.10 – a) Copper wire ring attached to the start plate. b) Copper disc inserted in the mini- vat assembly.	71
Figure 4.11 – Isometric and top view of the model used to test the effectiveness of a packed bed approach.	72
Figure 4.12 – Part warping observed in a niobium fabricated part.	73
Figure 4.13 – IR images showing a) overflow and b) no-overflow raking. The arrows in the top image point to the overflowed material when the rake is returning to the left rest position.	74
Figure 5.1 – Tallest niobium part fabricated in EBM. Parts measured ~85 mm in height	75
Figure 5.2 – Chemical analysis history of niobium in Phase I.	76
Figure 5.3 – Weight percent of elements in powder analyzed.	78
Figure 5.4 – a) Typical RGA plot observed during fabrication with niobium. b) Plot showing the increasing behavior in the partial pressure of nitrogen as the time of fabrication extended.	80
Figure 5.5 – XRD spectra for a) powder and b) EBM vertical cross section produced using Phase I powder.	81
Figure 5.6 – XRD spectra for a) powder and b) EBM vertical cross section produced using Phase II powder.	82
Figure 5.7 – SEM images obtained for Phase I powder at a) 100x and b) 300x.	85
Figure 5.8 – SEM images for Phase II powder at a) 100x and b) 300x.	86
Figure 5.9 – Particle size histograms for Phase I a) and Phase II b) powders.	87

Figure 5.10 – Grain microstructure observed for EBM fabricated parts with a) Phase I and b) Phase II powder in the horizontal plane of reference.	88
Figure 5.11 – Columnar grains observed in vertical plane of reference of EBM parts fabricated with a) Phase I and b) Phase II powder.....	89
Figure 5.12 – Microstructure of wrought reactor grade niobium showing equiaxed morphology of grains.	90
Figure 5.13 – Stress-strain curve for EBM niobium specimens.	91
Figure 5.14 – Stress-strain curves for reactor grade niobium.....	91
Figure 5.15 – Measured distance in pixels to evaluate elongation of tensile specimens.....	93
Figure 5.16 – a) Stereomicroscope image fed into the boundary detection code and b) the detected area in pixels.....	94
Figure 5.17 – SEM images at 50x magnification showing fracture surfaces of a) EBM and b) WRG niobium tensile specimens.....	96
Figure 5.18 – 150x SEM pictures showing identified sites of possible porosity in the material pointed by red arrows.....	97
Figure 5.19 – a) SEM image at 60x showing fractured surface of specimen at 45 degrees. b) SEM image at 500x for a WRG specimen showing the micro-void coalescence and dimple formation.....	98
Figure 5.20 – Hardness measurements in the vertical plane for EBM niobium parts.	99
Figure 5.21 – a) Bar produced with Phase I powder showing the delamination that might have caused reduced hardness. b) Shows the bar from Phase II powder with no defects.....	100
Figure 5.22 – Apparent density and %RD values obtained in Experiment # 1.	101
Figure 5.23 - Apparent density and %RD values obtained in Experiment # 2.....	102
Figure 5.24 – Apparent density and %RD values obtained in Experiment # 3.	103
Figure 5.25 – Measured values of apparent density and %RD for five sections extracted from an EBM bar fabricated with optimized parameters.	104

Figure B-1 – Linear region of stress-strain diagram for EBM1 specimen	117
Figure B-2 – Linear region of stress-strain diagram for EBM2 specimen	117
Figure B-3 – Linear region of stress-strain diagram for EBM3 specimen	118
Figure B-4 – Linear region of stress-strain diagram for EBM4 specimen	118
Figure B-5 – Linear region of stress-strain diagram for WRG1 specimen.....	119
Figure B-6 – Linear region of stress-strain diagram for WRG2 specimen.....	119
Figure B-7 – Linear region of stress-strain diagram for WRG3 specimen.....	120
Figure B-8 – Linear region of stress-strain diagram for WRG4 specimen.....	120
Figure B-9 – Linear region of stress-strain diagram for WRG5 specimen.....	121

Statement of the Problem

Superconducting radio frequency (SRF) cavities are used in various particle accelerator and other light sources for studies of elemental physics. Currently, cavity fabrication is done by employing different forming processes including deep-drawing and spinning. In both of the latter techniques, a feedstock high-purity niobium sheet with a thickness ranging from 3-4 mm is mechanically deformed and shaped into the desired geometry. In this manner, half cavities are formed that are later joined by electron beam welding. The shape of a half cavity resembles a bowl with a hole at the thinnest section or iris and it expands to a maximum diameter near the equator.

During operation a cavity experiences mechanical forces that develop from its interaction with the electric and magnetic fields. The correct function of one cavity can become compromised if these forces cause excessive deformation that can lead to detuning or shifting of the resonant frequency. Because of the detuning effect, mechanical tuners are required to synchronize the frequency in multiple cavity assemblies. Of particular interest is the development of the non-uniform Lorentz force that manifests as an inward pressure near the iris and as outward pressure at the equator of the cavity. Stiffener rings and other supports are welded to the cavity to provide stability against Lorentz force detuning. Other end group components made from niobium and that are used in accelerators experience large thermal gradients that result in high stress concentration. Therefore, their use also requires added support structures that are electron beam welded as well. Although widespread, the use of additional supporting structures comes at the expense of introducing variability and complexity to the intended component geometry.

Proposal

The research effort presented in this dissertation proposes the use of the novel additive manufacturing (AM) technology of electron beam melting (EBM) for the fabrication of monolithic structures using ultra-high purity niobium for SRF applications. As a main objective, this research entails the improvement of the fabrication conditions to maintain the purity of the material from the precursor niobium powder to the EBM fabricated parts and the optimization of the fabrication parameters to obtain nearly fully dense components. Several methodologies will be used to monitor the purity of the material at various stages of the fabrication process. The work will also focus on the characterization of the EBM produced niobium parts. Microstructural observations and measurement of mechanical properties such as tensile strength and hardness will be performed and compared against those obtained from wrought niobium stock to provide a comparison point. More importantly, the electrical and magnetic properties (particularly the residual resistivity ratio, RRR) of the EBM niobium will be measured to evaluate the feasibility of using this AM technology in the fabrication of components for superconductivity applications. To this end, application specific parts will be constructed, including an RF probe or antenna and a prototype SRF cavity both of which will be tested in current superconductivity experiment setups.

Justification

The EBM process can be employed for the fabrication of complex metallic structures in a layer-by-layer fashion directly from digital information. This manufacturing method can enable the production of components for superconductivity experiments with a reduced number of welds thus improving their mechanical stability. The EBM method offers the possibility for creating RF cavities with varying wall thickness and that integrate embedded support structures or thermal management configurations providing mechanical stability and reducing the

variability from part to part. Furthermore, the EBM process has the potential of providing the means for fabricating fully dense niobium parts with material properties that are comparable to those exhibited by the wrought material. The latter benefits are possible at a level not permitted by current manufacturing processes employed in the production of components for superconductivity experiments.

Chapter 1: Introduction

1.1 Physics Background

The subject of particle physics is advancing the understanding of our universe by studying the nature and interactions amongst the fundamental particles forming the continuum of matter, energy, space and time. Although it is considered an in-complete theory for it makes some simplifying assumptions, the standard model of physics has been widely adopted and intensively researched (Mann, 2010). For decades since the establishment of this model, groups of scientists and engineers have worked on developing the theory and tools for experimentally testing this formulation with many discoveries of elementary particles suggesting the soundness of the model. These scientific efforts have sprouted around the world in the form of state-of-the-art linear particle accelerators and other light sources at facilities such as CERN, DESY, KEK, ANL, and FNAL to name a few. These facilities house large arrays of devices including superconducting cavities that transfer the energy to and guide the traveling particles. The study of the behavior and nature of these elemental particles right after their collision is the subject of ongoing research.

A superconducting radio-frequency (SRF) cavity is a key component in the configuration of any linear accelerator. This is the device used to transfer energy to accelerate the particles. Great demand is placed for the use of cavities since multiple units are normally employed in a single accelerator assembly. Traditionally, high purity niobium sheets of $\sim 3\text{mm}$ in thickness are shaped into SRF cavities. The sheets are formed into half-cells employing techniques such as deep-drawing and spinning followed by electron beam welding to complete the cavity. Pure niobium, even though it has a low critical temperature (9.2 K), is still preferred over other materials such as niobium-titanium or niobium-tin alloys as it shows more promise for operating at higher accelerating gradients. It has therefore become the material of choice for the fabrication of SRF cavities for use in linear accelerators, neutron sources or light sources such as synchrotrons (Aune *et al.*, 2000).

1.2 Project Overview - Additive Manufacturing for Niobium SRF Cavities

The advances in manufacturing in the commonly called 3D printing technologies have opened the door for multiple innovation possibilities in various areas previously considered restricted. These technologies, catalogued now within the term additive manufacturing (AM), consist on the fabrication of components by the gradual deposition of material in a layer-by-layer fashion. Specifically involved with the fabrication of metallic components, techniques that use the energy from a laser or an electron beam, catalogued as powder bed fusion technologies, are employed to sinter and fully melt specific regions in thin layers of powder to construct monolith parts from computer aided design (CAD) models (Gibson *et al.*, 2010).

In this dissertation, Arcam's EBM process was used to investigate the fabrication of pure niobium SRF cavities and other end group components with applications in the area of particle physics for the first time. The project resulted from a collaborative research effort between the W. M. Keck Center for 3D Innovation (Keck Center) at UTEP and RadiaBeam Technologies, LLC (RadiaBeam) as part of a SBIR grant with the U.S. Department of Energy. There is a growing interest for the use of SRF cavities in particle accelerator experiments although improvements to the technology and to the traditional cavity fabrication processes are required. In the work detailed in this dissertation the use of EBM AM for fabrication of niobium components has been explored. The mechanical and physical properties of the fabricated parts have been characterized and contrasted against those obtained from conventional niobium manufacturing processes to evaluate their potential for use in superconductivity experiments.

1.3 Research Facilities Involved

The activities of the project were performed at the Keck Center. This center was established in 2000 with a grant from the W. M. Keck Foundation and has since become a hub of innovation in the area of additive manufacturing (AM) technologies. Within the Keck Center's recent expansion to over 13,000 ft², access is provided to well over 50 research equipment ranging from AM systems for plastic, resins, metals and ceramics, traditional manufacturing

machines including a computer numerical control (CNC) milling machine and a lathe, and systems for mechanical testing, reverse engineering and metrology of components. In collaboration with other departments in the college of engineering at UTEP, facilities for material characterization by optical microscopy, scanning electron microscopy (SEM), and transmission electron microscopy (TEM), as well as a machine shop for manufacturing were also available for this project.

RadiaBeam was formed in 2003 by a group of scientists and engineers from the UCLA Particle Beam Physics Laboratory. With a ~4000 ft² facility set in Santa Monica, CA, the company performs R&D focused in meeting the demand and advancing the development of components for use in particle accelerators systems. RadiaBeam's facilities include shops for manufacturing, RF testing and a class 100 clean room with ultra-high vacuum (UHV) capabilities. The company has multiple partnerships with both industry and academia providing it with access to research facilities such as the Thomas Jefferson National Accelerator Facility (Jefferson Lab) at which characterization of the electronic properties of EBM fabricated niobium including DC and RF measurements was performed (RadiaBeam Technologies LLC).

1.4 Dissertation Focus

The work presented in this dissertation investigates the fabrication of niobium prototype parts with improved mechanical and electrical properties using the EBM process. The project explores the manufacture of improved designs for SRF accelerating cavities and other end group components used in particle accelerator devices employing this AM technology. Aside from improvements in mechanical and electrical properties, the optimized parts exhibit novel features including integrated stiffeners and variations in wall thickness thus improving their mechanical stability during operation.

1.5 Summary of Obtained Results

In this project, the fabrication of high purity niobium by the EBM technique was achieved. This is the first time that tall structures have been produced including one near net shape part (niobium probe) that was used for measurement of SRF properties.

The quality of the EBM chamber environment during fabrication was monitored with the use of a residual gas analyzer (RGA) that demonstrated the suitability of this additive manufacturing process to restrict the impurity content of both the precursor powder and the fabricated parts. The x-ray diffraction technique corroborated a clean spectrum for EBM fabricated niobium ruling out the presence of impurities in the final material. Equally important was the implementation of a protocol for handling the powder material inside a glovebox with a N₂ atmosphere and the installation of a ventilation system for the Arcam A2 also using N₂ gas. Both measures prevented the adsorption of moisture or other interstitial elements into the precursor powder making it more suitable for fabrication of EBM parts with SRF applications.

Another fulfilled milestone was the fabrication of specimens that permitted the characterization of thermal and superconducting properties for EBM-fabricated niobium. Several EBM parts were produced (refer to Chapter 4, Figure 4.4) and provided to RadiaBeam for testing of properties such as thermal conductivity and residual resistivity ratio (RRR) of the material.

Last but not least, one of the main goals of the project during this phase (Phase II) was the improvement of the density in EBM-fabricated niobium parts. This goal was achieved, as described in the Chapter 5, as parts with apparent densities of 8.55g/cm³ were fabricated which represented a percent relative density (% RD) greater than 99.5%. Previous % RD values in Phase I maxed at 98.65%.

1.6 Organization of Dissertation

This dissertation is organized in six chapters. Chapter one has presented the main characteristics of the project describing, in an overall manner, the motivation of the project, the sources of funding utilized, the facilities involved in the experimentation, as well as providing a brief introduction to the subject of SRF cavities and their importance for next generation physics experimentation. Chapter two provides the literature review for the many subjects described in the project. The first section in chapter two provides an account on the subject of additive manufacturing (AM) technologies focusing in the powder bed fusion method of electron beam melting (EBM) which corresponds to the process used in the work described in this dissertation. The second section provides details for the extraction and purification of niobium from the ore and the gas atomization technique required to process it into powder form suitable for use in the EBM technology. Finally, the third section in this chapter provides an overview of superconductivity by the use of RF devices and also describes conventional production methods for niobium components, particularly for SRF cavities, including issues and challenges associated with their use. Chapter three details the preparation of the EBM system for fabrication with niobium and also provides reference to the experimental methods used to characterize the mechanical and physical properties of fabricated parts. Chapter four provides specifics on the fabrication of niobium using the EBM which includes the temperature cycles required and issues encountered during the fabrication experiments. Chapter five then deals with the presentation and discussion of the results obtained with the applied experimental methods. Finally, chapter six states the conclusions that are drawn from this research and provides references for future work that has been identified for continuation of this investigation.

Chapter 2: Literature Review

2.1 Additive Manufacturing

The subject of additive manufacturing (AM) has gained relevance in recent years. Commonly known as three-dimensional (3D) printing, the term AM evolved from its beginnings as rapid prototyping to reflect the nature of processes used in the fabrication of objects from digital data produced using computer aided design (CAD) software. Multiple processes have been developed that work with a comparable number of materials however they rely on the same basic premise of fabrication of a part by the gradual deposition of material in a layer-by-layer fashion (Gibson *et al.*, 2010).

AM technologies provide many advantages over traditional manufacturing as they can be used for direct manufacture of complex geometries without incurring expenses derived from fabrication of additional fixtures, required tooling equipment or a process planning. Although the fabrication procedure varies according to the used AM technique, the general steps have been outlined before describing the route from the concept to the finished part. The different stages as summarized by Gibson *et al.* include:

- Modeling of the concept part using specialized CAD software.
- Conversion of the 3D model into STL file that describes its general topology.
- Processing of the STL into a slice file specific to the AM process being used.
- Setup of the AM system and actual fabrication of the part.
- Removal of the finished part from the AM system.
- Post-processing steps that can include removal of support material and post-fabrication treatments such as heat-treatment or polishing.

Some of the most recognizable processes include material extrusion and deposition through nozzles, photopolymerization or curing of liquid resin materials using a laser or other source of light, and printing processes for polymers and ceramics based on the deposition of drops of binder. In the case of AM for processing of metal materials, techniques that include the

lamination of thin metal sheets using ultrasonic waves, and the use of powder bed fusion methods that use the energy from a laser or electron beam to sinter and melt individual metal powder particles in specific regions or patterns, have been the subject of intense research.

2.2 Electron Beam Melting

The process of electron beam melting has been commercially available from the Swedish company Arcam since 2000 (Arcam AB, Sweden). The technology, catalogued under the powder bed fusion designation (ASTM Standard F2792-12a), uses a stream of traveling electrons as the energy source to melt metal particles in powder form. In the process, layers of metal powder with a thickness in the range from 50-120 μm are evenly spread by a raking mechanism. Then the electron beam is used to preheat the powder bed followed by the selective melting in specific regions through the bed using higher energy on the beam. The electron beam is accurately and rapidly steered to scan specific geometries with the use of electromagnetic lenses or coils positioned in the gun column. After processing of one layer, the build table is lowered in the z direction by a thickness of one layer and the process repeats. Complex designs can be obtained by following the process until completion of the model. Both the preheating and the melting sequences are carried out by the electron beam. The stream of electrons is energized at 60kV and steered by magnetic lenses. The process is performed in vacuum ($\sim 10^{-4}$ Torr) to ensure reduced particle collisions and the transfer of the kinetic energy in the electrons to the powder bed. The vacuum also prevents oxidation of the powder during fabrication. The main components (Figure 2.1) in the commercial Arcam systems are the electron gun (1), electromagnetic coils (2), powder hoppers or containers from which powder is gravity fed (3), the raking arm (4) and the build stage (6). Normally, the process uses a build substrate to commence fabrication and provide anchoring of the initial layers of the part being produced (5).

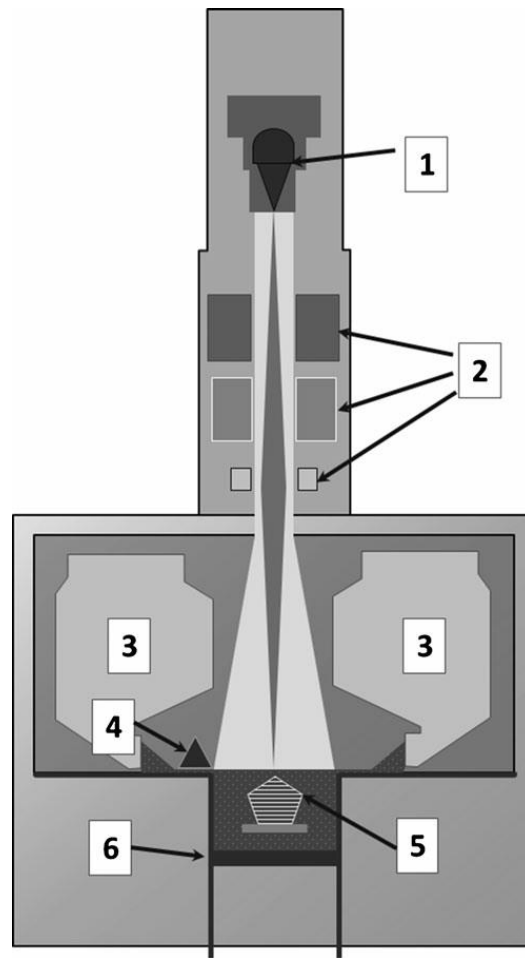


Figure 2.1 – Arcam electron beam melting system

When fabrication is complete, the system is allowed cooling down and it is normally assisted with a helium gas purge to speed up this process. Once the thermocouple indicates a temperature lower than 100°C, the manufactured parts are removed from the envelope of the machine along with partially sintered powder material surrounding the. The sintered powder is removed with the use of a powder recovery system (PRS). The PRS uses a stream of air and metal powder particles of the same material to blast on the surface effectively removing any non-solid material. It is calculated that roughly 90% of the powder removed during this step can be recovered, sifted and reused without much loss of alloying chemistry (Wohlers, 2009).

2.2.1 Materials Processed by EBM

Several metallic materials have been processed using the EBM technology. The most representative is Ti6Al4V alloy which has been studied with particular interest as an implantable material given its biocompatibility (Murr *et al.*, 2009). The set of mechanical properties including light weight and high corrosion resistance have also made this alloy of interest as a structural material for aerospace applications. Manufacturing of aerospace components with these alloys has been previously done by castings and machining but as the costs of such processes become restrictive for high performance materials such as Ti-6Al-4V EBM has been explored as a possible fabrication method in this sector (Wooten and Dennies, 2008).

Superalloy materials, traditionally employed to fabricate components exposed to high temperature conditions, have also been processed by EBM. Structures made out of the directional solidified nickel-based superalloy René 142 were characterized as having an optimized volume fraction of the strengthening γ' -precipitate phase which would benefit the creep resistance of components such as turbine blades (Murr *et al.*, 2013a). Microstructural characterization of Inconel 718 produced by EBM revealed the precipitation of very fine γ'' precipitates while the γ grains were observed to grow preferentially in the build direction ($\langle 100 \rangle$ direction) for several millimeters (Strondl *et al.*, 2008). Columnar arrays of Cr_{23}C_6 carbides and dislocations were observed by TEM in Co-26Cr-6Mo-0.2C specimens fabricated using EBM (Gaytan *et al.*, 2011).

Other materials have been researched for fabrication using EBM. For instance, copper (Cu) components consisting of solid parts as well as open cellular structures were fabricated and characterized (Ramirez *et al.*, 2011). Although the fabrication parameters required improvement, Cu structures could be fabricated and they exhibited elongated and columnar grain morphologies. A series of experiments were performed for the EBM fabrication of aluminum parts from alloys 2024 and 7075. Several parts were fabricated with a reasonable geometric control from both alloys. The parts manufactured included simple mechanical shapes or complex

ones such as mesh structures to be used as heat exchangers with large surface areas. However, some porosity, originating from incomplete melting of powder particles, was still encountered in the fabricated parts. Even more challenging was the evaporation of the alloying elements which consistently resulted in parts that were below standard chemistry specifications (Mahale *et al.*, 2007).

In recent research performed at the W.M. Keck Center, the pre-alloyed two phase gamma titanium aluminide (Ti-48Al-2Cr-2Nb) was fabricated by EBM into fully dense parts such as solid blocks and foams and their grain structure characterized by microscopy and TEM (Hernandez *et al.*, 2012). Similarly, pure niobium components were fabricated in a small scale vat using an Arcam S12 EBM system that exhibited the columnar grain morphology parallel to the build direction. In this study, the parts fabricated had limited heights (~5 to 8mm in thickness) but demonstrated the capacity of EBM to fabricate this high melting point material (Martinez *et al.*, 2013). Finally, solid parts and reticulated mesh structures were fabricated from pure iron powder using the EBM process. Characterization of this parts showed that EBM processing caused retention and increase of the metastable δ -Fe phase within the α -Fe matrix (Murr *et al.*, 2013b).

2.2.2 Advantages of EBM Process

The EBM system is considered vital for some industries provided it can be used for the serial production of components using the titanium and cobalt-chrome alloys commercialized by Arcam. Since its introduction it became a competitive alternative to laser-based technologies for it provided faster production rates (Wohlers, 2009). Since the electron beam is deflected without the need of any moving parts, this allows for faster scanning speeds of up to 40,000 mm/s and this translates into high build speeds (Larsson *et al.*, 2003; Mahale, 2009). Contrasting with laser systems, the EBM process achieves several times higher energy efficiency with lower power consumption (Larsson *et al.*, 2003).

During fabrication, the electron beam is regularly used to preheat the powder bed to maintain it at an optimal temperature depending on the material being used. This characteristic makes the resulting parts generally free from residual stresses that normally develop in other AM methods.

The use of vacuum in EBM provides a good thermal environment for fabrication and eliminates negative effects from impurities (Larsson *et al.*, 2003). The operation under vacuum also provides the ability to process high melting point materials such as nickel and cobalt superalloys, and highly reactive materials such as titanium alloys.

The rapid melting and solidification taking place during the processing in EBM has been associated with the optimization of microstructures and resulting improvement in mechanical properties. As pointed out before, observations of the parts fabricated from the superalloy René 142 exhibited an optimized volume fraction of the strengthening phase making it suitable for creep resistance applications (Murr *et al.*, 2013a). EBM fabrication of pure iron resulted in an increase in content of the metastable δ -Fe phase, which was thought to originate from the rapid melting and solidification conditions. The increased content of δ -Fe contributed to discontinuous yielding of the material but further research was recommended to fully characterize the effect on the mechanical properties of the iron (Murr *et al.*, 2013b). Finally, a refinement of the microstructure of open cellular foams fabricated by EBM using the Ti-6Al-4V alloy promoted increased micro-indentation (HV) hardness, and thus implied higher yield strength of the material according to the relation $\sigma_y = HV/3$ (Murr *et al.*, 2010).

2.2.3 Recommended Powder Properties for EBM

Although many different metal powders have been processed with the EBM process with success, Arcam provides several guidelines for researching fabrication with new materials. Some of the recommendations include:

- Spherical particles to minimize surface area and lower risk of fire/explosions (Arcam, 2010). Compared to flake like powders which have higher surface area, the reduced area of spherical powders limits the energy required for ignition (Eapen, 2004).
- A high ability of the material to flow without assistance similar to Arcam's provided Ti-6Al-4V powder of 25sec/50g (Arcam, 2010).
- High apparent density that is greater than 50% of the density of the solid or wrought material (Medina, 2013; Arcam, 2010).
- Due to health and safety concerns, individual powder particles must be larger than 10 μ m to prevent aspiration. Spherical solids with diameters below 10 μ m pose a health risk since they can be inhaled and deposited in the lungs and alveoli leading to chronic respiratory problems (Luther, 2004).

2.2.4 EBM Parameter Development

The development of processing parameters for a material normally involves the determination of several variables working in synchrony. As a starting point, experiments are performed to determine the sintering temperature of the material. In the EBM process, a powder bed is laid and the start plate placed atop. The purpose of the sintering test is the determination of the temperature at which powder underneath the start plate starts to coalesce and bind to it. This is an important factor contributing to success of the build since the proper sintering under the start plate provides stability of the fabrication substrate throughout fabrication.

The next step in the development of processing parameters is the determination of the preheat and melt themes. Proper preheating parameters allow for maintaining the temperature of the powder bed high enough to cause binding of individual particles prior to the melt scan. A combination of scan speed, number of scan repetitions, and the current and focus offset of the electron beam promote the above condition while preventing particle charging and subsequent powder spreading. Regarding the melt parameters, the proper combination of beam current,

scanning speed and focus offset must also be found to achieve complete melting or fusion of the current layer while preventing surface instability effects such as balling or delamination.

2.3 Sintering

Sintering can be described as the coalescence of material particles by diffusion of atoms in between discrete material particles. Various atom transfer mechanisms or diffusion paths have been identified that contribute to sintering depending on the route atoms have to travel (Murr, 1975). Regardless of the mechanism, atomic movement obeys the minimization of the surface free energy in the material. Energy is minimized when internal surface area such as porosity is eliminated by sintering (Sōmiya, 2013). The application of temperature and pressure enhance sintering speed by providing more energy and thus faster diffusion rates for atoms. For most materials, temperatures in the range of 0.5 to 0.8 of the melting point serve to promote sintering (German, 1996). A two sphere model allows describing the phases of sintering. In the model, particles come to an initial point contact position. Then, in the early sintering stage there is the development of a neck in between particles. Late stage sintering is exhibited over long time as the inter-particle neck grows. Finally, after very long times, particles are fully coalesced (Figure 2.2). In the EBM process, the coalescence of the powder particles in the processing layer is achieved during the preheating step. The partial binding of the particles prepares the surface prior to the melt sequence. The sintering of particles during this process also has the beneficial effect of preventing the scattering of the powder, an effect that is detrimental to EBM fabrication, as explained in the next section.

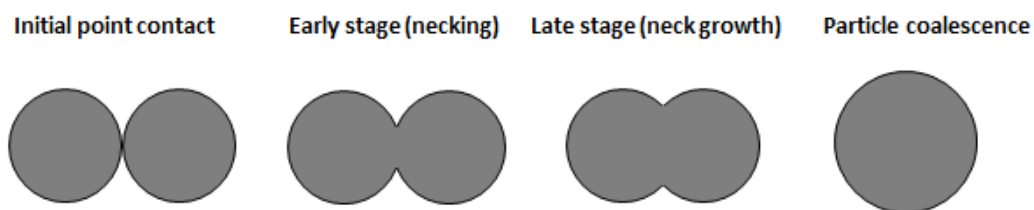


Figure 2.2 – Stages of sintering. From: (German, 1996)

2.4 Particle Charging and Powder Spreading

During fabrication of a component, the EBM process normally employs a preheat cycle followed by scanning of the part at higher energies during the melt step. Preheating achieves sintering of the current powder layer prior to melting and also helps to maintain the powder bed at high temperatures throughout the process. The partial sintering of powder during the preheating step provides the extra benefit of helping prevent the incidence of particle charging and the consequential powder spreading effect. This phenomenon is referred by Arcam to as “smoke” and it is characterized by the violent scattering of individual powder particles. The occurrence of smoke is detrimental to the fabrication process in EBM since the powder particles are ejected from the powder bed resulting in an uneven distribution of the current layer. When this occurs, part porosity has been observed in the affected layer using IR cameras to monitor the EBM process (Rodriguez *et al.*, 2013; Dinwiddie *et al.*, 2013). In addition, the fabrication process can become compromised and fail if several simultaneous smoke events happen for a given millimeter fabricated. Spreading of the powder starts by the accumulation of charge in the powder particles. As the repulsive forces exceed the binding due to sintering, powder particles are expelled in random trajectories (Figure 2.3).

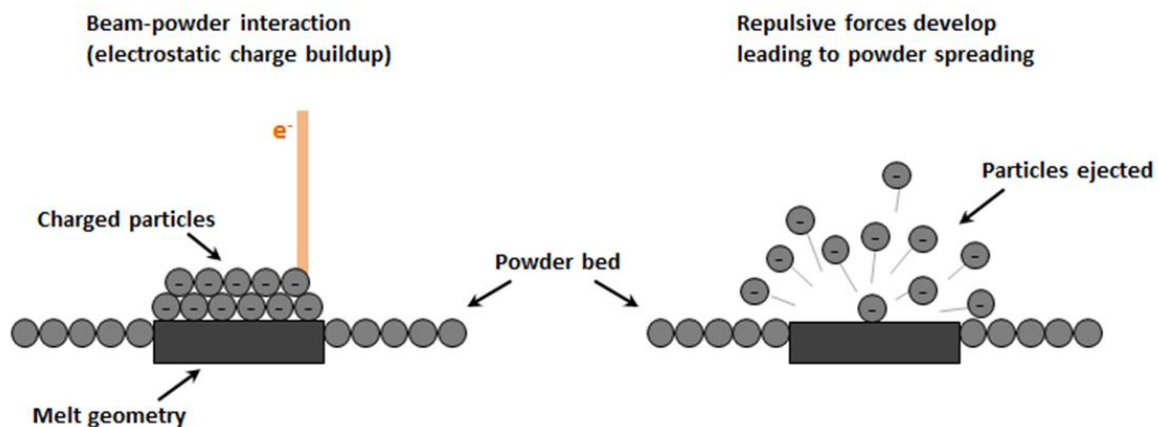


Figure 2.3 – Schematic illustrating particle charging and powder spreading effect.

In the EBM method, the electron beam carries an electrical charge in contrast to other AM technologies that employ lasers as the heat source. Therefore, measurable electrostatic forces develop from the interaction between the beam and material particles in the powder bed leading to smoke events. Particle charging and powder smoke were documented in an experimental electron beam welding machine using high-speed photography. In this study, three possible causes of the powder spreading effect were evaluated which included humidity residues in the precursor powder, impulsive forces on the particles as momentum was transferred from the moving electrons, and electrostatic charge buildup on the powder particles. This study rejected the hypothesis that humidity in powder caused smoking by monitoring chamber pressures that showed no drastic changes. The variations on pressure would have resulted from too much outgassing of water vapor during heating of the powder. Similarly, the momentum transfer theory was disproved as calculations of the momentum transfer from a stream of electrons revealed the interaction of the electron beam and powder particles required over 15 minutes to cause enough moment to displace individual particles. The study then analyzed the forces that arise due to electrostatic charging and concluded they were of sufficient magnitude to overcome binding and gravity forces of particles causing them to spread as in an explosion (Milberg and Sigl, 2008).

The mechanism by which electrostatic charge builds up has been previously studied. As the electron beam scans the powder either during the preheating or melting steps, small negative charges accumulate giving rise to Coulomb forces that eventually lead to spreading of the powder layer (Zah *et al.*, 2008). A recent analysis of the powder spreading effect categorized the problem in two types of smoke occurring in EBM. Type I smoke resulted when the electron beam was raster scanning over a hatch pattern such as what occurs during the preheating step. As the beam rasters over one pattern, the powder particles in that track experienced repulsive forces from the negative charge accumulated in a previously scanned adjacent area. Type II smoke was observed as the beam was vector scanning a cross sectional area such as when

melting of contours or the hatch geometry. The relative lower beam speeds during vector scan also caused buildup of negative charges and triggered smoke in contiguous powder. In both cases, spreading would occur if the repulsive forces exceeded the binding forces in the powder particles coming from inter-particle sintering and the weight of individual powder particles (Mahale, 2009).

2.5 Superconductivity

The word superconductivity was first coined by H. K. Onnes in 1913 to describe the peculiar effect that occurs when the electrical resistance of a conductor drops to zero at cryogenic temperatures. As illustrated in Figure 2.4, in the experiment carried out by Onnes, he observed that the resistance of high purity mercury vanished in an abrupt manner when the element was cooled to 4.19°K (APS News, 2007). An explanation for the superconducting state was not developed for several decades until 1957 when the Bardeen-Cooper-Schrieffer (BCS) theory was presented (Bardeen *et al.*, 1957).

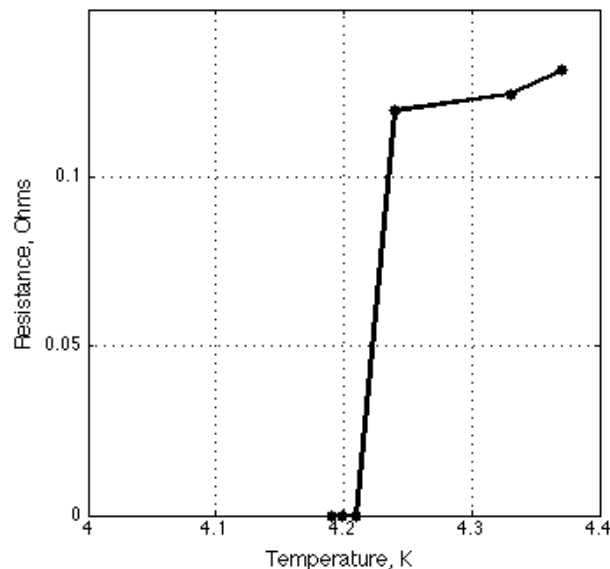


Figure 2.4 – Superconducting transition of mercury as measured in the classical experiment by Onnes.

Since then, many materials have been discovered that become superconducting when cooled below their transition temperature. In the mid 1980's metallic compounds such as those belonging to the Ba-La-Cu-O system were shown to exhibit superconductivity at a relatively high temperature of $\sim 30^\circ\text{K}$ (Bednorz and Müller, 1986). To date, the highest transition temperature in a material belongs to $\text{Hg}_{0.8}\text{Tl}_{0.2}\text{Ba}_2\text{Ca}_2\text{Cu}_3\text{O}_{8.33}$ at 138°K (USPAS, 2013). Niobium, as will be described later, exhibits the highest transition temperature of all pure elements at 9.2°K .

2.5.1 RF Superconductivity

Radio frequency (RF) superconductivity refers to the use of superconductors in radio frequency devices. Superconducting materials are used in the fabrication of radio frequency resonators (cavities) because their negligible electrical resistance provides the resonator with a high quality factor (Q). The Q factor measures the ability of the SRF resonator or cavity to store energy. It is defined as an efficiency ratio indicating the energy gain to power dissipated in an RF cycle (Zeng and Harms, 2012). Typical values of quality factor for niobium SRF cavities are on the order of 10^9 to 10^{10} (Padamsee, 1998).

2.6 SRF Cavities for Accelerators

Superconducting radio frequency (SRF) cavities are employed in linear accelerators and other light sources to carry out elemental physics studies. The cavity is the device that imparts velocity to the traveling particles. As the cavity is cooled below the transition temperature of niobium, it becomes superconducting and produces strong electromagnetic fields as it resonates in a microwave frequency when operated in a continuous wave (CW) mode. Different designs have been explored along the years since 1965 when the early efforts at Stanford University resulted in the first lead-plated resonators for use at the High-Energy Physics Lab (HEPL) (Padamsee, 1998). Different geometries have been explored since then, always responding to the

demands of the particular application. Widely adopted nowadays is the elliptical cavity design which evolved from the pillbox configuration and provided means for experimenting at higher accelerating fields and ease of formability during manufacturing. These current generation cavity assemblies have the shape as the structure shown in Figure 2.5. The full cavity profile has a small opening or iris at both ends and it expands to a maximum diameter at the equator. The length of the cavity is selected such that the radiofrequency (RF) cycle is synchronized with the motion of electrons to provide the kick in energy (Ding *et al.*, 2010).



Figure 2.5 – Elliptical SRF cavity assembly. From: (Palmieri, 1997)

2.7 Traditional SRF Cavity Fabrication Methods

2.7.1 Machining

Traditionally, machining is not employed for the mass production of cavities or any other niobium components for superconductivity applications. Some examples are provided in literature of the use of subtractive machining in the fabrication of cavities. However, the reason why machining use is not widespread is that it becomes cost restrictive and thus it is not viable from an economic perspective. Also, machining of niobium requires much operator experience in setting up the material and in selection of cutting tools. It also requires specific rates of

cutting and cooling with fluid to prevent the material from heating up and breaking the cutting tool. Guidelines have been provided as a starting reference point for whenever machining of niobium is performed. These include the use of preferably high speed steel cutting tool with an approach angle of 15-20 degrees, a cutting speed of 20-25 m/min, and the use of one of various coolants that include water, oils and other chemicals as trichlorethylene and tetrachlorocarbon (Bauer, 1980).

2.7.2 Forming Processes

Other processes employed in producing SRF niobium cavities rely on the use of dies and tonnage from hydraulic presses to carry the forming process of the stock material into the cavity shape. The three most notable processes include deep-drawing, spinning and hydroforming. Half-cells produced by deep-drawing normally undergo coining of the iris as a post-processing step while spun cavities have to be trimmed to remove excess material. Both techniques normally result in half-cells which require electron beam welding (EBW) at the equator to form the complete SRF cavity (Padamsee, 2001). Hydroforming is able to produce single cell and multi cell seamless cavities. Accuracies achieved by these methods are on the order of 0.2 to 0.3mm but nevertheless, the final accuracy depends on the material deposited during the EBW step (Bauer, 1980).

2.7.2.1 Deep Drawing

In the deep-drawing technique, niobium sheets (thickness ~3 mm) are formed into the desired shape by pressing them in between a set of dies. The process starts by bolting a disc of niobium cut from the feedstock blanket in between the female die and a holder plate. A hydraulic press is then used that lowers the male die or punch applying pressure and causing deformation of the material into the shape of the die (Padamsee, 2001). With this process, half cells cavities have been produced at many physics laboratories including Cornell, Genua and CERN. Nevertheless, there are several issues associated with the forming of cavities by deep

drawing which are related to variations in the tolerances attained in the thickness of the resulting part, problems while removing the parts from the dies, alterations in the elastic properties of the material and other effects related to the microstructure of the niobium sheet used (Bauer, 1980). Furthermore, intrinsic to the fabrication process, the thickness of the fabricated cavity is limited to the starting thickness of the niobium sheet and with accuracies, as mentioned before, of 0.2 to 0.3mm.

2.7.2.2 Spinning

In spinning, cavities are shaped by bolting a circular blank of niobium from the center and then using an adjustable mandrel to apply pressure and form the shape of the cavity. This technology was initially developed with the intent to fabricate seamless cavity cell assemblies or resonators. With the proper size of blank used as the stock material, studies have demonstrated the viability to spun multi-cell cavities with very tight tolerances and repeatability (Kneisel and Palmieri, 1999). Figure 2.6 illustrates the cavity fabrication processes of deep-drawing and spinning.

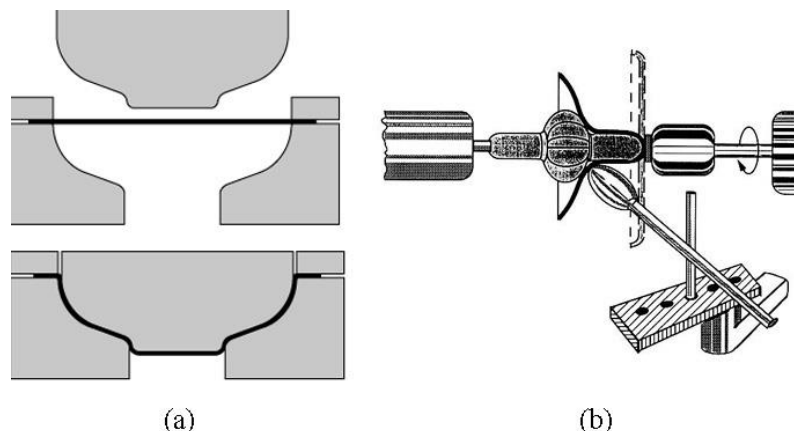


Figure 2.6 - Deep-drawing and spinning schematics for niobium sheets into cavity half cells. From: (Padamsee, 2001).

2.7.2.3 Hydroforming

In the hydroforming technique, a niobium tube is shaped by expanding its diameter at the equator while causing a reduction at the location of the iris. This process is achieved by simultaneous application of hydraulic pressure at the inside of the tube while the opposite end is axially displaced (Figure 2.7). Using computer numerical control, the loading parameters can be effectively reproduced to fabricate cavity cells which do not require welding. The technique has been employed in the fabrication of single-cell and multi-cell bimetallic niobium-copper cavities and also bulk niobium ones. The RF performance of such cavities was comparable to those measured in standard bulk niobium cavities with accelerating fields reaching up to 43 MV/m (Singer, 2006). Despite the fact that early attempts at hydroforming of niobium were challenging due to the lack of uniformity of niobium tubes (Kneisel and Palmieri, 1999), the technology has been identified as an alternative to reduce the fabrication costs of niobium SRF cavities (Compton *et al.*, 2007).

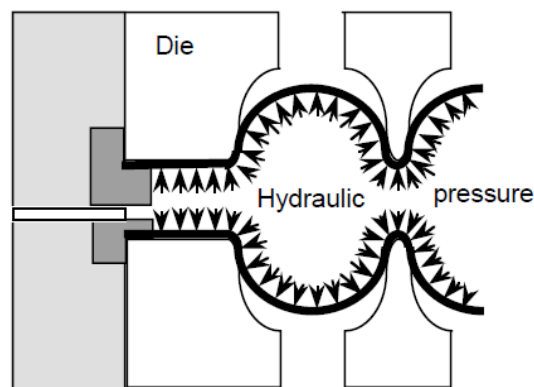


Figure 2.7- Hydroforming of niobium tubes. From: (Palmieri, 1997)

2.8 Issues with Current Generation Cavities

2.8.1 Lorentz Force Detuning

One common problem with SRF cavities is the frequency detuning effect that occurs when they are being excited by the RF source. Detuning is important as the RF power required for operation depends on the frequency at small effective beam currents (Posen and Liepe, 2012). At very high detuning, coupling is lost between the resonator and the power source which causes the decay and pondermotive oscillation of the accelerating field. This effect is known as Lorentz force detuning and it starts by the interaction of the magnetic field and the RF wall current that develop in the cavity. The physical effect is seen as radiation pressure that has been shown to push in a non-uniform manner in the cavity wall; inwards at the iris and outwards at the equator (Figure 2.8). Thus far, the only remedy to minimize the Lorentz force detuning is by increasing the stiffness of the cavity (Padamsee, 1998). This is achieved by the introduction of other structures such as stiffening rings or by implementing fast piezoelectric actuator tuners. Nevertheless, the added structures can contribute to complexity, increased risk of contamination, and their effectiveness can be reduced by the mechanical resonance on the cavity assembly (Posen and Liepe, 2012; Ries *et al.*, 2003; Longuevergne *et al.*, 2014).

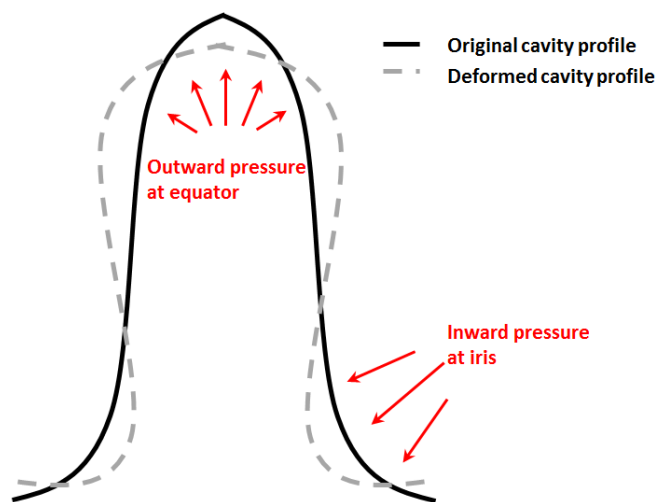


Figure 2.8 – Development of the Lorentz pressure in the cavity wall.

2.8.2 Field Emission

Field emission refers to the process in which electrons overcome the energy to tunnel through the quantum mechanical barrier in a metal surface. Field emission reduces the performance of SRF cavities as it consumes the RF power available causing the decay of the field and of the Q factor (Moffat *et al.*, 1991). In a multiple cavity assembly some of the field emitted electrons in a cavity can be bent by the magnetic field and can strike the surface of another cavity producing sites of localized heat and field instability (Figure 2.9).

Thermal and x-ray mapping techniques are used in pinpointing these sites in the cavity surface where emitted electrons collide (Knobloch, 1997). Field emission is strongly related to the cavity fabrication conditions, in particular, to the cleanliness of the different steps in this process. Sites of electron emission usually consist of particles from elements other than niobium that attached to the surface of the cavity during processing. Fine particles of elements such as carbon, indium, copper, titanium, aluminum, silicon or calcium have been characterized in sites of emission in niobium cavities using SEM. Condensed gases such as water vapor have also been shown to cause field emission from particles attached to the cavity surface. These gas residues can trigger the formation of arcs that eventually explode and melt the emitting particle generating a characteristic starburst pattern (Padamsee, 1998).

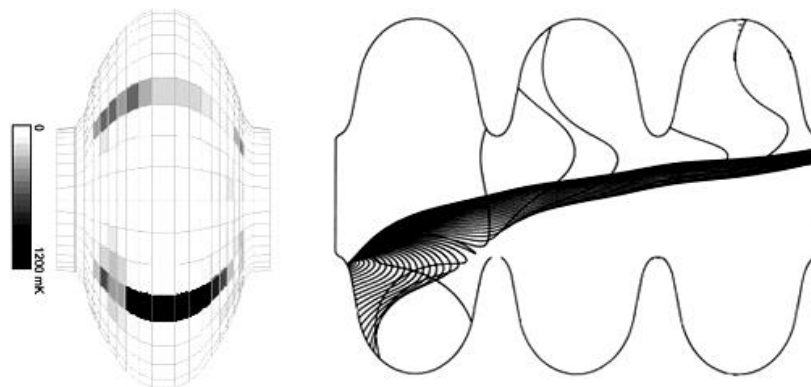


Figure 2.9 – Trajectories of bent electrons striking the surface of a cavity during field emission. From: (Padamsee, 2001).

2.8.3 Thermal Breakdown (Quenching)

The thermal breakdown or quenching of superconductivity is an effect that results when the RF losses are higher at a defect sites that are normally sub-millimeter in size. Quenching limits the accelerating field that can be used. As the field is increased, the temperature of the niobium near the defect surpasses the critical temperature T_c causing unstable dissipation of power and the breakdown of the field (Figure 2.10).

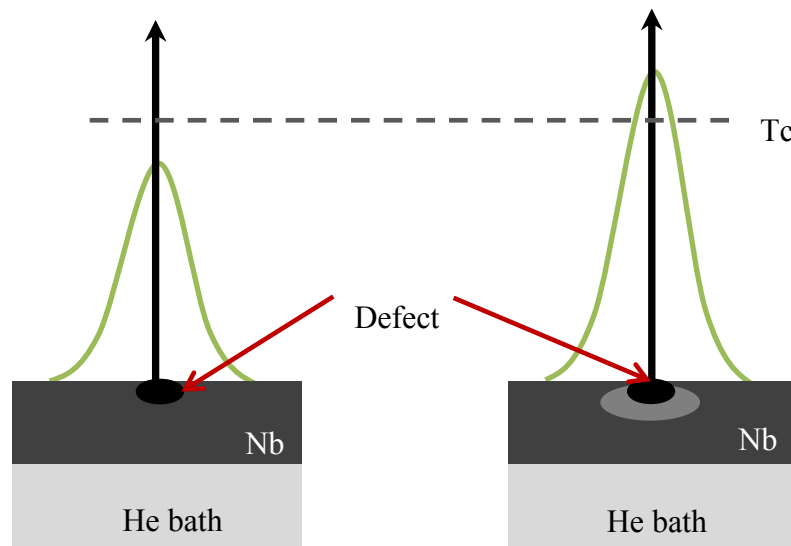


Figure 2.10 – a) At low fields, the temperature of the near the defect remains below T_c but at higher fields b) T_c is surpassed and power dissipation by niobium causes field breakdown.
From: (Padamsee, 2001).

One kind of defect can result from imperfections in the surface of the niobium cavity. Surface roughness of approximately 0.1mm can lead to quenching (Champion *et al.*, 2009). Other kinds of defects include inclusions from foreign elements such as copper, tungsten or tantalum or traces of other elements including potassium, calcium and chlorine that are used during cleaning of SRF cavities. The equation shown below has been developed for describing the accelerating field (H) in terms of the thermal conductivity (κ), radius of the defect (a),

surface resistance of the defect (R_n) and the bath and critical temperatures (T_b and T_c) (Padamsee, 1998):

$$H_{max} = \sqrt{\frac{4\kappa(T_c - T_b)}{aR_n}}$$

Thus far, the most effective method to achieve the maximum gradient (H_{max}) is by increasing the thermal conductivity of the niobium such that defects can tolerate more power dissipation before becoming unstable (Padamsee, 1998).

2.9 Niobium

A rather complete and entertaining account on the origins of niobium has been written previously (Gupta and Suri, 1993). Niobium (Nb) is a gray, soft and ductile transition metal, with number 41 on the periodic table, and similar shiny aspect as that of stainless steel. Niobium has the highest critical temperature of all elements (9.2°K) and that is the reason it is employed in fabrication of SRF cavities. Some of the material properties of reactor grade niobium are shown in Table 2.1 (Matweb.com).

Niobium is extracted from niobium-tantalum concentrates, mainly pyrochlore or columbite-tantalite ores, using different processes that can include chemical reactions, chlorination, fusion by alkaline agents, and leaching with the use of organic solvents (Ayanda and Adekola, 2011).

Table 2.1 - Properties of reactor grade niobium.

Property	Value
Density	8.57 g/cm ³
Hardness (Vickers)	65
UTS	240 MPa
Yield	170 MPa
Modulus of Elasticity	103 GPa
Poissons Ratio	0.35

Niobium is mainly utilized as an alloying element to increase the strength of steel, nickel and cobalt-based aerospace superalloys, with only a fractional 1-2% used for pure niobium or niobium alloys applications (ASM Int., 1990). Because of its high melting point of $\sim 2467^{\circ}\text{C}$ niobium is used in combination with other materials to improve their mechanical properties at high temperatures (Schwartz, 2012). The rise on the use of this niobium as an alloying element originated early in the 1930's after findings were made that properties such as weldability, yield strength, tensile strength, and toughness of some steel alloys, showed improvement by the addition of small amounts of niobium to the alloy chemistry (Gupta and Suri, 1993). In nickel alloys such as Inconel 718, niobium participates in the precipitation of the strengthening phase Ni_3Nb usually referred to as γ'' (Davis, 2000).

2.9.1 Reactivity to Gases

Most gases do not attack niobium from room temperature to about 100°C . This property is not retained at elevated temperatures when reaction can occur with gases such as hydrogen, nitrogen, carbon monoxide and oxygen. The material starts showing oxidation signs at temperatures above 200°C when exposed to air. At temperatures of $\sim 400^{\circ}\text{C}$, exposing niobium to a pure oxygen environment can result in catastrophic oxidation and the material becomes brittle. Hydrogen will react with niobium at temperatures above 250°C which can lead to the formation of hydrides causing a loss of ductility as well. Reactivity with nitrogen starts at temperatures roughly above 350°C (Gupta and Suri, 1993). For superconducting applications maintaining a low content of elements such as hydrogen, nitrogen, carbon and particularly oxygen is of extreme importance. These elements tend to form as interstitial impurities that cause detrimental effects to the electrical and superconducting properties of niobium (Padamsee, 1998).

2.9.2 Reactor Grade Niobium

The purification of niobium is normally performed by a series of melting operations in atmosphere controlled furnaces. Detailed instructions for performing removal of most gas impurities (hydrogen, nitrogen, carbon, and oxygen) from niobium have been previously established (Koethe and Moench, 2000). An electron beam furnace is employed to purify niobium in vacuum conditions with precise melting rates and outgassing times to flush out impurities. Typical vacuum levels used during purification are 10^{-4} to 10^{-5} Torr. In the furnace setup (Figure 2.11), the electron gun melts the bottom of the niobium feedstock and it also hits the resulting niobium ingot maintaining a molten pool.

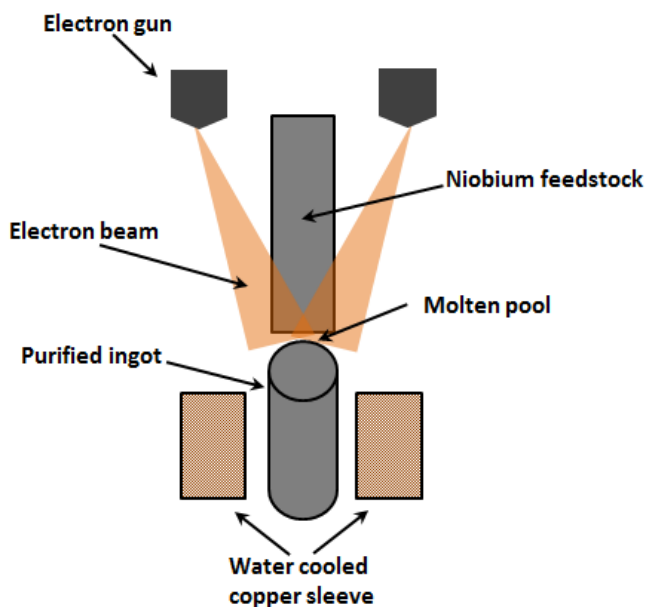


Figure 2.11 - Electron beam furnace for niobium purification. From: (Padamsee, 1998)

The purified ingot is continuously withdrawn through a water cooled copper sleeve at a coordinated rate with the melting rate of the feedstock ingot achieving removal of impurities (Padamsee, 1998). The impurity content can be evaluated by measuring the residual resistivity ratio (RRR) of the material. Although there is still debate in the physics community, the RRR has been accepted as the ratio of resistivity of the material at 300K and 4.2K (Singer *et al.*,

2010). Lower RRR values indicate higher concentration of imperfections such as substitutional or interstitial impurities. Reactor grade niobium has typical RRR values of 30. The use of multiple purification steps has resulted in the steady improvement of RRR values of commercialized niobium to values well over 500 (Chao and Tigner, 1999).

2.9.3 Powder Fabrication

The production of metal powder can be performed by several processes that can include gas atomization, water atomization, plasma atomization, centrifugal atomization, methods requiring the use of chemicals, and even milling and crushing of the feedstock material (Entezarian, 1996). For the EBM process, powders with a spherical morphology are preferred as they provide an increased ability to flow and achieve higher packing density. Argon plasma atomization was employed in the production of the niobium powder utilized in this work. In the atomization process, wire of material from a spool is fed at the top of multiple arc plasmas causing melting and atomization of the material in a single step. The argon environment allows for the processing of materials that can be reactive to atmospheric conditions maintaining the purity of the material. The cooling rates of the material are regularly one order of magnitude lower than those of other production processes like water atomization (Cooper *et al.*, 2000). The ionized argon reaches temperatures over 2000°K and this helps in delaying solidification until the point when surface tension achieves spheroidization of the material (Entezarian, 1996).

2.9.4 Properties of Niobium for SRF Cavity Fabrication

As it has been detailed in previous sections, SRF cavities are usually formed from niobium stock in sheet form. Careful control on the microstructure of the sheet stock is required for most forming processes. The use of niobium sheets with fine ($\sim 50\mu\text{m}$), fully recrystallized grains, enhances the formability process by preventing tearing (Compton *et al.*, 2000). A reduction in the number of dislocations is also preferred as dislocations present in niobium sheet, introduced during the rolling operation, are believed to affect the thermal conductivity and the

supported current of the cavity thus reducing its performance (Bieler *et al.*, 2010). Other mechanical properties requirements of high purity niobium for cavity fabrication, such as those used in the linear collider TESLA, are provided in Table 2.2 (Singer *et al.*, 2003).

Table 2.2 - Specifications of niobium for superconducting cavity production

Property	Value
RRR	> 300
Grain size	~50 μm
Yield strength	> 50 N/mm ²
Tensile strength	> 100 N/mm ²
Elongation at fracture	30%
Vickers hardness	≤ 50
Content of the main impurities	Ta ≤ 500 ; O ≤ 10 ; N ≤ 10 ; C ≤ 10 ; H ≤ 2

Chapter 3: Experimental Methods

3.1 Introduction

As discussed in previous chapters, there are many advantages in using niobium for fabrication of superconducting radio frequency (SRF) cavities. However, these benefits are undermined if the purity of niobium decreases during the fabrication process. The traditional methods of niobium cavity fabrication like deep drawing and spinning normally employ post-fabrication steps that include chemical or electrochemical cleaning and rinsing with ultra-high purity water to decrease the impurities present in the final part (Singer *et al.*, 2003). Measuring the residual resistivity ratio (RRR) is a way to assess the purity of a fabricated niobium RF cavity. Superconductivity applications normally require an $RRR > 300$ (Padamsee, 1998). The fabrication of niobium in EBM requires careful handling of the powder material to avoid prolonged exposure to environmental contaminants and high or ultra-high vacuum (UHV) levels throughout fabrication to prevent the development of interstitial impurities. The following sections in this chapter detail the steps taken to achieve stringent fabrication of niobium using EBM.

3.2 Upgrading Arcam A2 Interior

An upgraded interior for the Arcam A2 system was acquired and installed prior to the fabrication with niobium to maintain as pristine an environment as possible. The list of components for the upgraded interior is included in Appendix A. An Arcam's certified service engineer was in charge of the installation of the upgraded components and also of carrying out the preventative maintenance (PM) of the machine. According to Arcam, it is the first time that an upgrade procedure has been performed for any of their commercialized models. During this stage, the people involved in the assembly process for the upgraded interior wore nitrile gloves, tyvek® overall suits, and face respirators to minimize the amount of humidity in contact with different parts of the upgrade kit. Before installation, all components were cleaned using Durx® 670 wipers impregnated with isopropyl alcohol and then dried using compressed air to remove

any remaining dust or fiber particles. This cleaning process was performed twice for each component.

Referring to Figure 3.1, the parts in the upgrade kit of the A2 system included the following: two powder hoppers (1), one fabrication tray with redesigned powder delivery windows (2), one chain mechanism and its actuated rake (3), one stock vat (4), two powder sensor assemblies (5), one heat shield frame with new heat shields (6), and stainless steel covers to protect rake mechanism in the back and the observation port in front of the system (7). Other metal fixtures needed to attach the listed components above were also included in the update of the system.

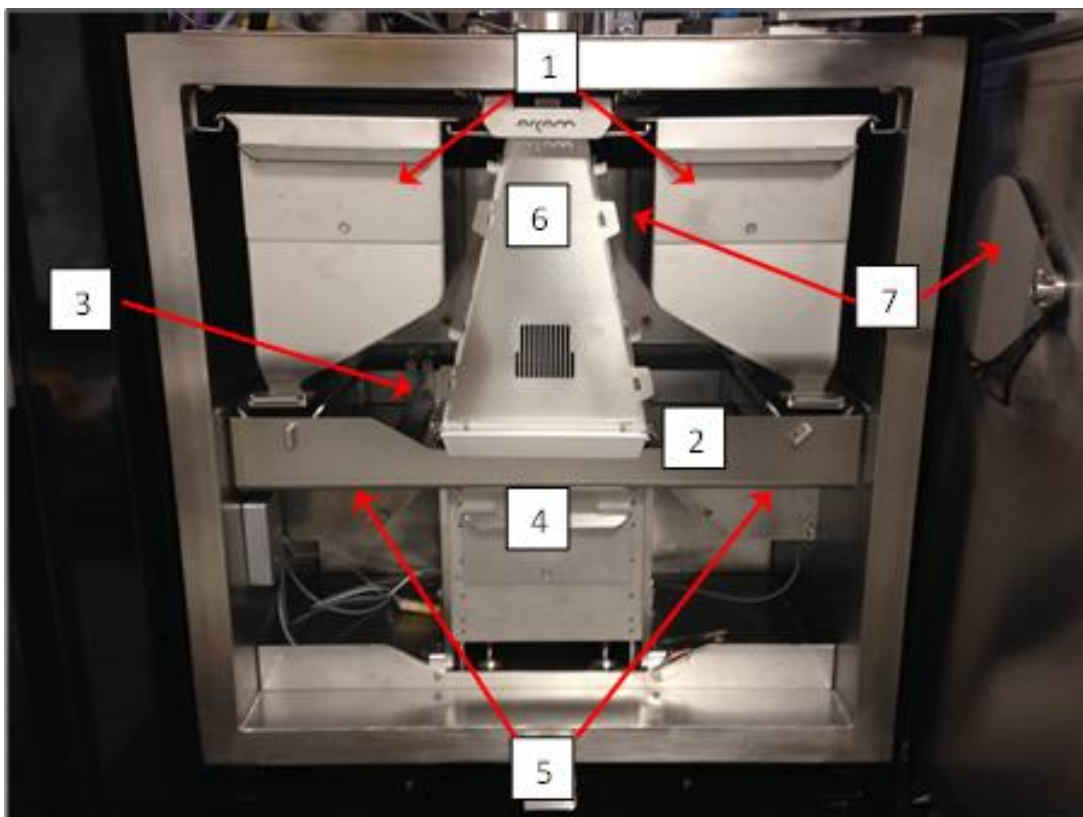


Figure 3.1 - Photograph of the A2 interior listing the major components upgraded during PM.

3.3 Cleaning of Chamber Components

Exceptions of parts upgraded for the A2 system were the fabrication chamber and the column where the electron gun is located. Portions of the walls of the chamber and door had a thick oxide buildup which was removed to prevent any of this material from falling into the niobium powder bed during fabrication. Similar oxide and metallization buildup was removed from the recess at which the column and chamber are connected and from a shutter mechanism that was installed to protect the view of an infrared camera. Although it is difficult to quantify, the material removed can contain elements (such as titanium and nickel) from other materials previously processed in the A2 machine and that can alter the purity of niobium powder. The oxide residue was removed by grinding using sand paper of 80grit and it was pulled from the A2 chamber with the use of a vacuum machine. Figure 3.2 shows the interior of the A2 system (with the stock vat and powder sensors already installed) after the cleaning step.

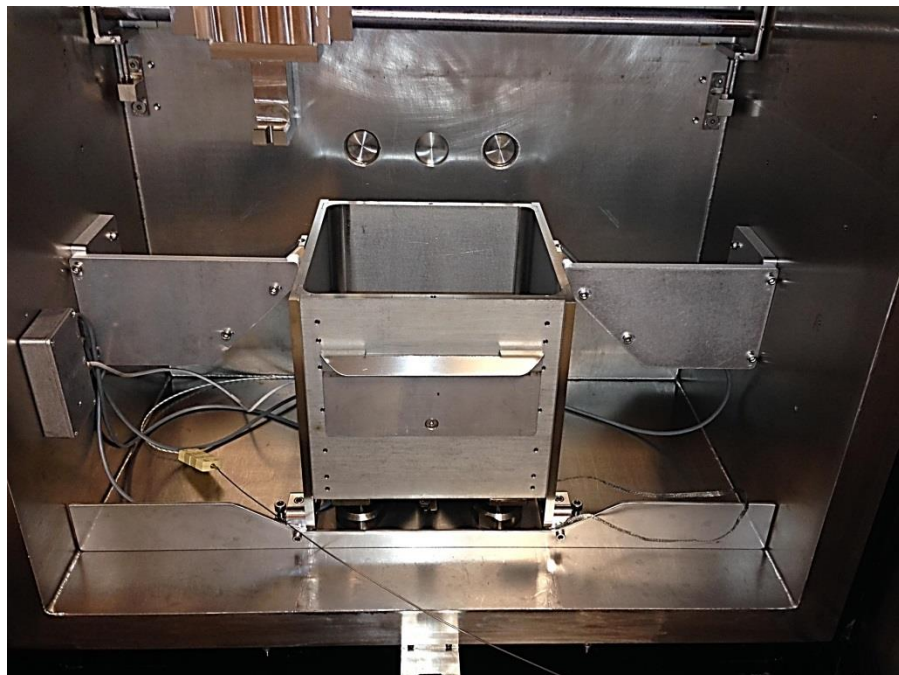


Figure 3.2 - Photograph of the A2's chamber after removal of oxidation and metallization.

The mini-vat assembly (section 3.6), used for fabrication, was also cleaned before any contact with the niobium powder occurred. This step was carried out to remove particles from nickel or titanium base alloys that might have remained from previous use of the mini-vat in the development of process parameters for such materials. All components in the mini-vat assembly (cylinder, piston arm and stage, a support plate, and threaded bars) were manually cleaned using wipes and a mixture 70% water to 30% Alconox[®]. This detergent is regularly used to remove oil and particulates from the surface of metal components without considerable damage from abrasion or corrosion. The mini-vat components were wiped with water and Alconox[®] twice followed by rinsing with isopropyl alcohol and then drying in air.

3.4 Steps to Improve the Vacuum During Fabrication

One of the main goals of the project for Phase II was to achieve higher levels of vacuum during the fabrication of niobium components. Purification of niobium is carried out at vacuum levels of 10^{-4} to 10^{-5} Torr; therefore similar operating levels during EBM ensured conservation of the purity in the fabricated parts which can also indicate improvement of the performance of the material for superconducting applications. Previously in Phase I of the project, processing of niobium was performed in an Arcam S12 system operating at an average chamber pressure of $\sim 1 \times 10^{-5}$ Torr as monitored by a residual gas analyzer (RGA). In the second phase of the project, fabrication was assigned to an Arcam A2 system in which the logbook indicated vacuum levels seldom below 1×10^{-4} Torr. Several components of the system were replaced to improve the vacuum level reached by the system. These components included a new 10.5mm diameter o-ring or gasket for the door and an unused screen for the turbo molecular pump. The gaskets and walls of all vacuum feed-through passes that provide access to electronics and sensors, and which are located in the back of the chamber, were also wiped with isopropyl alcohol and reassembled. The vacuum clamps for the feed-through passes were tightened as well. The vacuum level of the column was also improved by cleaning the gasket and the metal surfaces where the column meets with the electron gun assembly. These measures improved the flow and suction capacity

of the Arcam A2 system. Measurements with the RGA for the initial tests of Phase II indicated the system was able to maintain an average chamber pressure of $\sim 1 \times 10^{-5}$ Torr at the pump down of vacuum.

3.5 System Calibration

As standard steps during the PM of the A2 system, the vat is aligned, and the rake and beam calibration procedures are performed. These steps have the goal to ensure the EBM system operates in the factory conditions recommended by Arcam. The system calibration was performed concurrently with the installation of some parts of the upgraded interior.

3.5.1 Vat and Rake Calibration

The first step in the process consists of the alignment of the walls of the vat relative to the z-stage of the machine. A dial indicator is placed atop the z-stage and its probe in contact with one of the walls of the vat. The stage is then moved up and down (~ 100 mm), and as it traverses, the dial will indicate if there are any slight inclinations along the x or y directions of the current vat wall against the level set by the stage. The inclination in each wall can be adjusted by performing incremental changes to the supporting bases fixing the vat to the chamber floor. The process is repeated for all four walls of the vat until all measurements are within a $50\mu\text{m}$ ($0.002''$) tolerance recommended by Arcam.

A similar procedure is performed to align the rake mechanism. This step ensures that the powder bed is evenly distributed. To start the procedure, an L shaped fixture is attached to the arm that normally holds the rake in place. This fixture is then set against the probe of the dial indicator that is again placed atop the z-stage of the Arcam system. Starting with the probe midway in the L shaped fixture, the z-stage is moved approximately 100 mm down and this reveals any changes in the inclination of the rake mechanism. Depending on the faces probed, adjustments are made in either the x or y directions (relative to the powder bed) until the variations from the maximum to minimum are below $50\mu\text{m}$. The inclination of the rake

mechanism along the x axis was adjusted by turning support screws holding the assembly from underneath, while shims of metal with various thicknesses were placed in the back of the rake assembly to fix the inclination in the y axis. Figure 3.3 shows the dial indicator (1) and L shaped fixture (2) utilized for the rake calibration.

3.5.2 Beam Calibration

The final step in the PM procedure for the A2 machine consisted of the calibration of the electron beam. First, having the machine at atmospheric pressure a new filament is installed. The chamber is also accessible, and a calibration plate is fitted inside the stock vat and over the z-stage of the machine. The rake is moved to the center position and then the z-stage incrementally moved up until only a very small gap separates the calibration plate from the teeth of the rake. As the calibration plate is elevated small inclination adjustments might be required by turning screws embedded in it. The screws are turned until the calibration plate rests entirely



Figure 3.3 Rake calibration process.

leveled in one plane. The z-stage is continued to be moved up and once a small separation between the rake and calibration plate is achieved, the rake can be moved to either of the rest positions. The powder containers and heat shield assembly are then placed inside the machine chamber. In the heat shield, a modified front shield is used which allows observing the beam during the incoming stages of the calibration process.

In the next step, vacuum is pulled into the chamber until reaching a minimum value of $\sim 10^{-3}$ mBar. Then, the beam can be turned on and the actual beam calibration is performed. With the beam on at a current of ~ 1 mA, the arrow keys in the keyboard are used to center the beam inside 49 holes with a diameter of ~ 0.5 mm and which are set as a 7x7 grid in the calibration plate (Figure 3.4). The beam is considered centered once it disappears from the view as it goes into the hole. Each center position is saved in the calibration theme of the system.

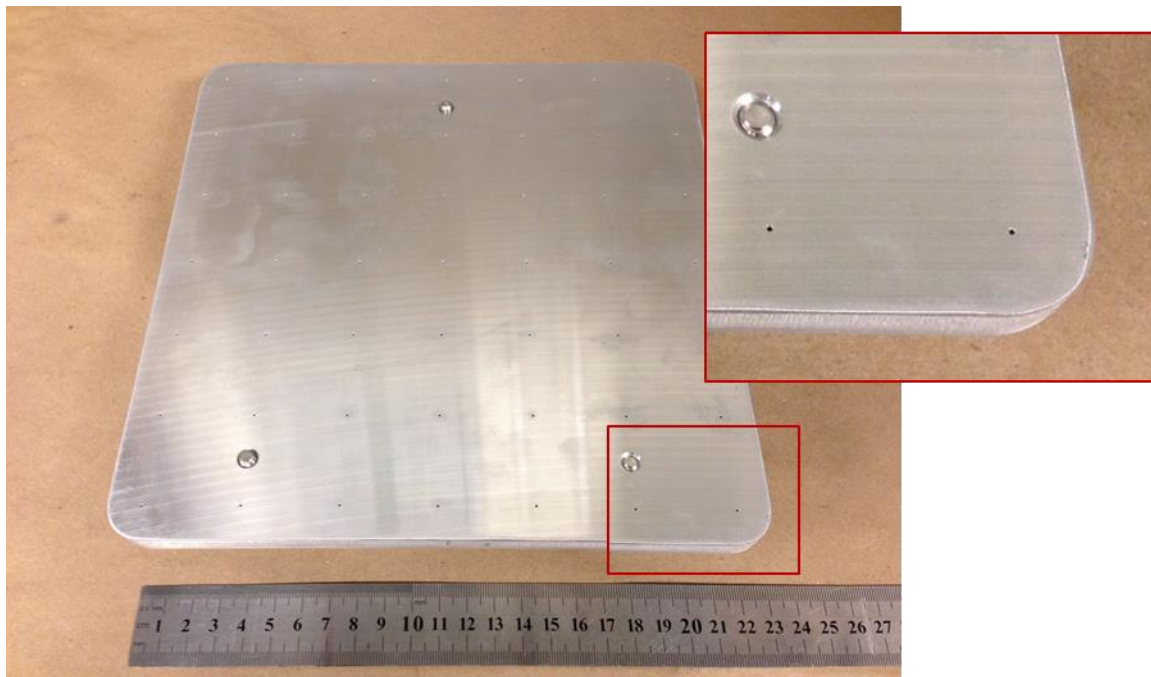


Figure 3.4 - Beam calibration plate showing an amplified view of two calibration holes.

Following the centering of the beam, the focus and astigmatism calibration procedures are performed. To calibrate the focus, the beam is set just next to a hole in the calibration plate where it is visible. Then, the focus values (mA) are adjusted which causes the spot size of the beam to grow or shrink to corresponding increments or decrements. In this manner the focus value is adjusted for each one of the 49 positions in the calibration plate until the beam is a single and small spot.

Astigmatism calibration is a similar process as with the focus of the beam. Visually, the objective is to align the beam into a single track along a particular axis. This procedure is performed for both the x and y axes relative to the powder bed. In the calibration screen, the system automatically positions the beam right next to a hole in the calibration plate and the astigmatism values can be tuned in the x and y directions. As the values are adjusted, the beam will grow into an oval shape or shrink into a single beam line. The astigmatism is considered

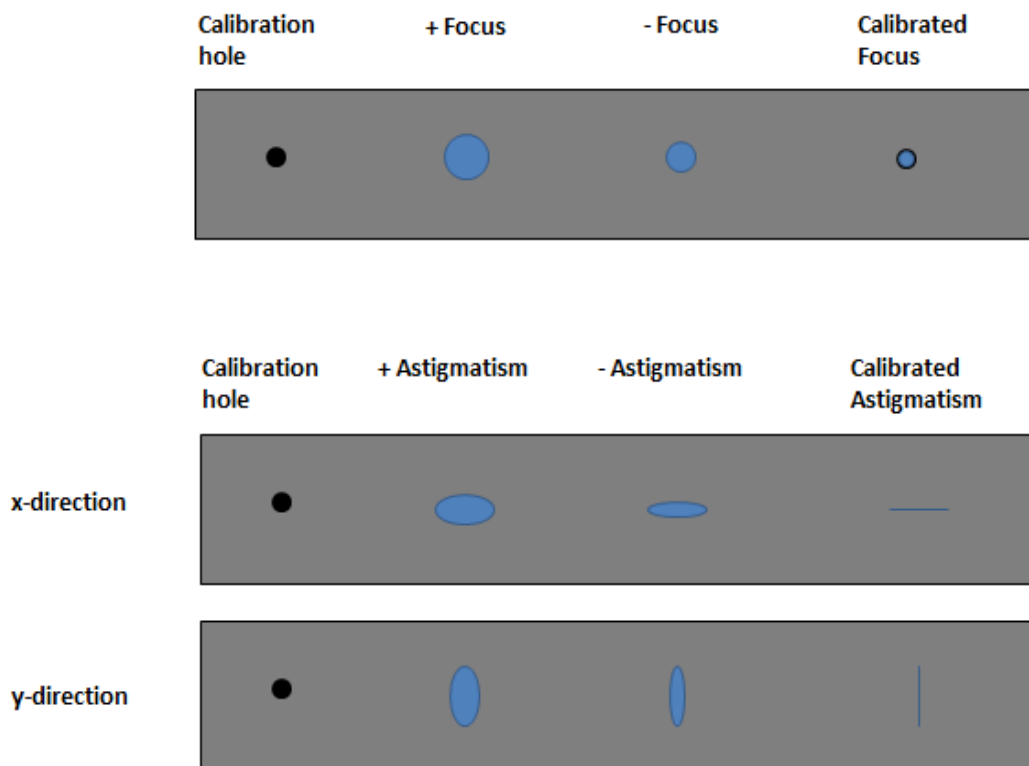


Figure 3.5 – Focus and astigmatism calibration of EBM system.

calibrated when only a single track is visible in either axis. Figure 3.5 shows a schematic of the focus and astigmatism procedures for the EBM system.

The final step in the beam calibration sequence is the run of a verification plate. In this step, the system is assembled with all components including a regular front heat shield and hoppers. Instead of a calibration plate, an unused stainless steel verification plate measuring 250 x 250mm is placed over the z-stage and aligned at a height where the rake is barely in contact with it. Then the verification project is loaded and run. The marks produced by the electron beam in the verification plate (Figure 3.6) are analyzed to ensure the beam has the proper focus and astigmatism values.

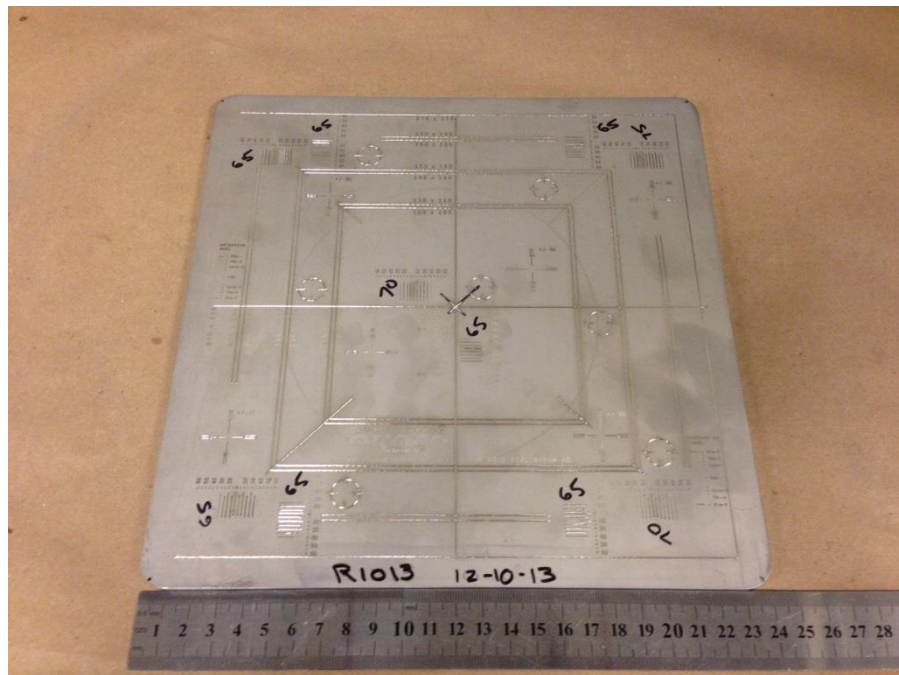


Figure 3.6 - Verification plate used in beam calibration of the A2 system.

3.6 Mini-vat

The fabrication of niobium in the EBM system was performed using a miniature vat (mini-vat) that was developed at the Keck Center. The mini-vat was conceived to test the candidacy of some powder metals for fabrication using the EBM process and it has been used for

parameter development of various materials. Two versions of the mini-vat have been employed and both possess smaller fabrication envelopes in contrast to the stock vat. Because of this characteristic, with the use of either mini-vat, the setup of the machine, experimentation to develop processing parameters, and ultimately part fabrication require less material. The reduced fabrication envelope has provided an ideal test platform for materials with limited stock and it has also helped to speed up the parameter development process. Shorter times to cool down the system allow performing experiments without much delay in between. The reduced volume of material also provides for faster setup times.

An envelope comparison of the mini-vat against the regular A2 vat reveals that while the latter would require approximately 9.15Kg of niobium powder (based on an average apparent density of niobium powder of 5g/cm^3) to perform the recommended setup including the powder bed and start plate, the mini-vat only needs 0.765Kg. Based on this volume comparison, approximately twelve times less material are needed to setup the powder bed and start plate in the mini-vat in contrast to the stock vat. One of the drawbacks of the mini-vat is that it has a limitation on the height of the parts that can be produced. In the configuration used with the

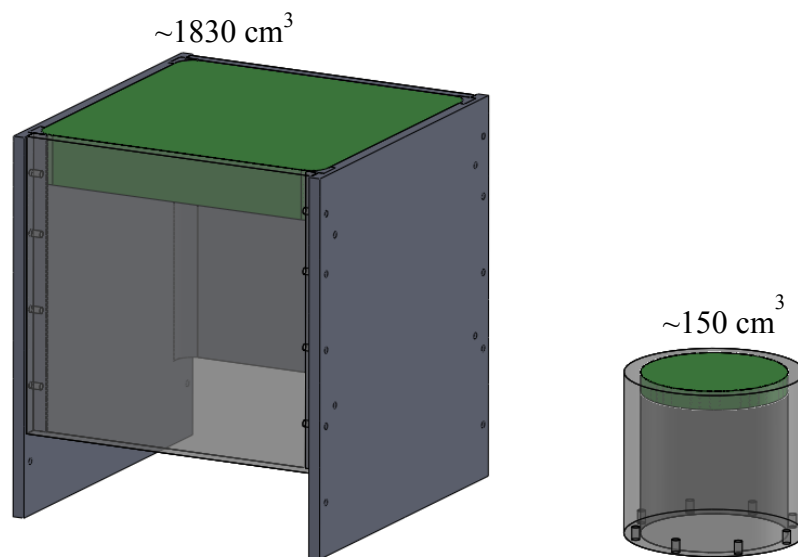


Figure 3.7 - CAD models of the A2's stock vat and the mini-vat cylinder used for fabrication.

Arcam A2 system, the physical limit was measured at just below 90 mm. The CAD models of both the stock vat and mini-vat are shown comparatively in Figure 3.7.

The configuration of the mini-vat used for processing of niobium consists of a stainless steel cylinder and piston assembly that is reconfigurable to mount in either of the stock vats for the A2 or S12 Arcam systems. As shown in Figure 3.8, this five part assembly includes the vat, a cylinder with an inner diameter of 114mm (1), one piston arm (2), one circular piston plate (3) which serves as the moving stage for the mini-vat, and a square shaped plate (4) to which the cylinder is attached. Threaded bars on all corners of the support plate provide the means for adjusting the height of the entire assembly depending on which machine it is being used. The last part of the mini-vat assembly consists of a square cover plate with a thru hole and pocket design (5). This part was machined from the regular fabrication stage used in the generic Arcam A2 machine and it attaches atop the cylinder to provide a flatbed that is leveled at the same height of the updated fabrication tray (6).

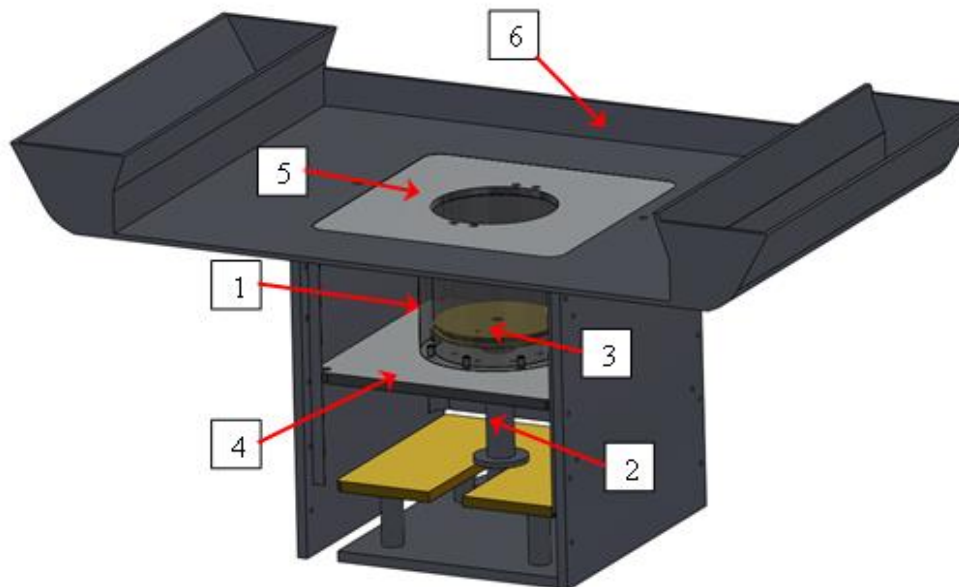


Figure 3.8 – CAD rendering of the mini-vat configuration in the Arcam A2 system used for niobium fabrication.

3.7 Material Handling

3.7.1 Ventilation with Nitrogen

In the regular fabrication cycle as recommended by Arcam, once a part has been finished the system is cooled down with assistance by a purge of helium gas. Once the temperature below the start plate has reached what is considered a safe level at or below 100°C, the chamber can be ventilated using air until the part cools to room temperature. For the processing of niobium, ventilation with neither helium nor air was advised as these gases contribute to the absorption of impurities by both the recycled powder and the fabricated parts. Therefore, ultra-high purity dry nitrogen (N₂) tank was connected to the A2 system that permitted ventilation of the chamber with this gas. The selection of nitrogen was adequate as it does not react with niobium up until ~ 350°C and since its relative higher partial pressure, compared to that of moisture, delayed absorption of the latter into the EBM chamber once the door was opened. In the ventilation process, once a part was finished, it was allowed to cool-down to ~ 50°C without the regular helium purge. Depending on the size of the part built, the process lasted from 10 to 15 hours. Once the chamber of the A2 was at this temperature it was ventilated with N₂ and then the system opened to extract the part.

3.7.2 Handling Process

To minimize exposure of niobium powder to ambient conditions, the material was collected from the machine and sifted for reuse inside a portable glovebox (Figure 3.9). The relative humidity within the glovebox was maintained at 4-5% by regularly injecting N₂ gas. The positive pressure created by the nitrogen prevented moisture from coming into the glovebox thus maintaining a low relative humidity.

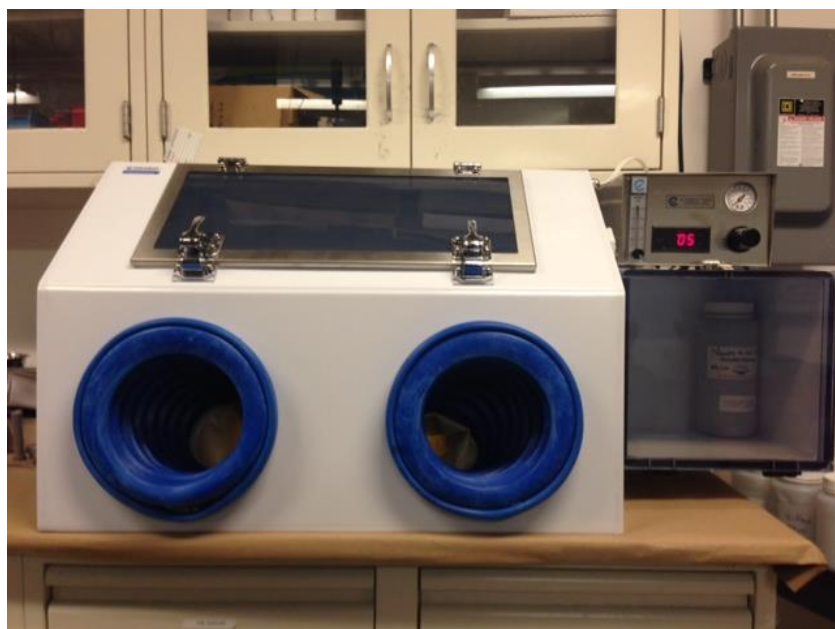


Figure 3.9 – Glovebox unit used for handling and sifting niobium powder in a N₂ atmosphere.

The longest time of exposure of niobium to atmosphere was at the time when powder from a run was recollected and while the setup for the next build was carried out. The next list of steps was followed to reduce exposure of the material to the environmental conditions (particularly humidity):

1. Ventilation of A2 chamber and glovebox with N₂ gas.
2. Re-collection of powder from fabrication chamber.
3. Sifting of powder inside glovebox in the N₂ atmosphere
4. Pouring of sifted material inside the powder container or hopper.

3.8 Monitoring the Material Purity

3.8.1 Chemical Analysis

To analyze the purity of powder niobium, samples were sent for elemental analysis. RadiaBeam outsourced this process to Element Materials Technology, USA where elemental tracing was performed by using ICP, Fusion for H, O and N and LECO combustion for C. In Phase I RadiaBeam conducted the chemical analysis from the ingot material, feedstock wire, powder after atomization, and for EBM niobium. Chemical analysis of powder samples from Phase I and Phase II as well as for EBM niobium fabricated using Phase I material was conducted in this study.

3.8.2 Residual Gas Analysis

An RGA-100 residual gas analyzer (SRS, USA) was installed in the A2 system to monitor the quality of the vacuum during fabrication with niobium. The system was used to monitor the EBM process for fabrication with niobium and it provided a measure of impurities present inside the fabrication chamber. This is done by recording the partial pressures for many different gas species that can react and affect the purity of niobium including nitrogen, carbon dioxide, water vapor, oxygen, hydrogen and helium. The RGA unit was connected directly to the A2 using one vacuum pass-through available on the back of the chamber (Figure 3.10). To operate the RGA, vacuum was pulled normally into the EBM system until it reached a value below $\sim 10^{-4}$ Torr (1.3×10^{-4} mBar). At this point the RGA filament was turned on and measurements were recorded using the RGA software interface.

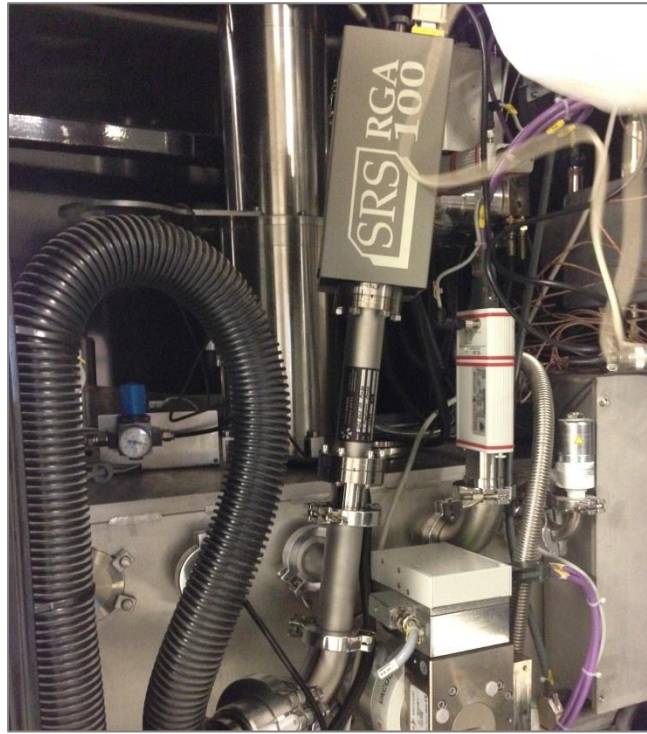


Figure 3.10 – RGA unit installed on the Arcam A2 system.

3.8.3 Vacuum Leak Detection

The RGA-100 unit was also used for detection of vacuum leaks occurring in the A2 system. In the leak detection mode, once the chamber on the EBM system reached $\sim 10^{-4}$ Torr helium gas was ventilated in possible sites of leak which included the perimeter of the door and also at each vacuum pass through into the chamber. The locations where gas leaking was happening were indicated in the RGA plot as sharp spikes for the partial pressure of helium. This diagnostic tool helped in the identification of a major leak in the door that was later fixed during the PM of the machine by replacing the door gasket.

3.8.4 X-Ray Diffraction

The X-ray diffraction technique (XRD) was used to characterize niobium powder samples and EBM-fabricated niobium parts. Since the niobium material is of high purity, the XRD analysis will also allow identifying impurities present in both powder and solid specimens.

3.9 Material Characterization

Two niobium powder batches were used for fabrication using the EBM process. To distinguish these materials they were catalogued as Phase I and Phase II powders. The characterization of the powder material was performed as described in the following sections.

3.9.1 Flow Rate and Apparent Density

As previously noted, good flow of the material is an indication of the suitability for using a given powder for fabrication with the EBM. The two powder batches were analyzed following the B213-13 ASTM standard designation. Using this method, flow of the material was calculated by allowing a weighed mass of 50 grams of material to flow through the orifice of a Hall Flowmeter funnel (ACuPowder International, USA). The mass of material was placed in a previously clean and dry funnel which has a calibrated orifice of 2.54 mm in diameter. The funnel is supported by an arm and stand (Figure 3.11). The 50 grams of dry powder were placed in the funnel while the orifice was covered. As the orifice was unblocked, material started to flow and a stopwatch was used to capture the time it took for the entire mass of material to go through the funnel. One tap on the side of the funnel was permitted to assist the start of the flow of powder if it did not flow on its own (Standard, ASTM B213-13).

Another qualification for use of a powder material in EBM is the measure of the powder's apparent density. As it has been mentioned before, Arcam recommends the use of powder with an apparent density of at least 50% that of the density of the bulk material. Measurements of the apparent density for niobium powder were done using the Hall flowmeter funnel setup and following the specifics in ASTM B212-09. In this process, a test volume (30 to 40 cm³) was allowed to flow into an empty density cup, with a volume of 25 cm³, which was weighed to the nearest 0.01 g. Once the density cup was full, the powder in the cup was leveled using a spatula. The density cup with the metallic powder was weighed once more to determine the mass of the test volume. The calculation of the apparent density (Hall) was done by dividing the mass value by the volume of the density cup. Density values were reported to the nearest 0.01 g/cm³ (Standard, ASTM B212-09).

3.9.2 Optical Metallography

An optical microscope was used to characterize the niobium material at different stages during the fabrication trials. Prepared specimens were observed using a Reichert MF4 A/M (Reichert, USA) and images were acquired using a digital camera. With this setup, images were



Figure 3.11 – Hall Flowmeter funnel and density cup.

acquired for niobium powders and from EBM fabricated niobium parts.

Niobium powder was mounted in resin and ground and polished to see internal features that cannot be seen using other methods. The process consisted of pouring a quantity of niobium powder along with resin in a small container. Once the resin had set, the specimen was ground to ~1000grit sand paper and etched using a solution of 1:4 parts of HF and HNO₃. In the case of EBM fabricated niobium coupons, they were also mounted in resin, ground and polished to a mirror-like finish. First, the specimens were ground using increasing finer grit papers from 80 to 1200. Then, a suspension of water with fine alumina particles was used to polish the surface to be observed. To reveal the microstructure in more detail, the exposed surfaces were etched using a solution of 30mL HCl, 15mL HNO₃ and 30mL HF as described before (Martinez *et al.*, 2013).

The average grain size of the material was obtained by using the average grain intercept method (AGI). In this method, lines are drawn at random orientations in the microstructure and the number of intercepts of each line counted. Then the average grain size can be estimated by dividing the number of interceptions over the length of the traced line in the correct units as indicated by the micrometer mark in the image.

3.9.3 Scanning Electron Microscopy

Higher resolution imaging, using scanning electron microscopes, was employed to characterize niobium in the precursor powder form and in the EBM as fabricated condition. Using a TM-1000 table-top scanning electron microscope (Hitachi, Japan) powder specimens were observed in detail. The obtained images from the powder were used to quantify the particle size distribution for the different batches of niobium powder used. A collection of particle sizes from different magnification SEM images was obtained and used to construct the particle size histogram, as it will be discussed in the results section.

SEM imaging was also used in the analysis of the fracture surfaces from tension experiments. In this case, fractured specimen were mounted in the holder for the SEM and

analyzed in the normal to fracture direction. Then, the specimens were also inserted at an approximate angle of 45 degrees and observations were made in this orientation as well.

3.10 Mechanical Properties

3.10.1 Tension Testing

The significance of the tension test is that it provides the strength and ductility properties of a material when subjected to uniaxial tensile stress. The test provides useful information on the resistance of the material in the uniaxial loaded condition. Results might not be necessarily applicable for the part under different loading conditions such as those experienced during service and/or environments in the specific application.

Using the tension test according to the specification of the E8/E8M ASTM standard, properties such as the yield strength, elongation, ultimate tensile strength and reduction in area were obtained. Testing was performed in a MTS Landmark Servo-hydraulic test system (MTS Systems Corporation, USA) using closed-loop control with a set straining rate of 0.015 ± 0.006 mm/mm/min. All experiments were performed, in accordance to the standard, at atmospheric conditions and with negligible variation in temperature. Sub-size specimens with a rectangular cross-section were machined from EBM niobium coupons. The type of specimen selected had the proper dimensions for fabrication from the available niobium coupons while adhering to the E8/E8M ASTM standard. The setup used for tension testing is shown in Figure 3.12. As per the ASTM standard, sub-size specimens were machined using 12x12x80 mm EBM niobium coupons that were built in the z-direction. All the dimensions of the E8 sub-size specimens are described in Figure 3.13 in units of millimeters.

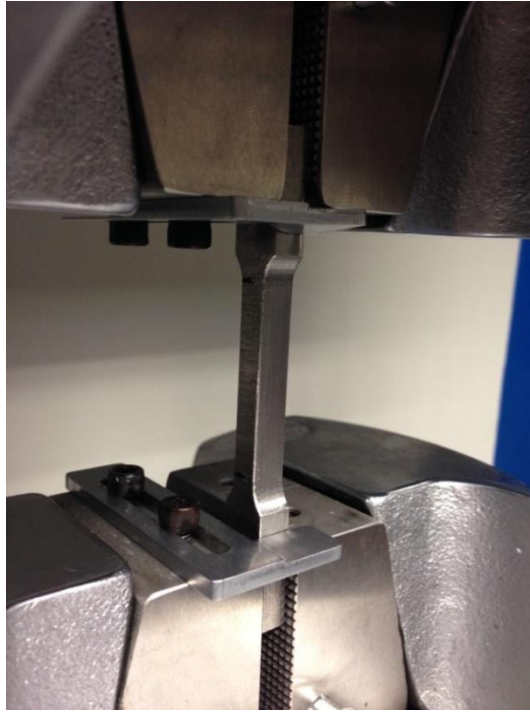


Figure 3.12 – Tensile test setup utilized showing tensile specimen held by the grips in the MTS machine.

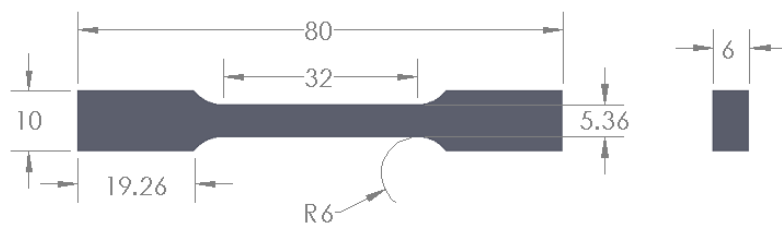


Figure 3.13 – Nominal dimensions of fabricated E8/E8M tension specimens.

Given the dimensions in the sub-size specimens used and with the expectation of a percent elongation in the range of 30-50% for the EBM niobium, the available extensometer could not be used to measure the elongation at fracture for specimens. Instead, digital video was recorded of the tensile test for each specimen and the distance between two punch marks or notches was measured in the initial and final frames of the video. Using this method, the percent elongation could be estimated for EBM niobium. The visual or manual measurement of material elongation has a +/- 2% error associated to it (Davis, 2004). More sensible devices as extensometers have error in the range of +/- 0.25% to +/- 1% (Standard, ASTM E83-10a).

The load and displacement measurements recorded by the MTS machine were used to calculate stress and strain. Stress was calculated from load values from the machine and using the area of the specimen cross section at the gauge (average of ~32.8mm²) using the equation below (Davis, 2004):

$$\sigma = \frac{P}{A}$$

Strain was calculated from the actual elongation of the MTS machine. The values for ultimate tensile strength (UTS) were measured directly as the maximum stress value in the engineering stress-strain curve. The yield strength was obtained using the 0.2% offset method by analyzing the stress-strain curves obtained for each specimen. In the linear portion of the stress-strain diagram for each specimen, a linear regression fit was used with R² coefficients greater than 0.99. The slope of this line was then used to draw a parallel line at the 0.002 strain mark and values of yield stress obtained from the intersection of this line with the curve. Appendix B provides plots for all specimens tested in the linear region showing the linear regression analysis.

In general, evaluation of the percent reduction of area for rectangular test specimens is difficult because the final shape after fracture does not remain rectangular but rather the edges bend non-uniformly towards the center of the part while the corners remain for the most part

constrained (Figure 3.14). Expressions developed to attempt the calculation of the percent reduction in area have no general consensus (Davis, 2004).

In this work, an approximate value was calculated by analyzing stereomicroscope images of the fracture surfaces of tension specimens. This was achieved with the use of a boundary detection code, programmed in Matlab (The Mathworks, USA), that segmented and applied a threshold to the binary of the original image and then provided the measure of the bounded or detected area as a number of pixels. The marker in the image was then used to calculate the area of a single pixel in square millimeters (mm^2). Multiplication of the previous two values gave the area of the detected region in mm^2 that was compared against the original measured area of the machined specimens to approximate the percent reduction in area.

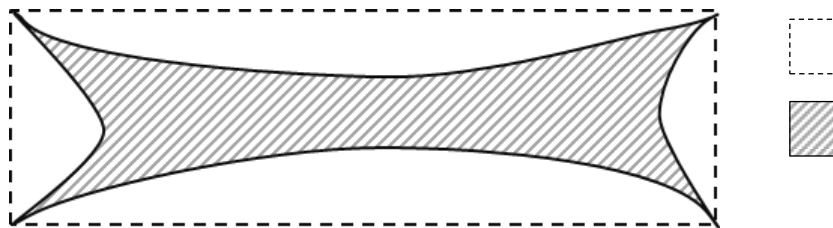


Figure 3.14 – Original and final areas of square specimens after tension test has been performed. From: (Davis, 2004)

To test the effectiveness of the code in detecting the area of a region, a square shape was placed in one original stereomicroscope image with each side measuring the length of the marker (0.5mm). The exact area for this shape is 0.25mm^2 . After analysis with the code, the area calculated for the square was 0.2476mm^2 which corresponds to less than 1% error in measurements, and therefore the technique was employed.

3.10.2 Hardness

Hardness measurements were performed in an Instron Wilson Rockwell Series 2000 (Instron, USA) using a 1/16" ball at a load of 60kgf. Measurements were done in the hardness

Rockwell F scale and converted to Vickers hardness values using published data available online at (<http://www.gordonengland.co.uk/>). The hardness of the material is important to qualify the density of parts. Lower hardness values could indicate regions of sintered rather than melted powder which could also have an effect on the mechanical properties of fabricated parts such as the yield strength.

The hardness of EBM niobium was measured in the horizontal and vertical planes of reference (i.e. parallel and perpendicular to the fabrication direction) using square bars with as-fabricated dimensions of 12x12x50mm. Bars fabricated with Phase I and Phase II powders were analyzed. Three square bars were cut at heights of ~20 and at ~40mm and measurements taken in these surfaces in the horizontal plane. A total of five measurements were done in each bar. Three more rectangular bars were cross-sectioned and hardness values measured in the vertical plane of reference along the height of the part in intervals of ~2mm. For comparison purposes, measurements were also made for the WRG niobium in the axial, longitudinal, and transverse directions.

3.11 Physical Properties

Aside from the mechanical properties of the EBM niobium, RadiaBeam had interest in characterizing physical properties that included density and the thermal conductivity. The density of the material was measured using the ASTM standard B311-13. The thermal conductivity was measured using the transient plane source method by ThermTest Inc. The RRR was also measured for EBM-fabricated niobium at the vertical test area setup (VTA) at JLab. The following sections provide more detail of the techniques used in measuring the physical properties.

3.11.1 Apparent density

Similar to the effects of impurities, the presence of porosity or similar defects are detrimental to the SRF properties. Such surface defects limit the accelerating electromagnetic

field that can be used for experiments by the occurrence of quenching (Champion *et al.*, 2009). To improve the density of parts obtained by the EBM process, an experiment was designed that included building an array of nine parts measuring 10x10x10mm. Using the array of parts approach, variations of three influential parameters were investigated; across columns, the focus offset was varied while average current and beam speed were varied in each row (Figure 3.15).

		Focus Offset (mA)				
		30	31	30.5	Beam current (mA)	
Beam Speed (mm/s)	175	7	8	9	21	
	170	4	5	6	20	
	172.5	1	2	3	20.5	

Figure 3.15 – Schematic of fabrication parameter space explored during experimentation to improve the density of EBM niobium.

In each iteration, the parameters yielding the highest density were selected and used to explore a different but close parameter set in the following experiment. In this fashion, the density of EBM niobium was improved.

The apparent density of EBM parts was measured using the volume displacement method. This was done by following the process described in ASTM standard B311-13. As shown in Figure 3.16, measurements were done using a weighing balance with 0.001 g precision (1) and a density measuring kit consisting of one stand (2), one bracket (3), one weighing basket (4) and one nalgene beaker (5) to hold distilled water. The kit was assembled by resting the bracket atop the surface of the scale. The basket was suspended from the bracket into the empty beaker. The beaker was held in place by the plastic stand.

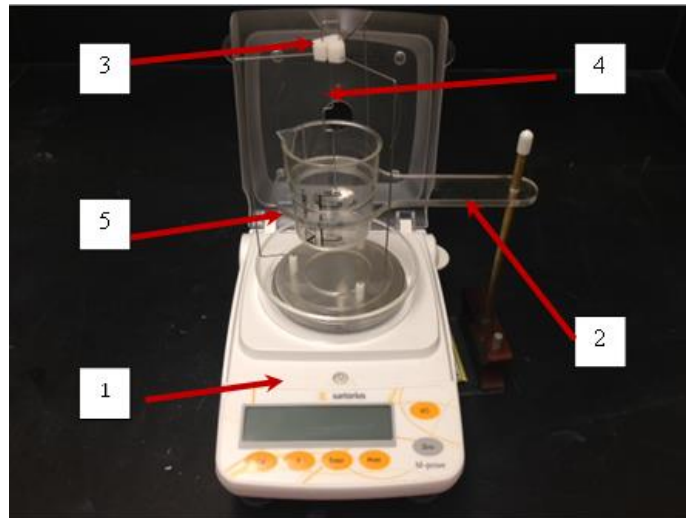


Figure 3.16 – Density measurement kit used for EBM niobium parts.

Weight measurements were made by weighing the part of interest in air and then in water. Then, the apparent density of parts was calculated by the following formula $D = (A \times E)/(A - F)$. The percent relative density (%RD) for parts was calculated by dividing the obtained density values over the density for wrought reactor grade niobium (WRG) of 8.57g/cm^3 . Reported values were the average from three measurements for each part. In this formula, A was the mass of the test specimen in air, F was the mass of the test specimen in water and E was the density of water at the working temperature. Standard B311-13 provides a reference table of water densities versus temperature. Using this method, the density of EBM niobium parts was measured in the as fabricated conditions. Once the %RD of as-fabricated parts was optimized at >99%, a final experiment was performed using a ~80mm square bar in which the edges were machined. The bar was sectioned into five parts and density measurements taken. As will be discussed in the results, all five sections had greater than 99.5% RD. This was done to assess the relative density of parts with the optimized surface roughness as that required for SRF experimentation by RadiaBeam.

3.11.2 Thermal Conductivity

Thermal conductivity testing was also outsourced by RadiaBeam to ThermTest Inc., Canada. The method used for measuring conductivities was the transient plane source (TPS) method. EBM fabricated niobium discs measuring ~35mm in diameter by ~10mm in height were provided to RadiaBeam for measurement of the thermal conductivity. The discs were machined to smooth surfaces to allow testing. In the TPS method, a double metal spiral covered in kapton served as heat source and resistance thermometer. The spiral was sandwiched between a niobium disc and an insulating material (Figure 3.17). With this setup the thermal conductivity of EBM-fabricated niobium was measured at a temperature of 20°C. ThermTest Inc. carried out measurements by providing the TPS sensor with 0.5Watts for 2 seconds. Seven measurements were conducted for each niobium disc received. For quality assurance, ThermTest Inc. tested the same setup with the reference steel 8620 having a thermal conductivity of 46.6 W/mK and found errors in measurements to be below 1.7%.

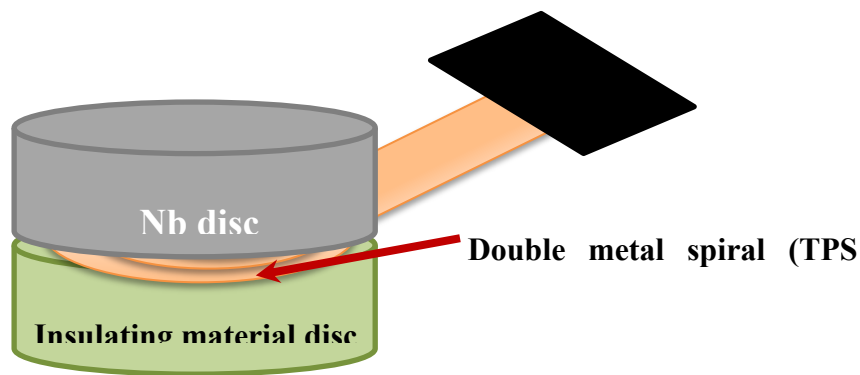


Figure 3.17 – TPS setup used by ThermTest Inc. showing the double metal spiral between the niobium and insulating material discs

3.11.3 Residual Resistivity Ratio

The RRR for the EBM niobium was characterized by RadiaBeam in collaboration with the Thomas Jefferson National Laboratory's SRF Institute (JLab, USA). Two niobium rectangular bars with dimensions of 10x45x35mm (shown in Figure 4.4 b)) were sent to JLab where 16 smaller sections were extracted for measurement of the RRR. JLab conducted these experiments in their Vertical Test Area (VTA) and provided direct measured results for the RRR of the EBM niobium specimens.

3.11.4 DC and RF Testing

The SRF properties of the material were also characterized at JLab using an in-house test design consisting of a single TE_{011} cavity. Ciovati et al. provided the details for the fabrication of a coaxial TE_{011} cavity as a system to measure the superconducting properties of a removable cylindrical sample (probe) with a center cooling channel (Ciovati *et al.*, 2007). As detailed in the next chapter, two niobium probes were fabricated with the EBM technology and provided to RadiaBeam for post-processing by machining of the parts prior to testing at JLab. The EBM fabricated niobium probes were ~85mm in height, smaller than the 120mm probes used regularly at JLab but their testing was possible. The limit on the height of the EBM parts was imposed by the dimensions of the mini-vat used for fabrication. Figure 3.18 shows photographs of the cavity fabricated at JLab and a sample niobium probe.



Figure 3.18 – Cavity fabricated at JLab and sample niobium probe used for SRF tests. From: (Ciovati *et al.*, 2007).

Chapter 4: Fabrication of Niobium in EBM

4.1 Previous Work

The literature regarding the fabrication of niobium by electron beam melting is rather limited. Small EBM niobium components were fabricated for the first time at the Keck Center in 2012 as part of the Phase I activities in RadiaBeam's grant. Observations of the microstructure and mechanical properties for parts produced with Phase I powder were described in a recent work (Martinez *et al.*, 2013). The microstructures obtained from the small specimens analyzed in this work consisted of elongated grains in the vertical direction. In the horizontal direction, the grains showed equiaxed morphology corresponding to the top of the columnar grains (Figure 4.1).

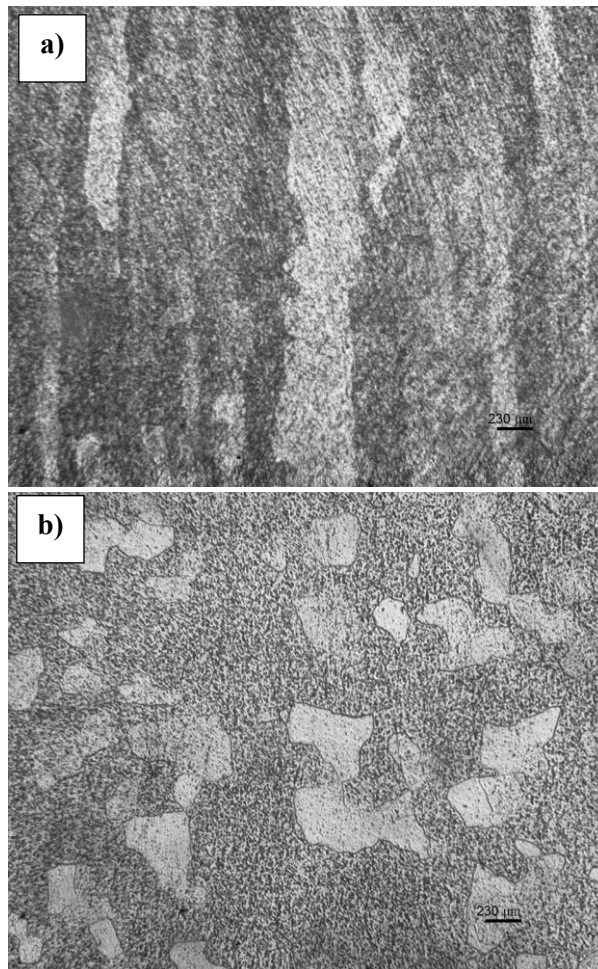


Figure 4.1 – Microstructures of EBM niobium in the vertical a) and horizontal b) directions. Image b) corresponds to the top of the columnar grains.

RadiaBeam also conducted work in the characterization of some of the properties of the EBM niobium constructs including the Vickers scale hardness, the density, and the RRR. Some niobium parts fabricated by EBM were sent by RadiaBeam to JLab to measure the RRR of the material. The results of these measurements are shown in Table 4.1. The average density of parts in Phase I was ~98.6%.

Table 4.1 – Properties obtained for EBM Phase I niobium parts

Parameter	EBM Niobium	Wrought Reactor Grade Niobium
Density (g/cm ³)	8.40 - 8.51	8.57
RRR	19 - 24.7	40
Vickers Hardness (Gpa)	0.82 - 0.86	0.76 - 0.85

Parts for Phase I were produced using an Arcam S12 machine and using a similar mini-vat configuration as that described for Phase II. During the fabrication trials in Phase I, it was possible to fabricate niobium in the EBM by introducing a delay in between the processing of each layer. This was necessary since agglomeration of powder occurred if the deposition of a fresh layer occurred right after the melting of the previous layer. It was observed that the delay helped in preventing the agglomeration and thus permitted the deposition of an even layer of material during raking. Processing times of ~150 seconds were observed during these fabrication trials at a temperature cycle that oscillated from ~590-640°C.

4.2 Processing Conditions in Phase II

The fabrication of niobium was carried out using an Arcam A2 system with a reduced mini-vat assembly. To follow a consistent setup method, the stage of the mini-vat was positioned at ~35mm. The volume from the stage to the top surface was filled with powder and

the build plate placed atop the powder. The single thermocouple from the system was put in contact with the back surface of the build or start plate.

In the normal EBM fabrication process three themes can be used; preheat, melt and net. This last step is only used whenever support structures are required in the build. The preheating step uses a defocused beam to pre-sinter the powder bed and it is followed by the melt step that is carried out using more focus and power on the beam. The themes are repeated for every layer processed. From previous fabrication trials of niobium during Phase I, a sequence of themes was identified that helped in the fabrication of the material. In addition to the preheat and melt sequences, a delay was necessary as it was observed that raking of the fresh powder layer right after the melt sequence resulted in agglomeration of the powder and uneven raking. This was evident as tracks left on the powder bed as the rake moved and dragged the agglomerates formed (Figure 4.2).

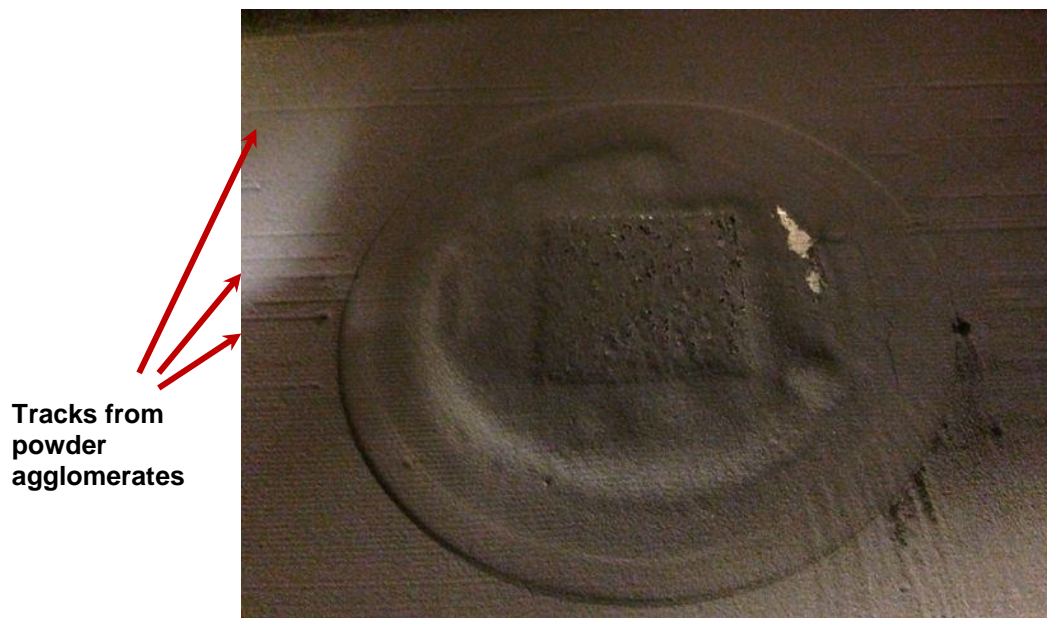


Figure 4.2 – Powder bed with tracks left by rake due to powder agglomeration. Study carried out during Phase I.

The delay required to prevent agglomeration and surface tracks in the powder bed was accomplished by adding an extra theme. This extra step consisted of a melt theme enabled in the manual mode and with zero currents and focus offset values. Using this configuration, the beam speed was varied and that increased or decreased the duration of the step without any more energy added from the scan. Because of the delay introduced, the temperature plot resembles a pattern with peaks and valleys (Figure 4.3).

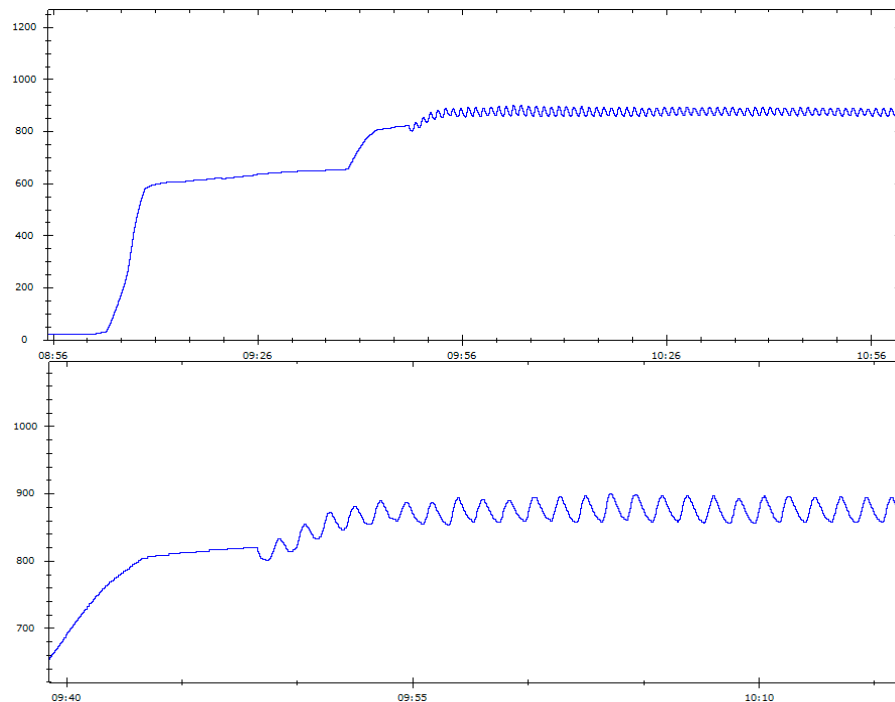


Figure 4.3 – Top: temperature profile captured by thermocouple during EBM fabrication of niobium. Bottom: Close-up view.

The apex of each peak corresponded to the end of the melting sequence. The following decrease in temperature corresponded to the delay time to cool down the surface along with the raking of the fresh layer. At the conclusion of the raking step, the minimum value in temperature was reached in the cycle and then the heat started increasing during the preheating of the next layer. As can be seen in the plots below, the fabrication of niobium was performed in a temperature cycle that reached a maximum at $\sim 890^{\circ}\text{C}$ and decreased to $\sim 840^{\circ}\text{C}$ at the minimum

value after the delay. It is interesting to note that no reliable fabrication of pieces could be done using the temperature ranges obtained from Phase I. With the preheat theme used for each layer, powder smoke was always observed at temperatures below $\sim 700^{\circ}\text{C}$. During Phase I, fabrication was performed at temperatures in the range of $600\text{--}650^{\circ}\text{C}$. In the Phase II cycle, the duration of the delay was ~ 30 seconds. Total fabrication time for each layer was ~ 80 seconds.

4.3 Fabrication of Niobium Components

Most of the parts fabricated were done using Phase I powder. This approach was decided by RadiaBeam since optimal processing parameters were still under investigation. Several designs of interest were EBM fabricated using the Phase I niobium. Some of these designs included simple geometries such as rectangular bars and cylinders (Figure 4.4).

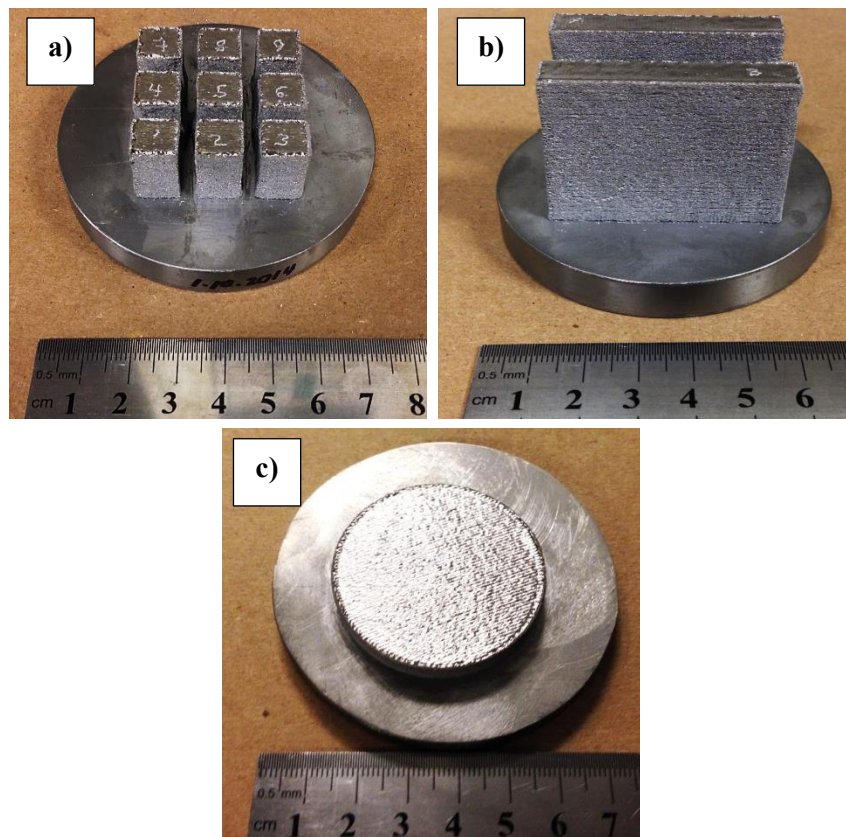


Figure 4.4 – a) Grid of 9 parts used in density experiments. b) Rectangular bars used for RRR measurements. c) Niobium discs used for thermal and electrical conductivity measurements.

For density measurements, fabricated parts consisted of grids of nine 10x10x15mm rectangular bars in which different processing parameters were investigated to increase their density (Figure 4.4 a). Rectangular bars with dimensions of 10x45x35mm were also fabricated and sent to JLab for measurements of the DC and RF properties including the residual resistivity ratio RRR (Figure 4.4 b). Similarly, two niobium discs were fabricated with diameter of ~45mm and ~10mm in height that were also used by RadiaBeam to measure the thermal conductivity (Figure 4.4 c). Density measurements of similar parts showed components had % RD values above 99.5%.

4.3.1 Application Specific Parts

Two specific designs of interest for RadiaBeam were a probe or antenna with an internal channel, and a cavity prototype with included stiffening supports. Both of these designs consisted of structures taller than ~50mm. As will be discussed later in this chapter, several complications were encountered in the fabrication of parts that exceeded this height. Nevertheless, in two particular runs it was possible to fabricate to a total height of ~90mm and two antennas could be produced. Further attempts at replicating the fabrication of niobium antennas resulted in warping of the parts and/or the failure of the build due to excess smoke or arc-trip events. Figure 4.5 shows one of the niobium antennas fabricated. These parts were sent to RadiaBeam for post-processing and machining to the required dimensions and then used at JLab in DC and RF experiments.

The fabrication of a cavity prototype was also investigated. The design of the cavity prototype was a scaled down version of a 2.3 GHz cavity which has been previously utilized by JLab in its testing facility. The original design was scaled down to half of the original CAD provided by RadiaBeam. The explored design consisted of two half cavities facing opposite to each other. At the iris where both cavities meet a band of mesh structures was embedded. The advantage of producing this prototype cavity is that it provides a seamless structure which has stiffening supports to prevent the detuning effect. Figure 4.6 shows a rendering of the CAD for

the two half cavities in blue and the supporting structures shown in green. This design was prepared in Magics RP software (Materialise, Belgium).

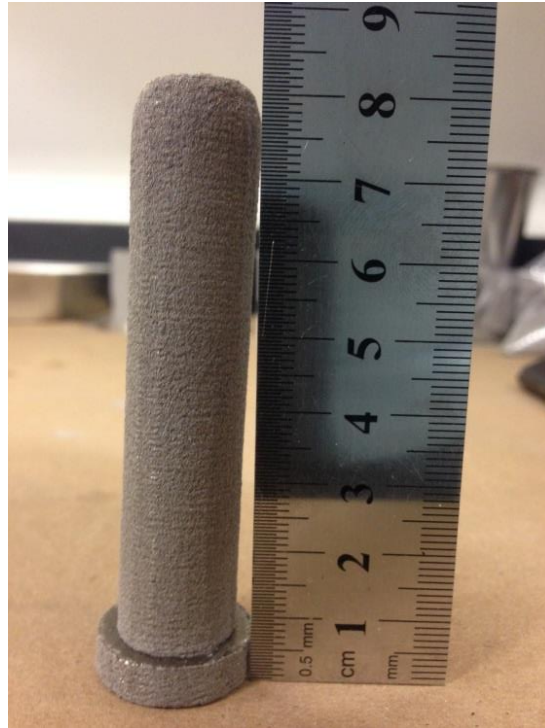


Figure 4.5 – EBM fabricated niobium antenna for RF testing.

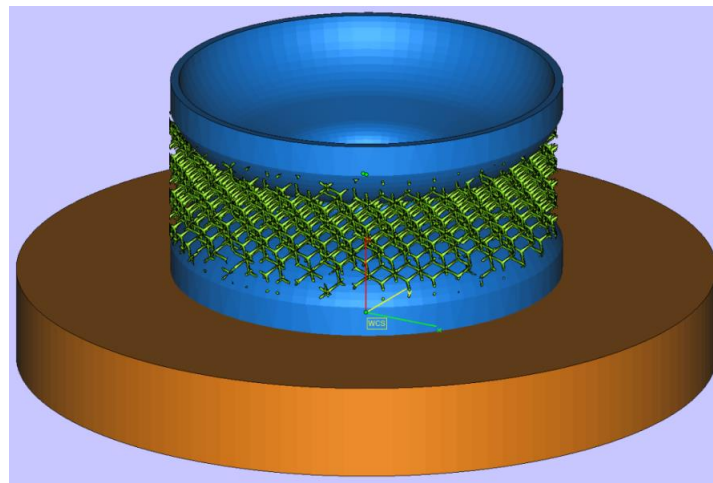


Figure 4.6 – Prototype half cavity design with supporting mesh structures.

4.4 Complications During Part Fabrication

4.4.1 Arc-trips (Powder “smoke”)

Fabrication of tall niobium parts in the EBM was not a straightforward process. Initially, the fabrication of relatively short structures (at or $\sim 15\text{mm}$) was performed without problems. Nevertheless, this was not the case when taller parts were attempted. It was observed that at a height of $\sim 35\text{mm}$ particle charging and “powder smoke” events were affecting the powder bed. These events were recorded in the EBM log file as arc-trips and, as it has been discussed before, they were very detrimental to the quality of fabricated parts. The powder smoke occurred during the preheating step of the EBM process and it was characterized by the ejection of powder in all directions outwards from the powder bed. When this happened, the high voltage in the EBM became idle for a few seconds and restarted. A possible explanation for this behavior is that the overall fabrication temperature decreased as the height of the part increased to the $\sim 35\text{mm}$ limit triggering arc-trip or smoke events during the preheat step for the powder bed. The arc-trips started a cycle that further decreased the temperature as the high voltage restarted until the build failed.

Normally, the system can and it usually recovers from the arc-trip event carrying out the preheat and melt sequences for the layer again. Nevertheless, the layer is usually not processed correctly since it can have traces of porosity because of the uneven distribution of the powder bed when the powder falls back by gravity after the arc-trip event. The effect of arc-trips is readily observed on the surface of fabricated parts. Figure 4.7 shows two similar parts processed without (left) and with (right) arc-trips.



Figure 4.7 – Fabricated antennas showing the contrast between a part with and without arc-trips or powder smoke during processing.

4.5 Causes of Arc-rips and Corrective Measures

4.5.1 Monitoring Powder Bed Temperature

With the aid of an IR camera setup (Rodriguez *et al.*, 2013), IR images of the powder bed were obtained from the beginning of one build to the point where powder smoke was observed. From analysis of the images, a relative average temperature for the powder bed was established. The average temperature was calculated from averaging the values of several regions of interest established using the ThermoCAM Researcher Pro 2.1 software (FLIR Systems Inc., USA). The screenshot taken from the Researcher Pro software (Figure 4.8) shows the different regions of interest (ROIs) in the image and the plot of the average temperatures at the interior of each region versus time. The image shows that the temperature of the different ROIs remains relatively stable throughout the monitoring time until a sudden drop caused by an arc-trip or smoke event. This suggested the gradual reduction in temperature of the powder bed was not the unique cause of powder smoke observed.

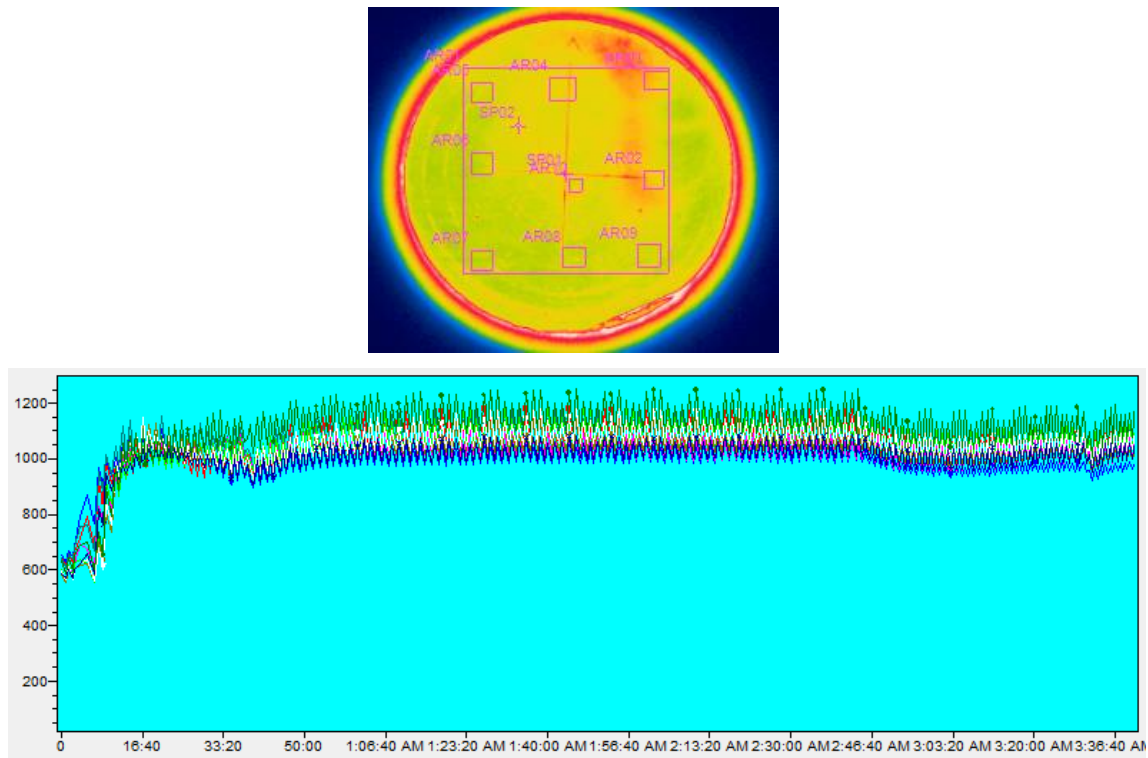


Figure 4.8 – ROIs and relative temperature values captured by the IR camera on the powder bed during niobium fabrication.

4.5.2 Changes to Preheat Theme

Another approach investigated was the variation of several parameters in the preheat step. With the premise of increasing the sintering in the powder bed, different currents of increased value were used in the preheating step. The regular current used in the preheat was 6.5mA. Increases to current values of 15 and 23.5mA were investigated as well. The rationale behind the selection of higher currents was that more energy in the preheat step would cause improved sintering of the powder bed and help in reducing the occurrence of arc-trips or smoke. SEM images were taken of sintered powder specimens at the different currents and used to characterize the degree of sintering caused in each of them. The images were qualitatively compared against the sintering observed in Ti6Al4V powder that was also processed in the EBM. The sintering in Ti6Al4V served as a reference since arc-trips seldom occur with this material during fabrication.

Images of the powder specimens processed at the different currents show no qualitative difference. Few instances of necking are observed for all three currents. Minimal difference was seen in sintered Ti-6Al-4V powder with the exception that some broken necks could be visible. This indicated that in contrast to niobium, binding of particles was stronger for Ti-6Al-4V (Figure 4.9). In the SEM images of the titanium alloy, necking can be easily seen for several particles (red arrows) while in the case of the niobium powder analyzed, only particle contacts can be observed.

Sintering was not improved using higher currents in the preheating step. Furthermore, during runs at these currents it was observed that powder smoke was still evident. For the higher current value used of 23.5mA, it was observed that after an arc-trip, the powder will not only scatter in all directions but it also turned incandescent for short times. After the experiments at higher currents were performed and did not yield improvement, further fabrication trials were carried out at the regular preheating current of 6.5mA.

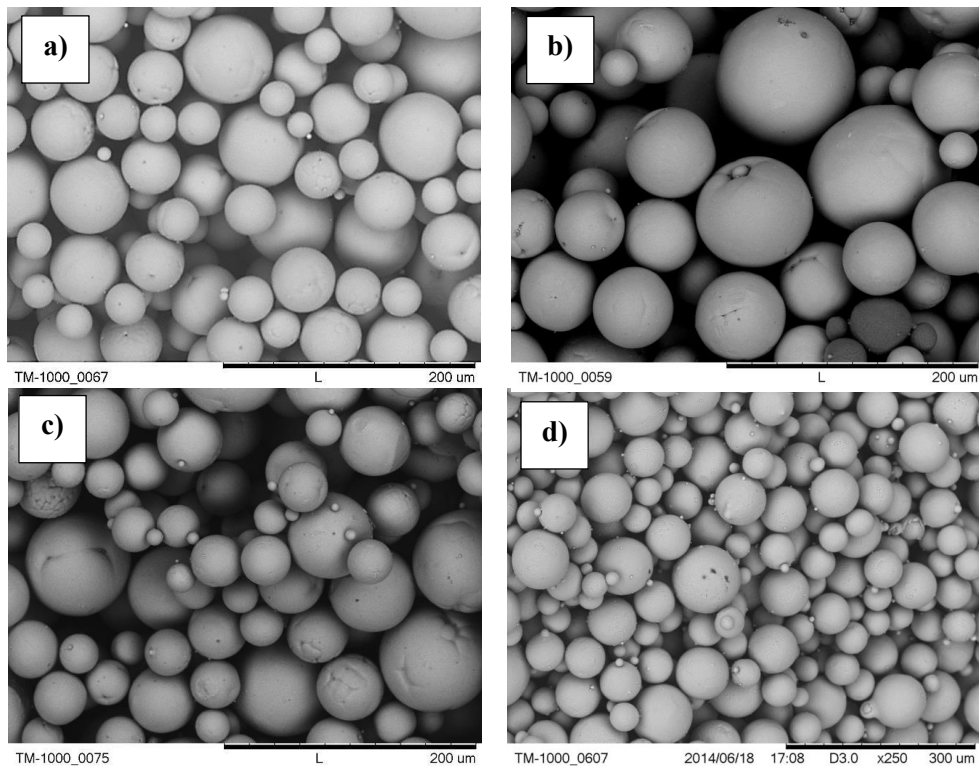


Figure 4.9 – SEM images for sintered niobium powders. Pictures a) through c) corresponding to currents of 6.5, 15 and 23.5mA, and d) Ti-6Al-4V.

4.5.3 Improved Electrical Grounding

During the machine setup, a copper wire is set into contact with the back face of the niobium build plate to provide a ground. This copper wire then passes through the mini-vat assembly and is attached directly to the floor of the A2 chamber. Poor grounding of the build plate can lead to the electrostatic charging of the surrounding particles in the powder bed that eventually can result in arc-trips (Zah *et al.*, 2008). The grounding of the niobium build plate was regularly checked during each machine setup. This was done by measuring the electrical resistance in the circuit from the build plate to the chamber. The values measured ($\sim 2.7\Omega$) were slightly above those recommended by Arcam at $< 1\Omega$.

One approach followed to see if grounding was improved with the use of copper wire that was wrapped around the niobium plate (Figure 4.10 a)). The ring formed by the copper wire around the plate was connected directly to the regular copper wire. The increased area of contact around the plate was connected directly to the regular copper wire. The increased area of contact of the build plate with the copper wire was thought to reduce the electrical resistance and prevent the buildup of electrostatic charge. A second approach consisted of the use of a copper disc which was placed between the top cover and the cylinder of the mini-vat (Figure 4.10 part b)). The copper disc was meant to provide a shorter conduction path for electrons as it was fixed at the same distance from the powder bed throughout fabrication.

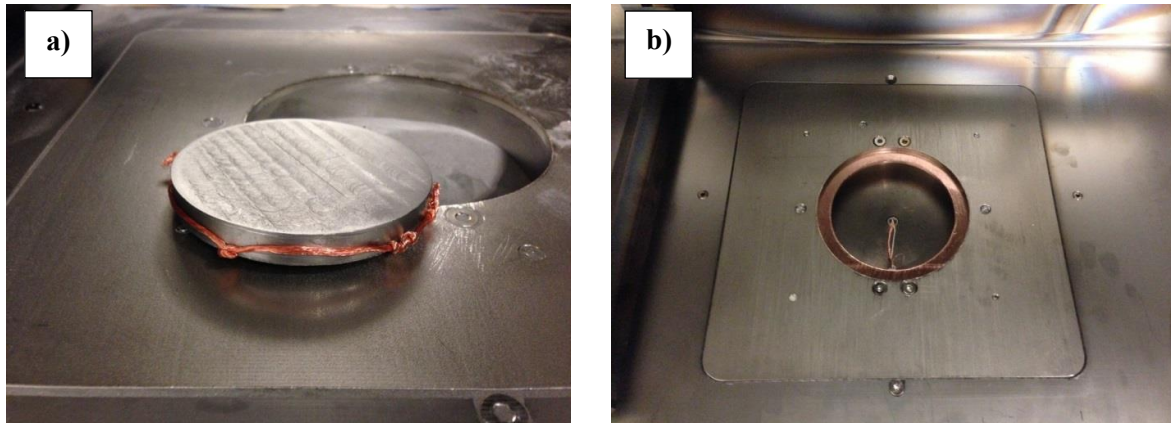


Figure 4.10 – a) Copper wire ring attached to the start plate. b) Copper disc inserted in the mini-vat assembly.

The two approaches were not effective in preventing arc-trips. Furthermore, the use of the copper disc was problematic to the distribution of an even powder bed since some of the powder collapsed underneath it. For this reason, the use of the copper disc was discarded in further runs.

4.5.4 Packing of Fabrication Bed

Another approach investigated to preventing arc-trips by using a different scanning strategy in the melt. The powder bed was packed with various parts occupying most of the area in the powder bed (Figure 4.11). This approach was somewhat beneficial for the fabrication process for reduced arc-trips were observed in several fabrication trials. Furthermore, parts with heights of ~90mm were produced using this strategy. Although more testing is needed to confirm this hypothesis, packing of the bed with various parts worked because the energy required to preheat and melt the larger surface area helped to maintain a higher temperature throughout the build time thus minimizing the occurrence of arc-trips and failure of the build.

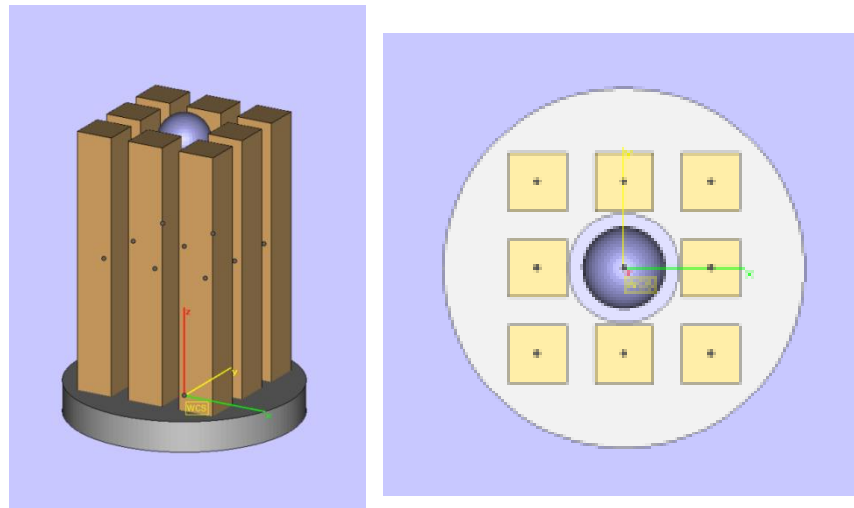


Figure 4.11 – Isometric and top view of the model used to test the effectiveness of a packed bed approach.

4.6 Part Warping and Powder Overflow

During monitoring of the powder bed with the IR camera, powder overflow was observed in the raking step. The overflow would occur because of the gradual accumulation of powder material in the opposite side to powder fetching (right side of the Arcam system). As it has been pointed out, powder fetching was only performed from the left side. No material was deposited or fetched from the right hopper. This effect is normally not seen when the regular triple raking method is used. The overflow was also detrimental to the fabrication process since the excess material moved by the rake resulted in uneven distribution of the powder bed. Variations in temperature were characterized with the help of the IR camera after the raking step. These differences in temperature of the current powder layer caused incorrect preheating of the layer and then start the development of part warping or swelling (Figure 4.12).

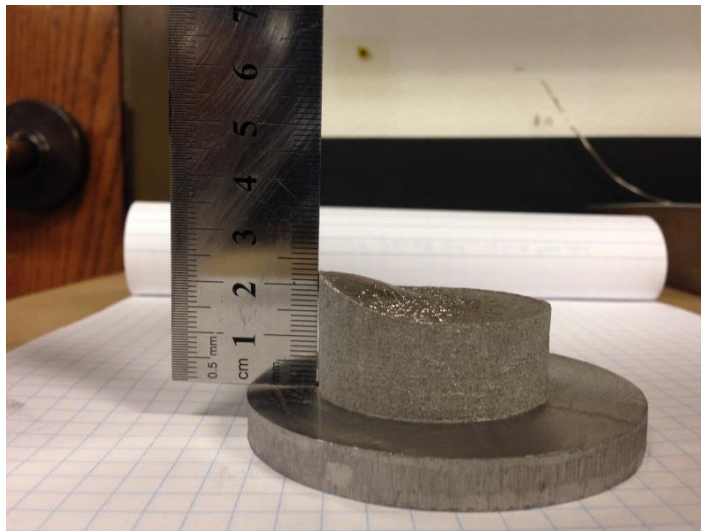


Figure 4.12 – Part warping observed in a niobium fabricated part.

The warping of the parts also contributed to arc-trips because an uneven powder bed could not be maintained after warping started. With this information, the rake positions were recalibrated preventing the overflow of material in further builds. Figure 4.13 shows IR images from the rake moving the overflow of a) and no overflow of material b) after recalibration of the

rake positions. To distinguish the overflow powder, the boundary of the rake is indicated in the left image with a red line. In image a), the rake is returning to the left side with excess powder from the overflow in the right side. In both images, the raking direction is from left to right. Powder was fed from the left side and then raked to the right side. With the single-sided raking used, the rake returned to the left position after spreading the fetched powder.

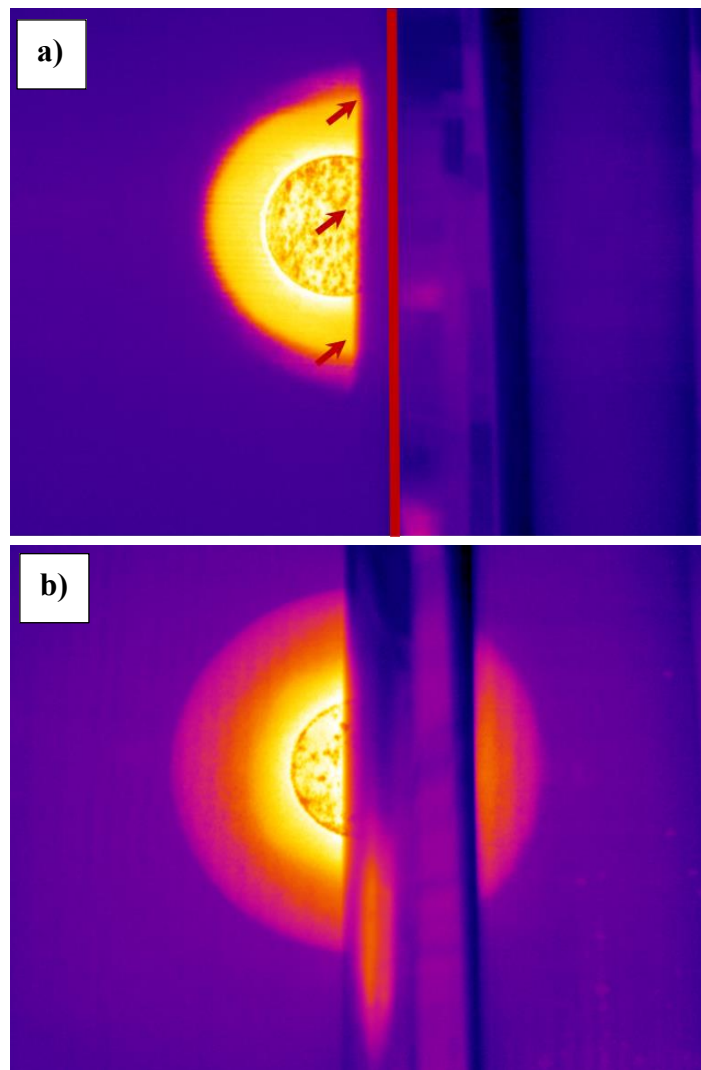


Figure 4.13 – IR images showing a) overflow and b) no-overflow raking. The arrows in the top image point to the overflowed material when the rake is returning to the left rest position.

Chapter 5: Experimental Results and Discussion

5.1 Fabrication of Niobium

The fabrication of niobium was performed utilizing the Keck Center's A2 system. Two powder batches were investigated in this work. The Phase I material referred to niobium powder that had been previously used. Phase II material was obtained directly from the powder manufacturer in sealed containers. Despite several complications during the fabrication trials, several parts could be manufactured using both powder batches that were used to conduct studies of the mechanical and physical properties of the fabricated components.

Some of the parts that were produced consisted of rectangular cross section bars that were used in the measurement of density and to study the microstructure and hardness of the EBM niobium. It is important to mention that this is the first time that tall structures $> 80\text{mm}$ have been fabricated by EBM using niobium as the powder precursor. Previous work at the Keck Center and elsewhere for fabrication of niobium in EBM only yielded small parts with heights of

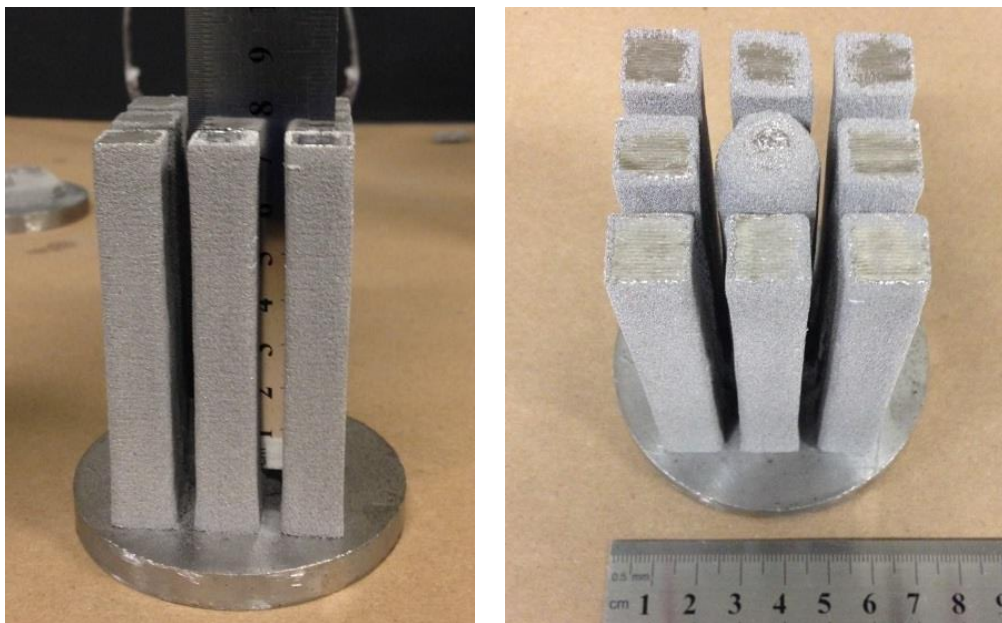


Figure 5.1 – Tallest niobium part fabricated in EBM. Parts measured ~85 mm in height

3-10mm that were used for analysis (Martinez *et al.*, 2013). With some of the structures fabricated in this study, it is demonstrated that EBM is a promising process for producing high-purity niobium tall structures for superconductor applications. Figure 5.1 shows the tallest niobium structures that could be produced during this investigation with a height of ~85mm.

5.2 Material Purity

5.2.1 Chemical Analysis

In Phase I, the chemical analysis history of niobium was traced from the wire used for atomization, in the powder and then in parts that were fabricated by EBM. Those results indicated the atomization process had caused some increase in the titanium (Ti) content as compared to the wire used for atomization (Figure 5.2). Although the increase in Ti was seen in the powder, the chemical analysis of the EBM coupon showed the chemistry of the produced part was within the standard chemical specification for this element. The limits were specified by ASTM Standard B393.

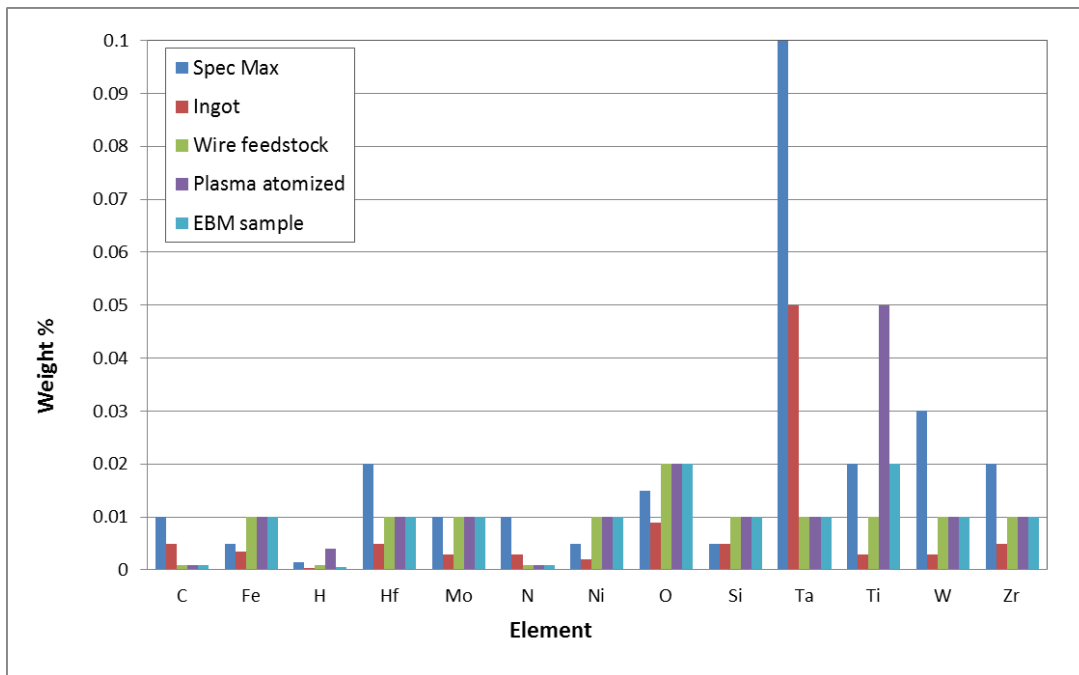


Figure 5.2 – Chemical analysis history of niobium in Phase I.

For Phase II, the results of the chemical analysis for niobium powders are summarized in Table 5.1 and the bar chart in Figure 5.3. The results are compared against the Reactor Grade 1 niobium specification (Standard, ASTM B393). The column labeled “PHI Powder (reused)” provides the chemical analysis of powder from Phase I that was used for the initial trials in Phase II. The values for column “PHII powder” correspond to powder samples from the Phase II. The Phase II samples were collected inside the glovebox with the N₂ controlled atmosphere, thus the chemical analysis was performed for this powder in the state sent by the manufacturer. At the time of this writing, analysis for the Phase II powder after reuse had not been completed. Similarly, the chemical analysis of EBM coupons fabricated with Phase II material was still underway.

Table 5.1 – Chemical Analysis results (in weight %) for niobium powders used

Element	Max Spec	PHI Powder (reused)	PHII powder
Ta	0.1000	0.0100	0.0100
Ti	0.0200	0.0400	0.0233
Zr	0.0200	0.0100	0.0100
Ni	0.0050	0.0100	0.0100
Si	0.0050	0.0150	0.0100
Fe	0.0050	0.0100	0.0100
W	0.0300	0.0100	0.0100
Mo	0.0100	0.0100	0.0100
Hf	0.0200	0.0100	0.0100
C	0.0100	0.0030	0.0023
O	0.0150	0.0385	0.0227
N	0.0100	0.0055	0.0053
H	0.0015	0.0005	0.0007

Figure 5.3 shows that the chemistry of both powder batches used for experimentation do not adhere strictly to the ASTM standard. The atomization process does not result in powder completely free of impurities since the weight percent content for some elements including Ti,

Ni, Si, and Fe were outside the limits of the specification. Nevertheless, an improvement is seen since the increase in Ti is not as marked as that from the analysis of Phase I powder.

As discussed previously, light elements such as C, H, N and O can form interstitial impurities that can become detrimental for the RF properties of superconducting cavities (Padamsee, 1998). Keeping a low content of these impurities in the powder materials was therefore required. The reported values from the chemical analysis showed that only the percent weight for O was exceeded for all powder samples studied when compared to the reactor grade material.

Previously in Phase I, chemical analysis was also performed in EBM fabricated niobium parts. This information has been detailed in RadiaBeam's Phase I report and it is included in Figure 5.2. EBM specimens with the appropriate dimensions for chemical testing have not been produced with the Phase II powder and therefore these results are not reported in this work.

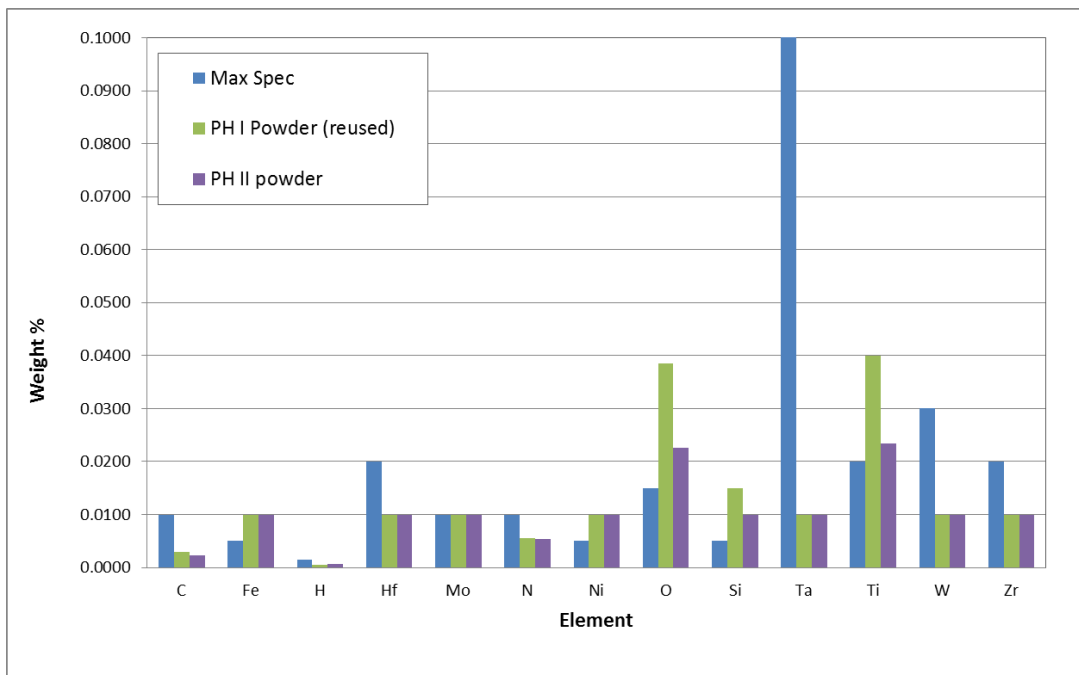


Figure 5.3 – Weight percent of elements in powder analyzed.

5.2.2 Residual Gas Analysis

The residual gas analyzer provided measurements of the partial pressures for gases in the vacuum environment of the A2 machine. This tool helped in monitoring the exposure of niobium powder to gases such as nitrogen (N_2), oxygen (O_2), hydrogen (H_2), carbon dioxide (CO_2), water (H_2O) and Helium (He) during the EBM fabrication. Leaks of these gases can occur into the EBM chamber because of their small size molecules. The plots obtained from the RGA show the values of partial pressures in Torr versus elapsed time of monitoring. RadiaBeam was interested in maintaining the pressures for all mentioned gases at below $\sim 1.0 \times 10^{-4}$ Torr. Typical RGA plots are shown in Figure 5.4. In plot a) of this figure, the partial pressure for H_2 showed the highest values (above 1.0×10^{-4} Torr) during the fabrication of the initial layers and went down over time to values in the $\sim 1.0 \times 10^{-5}$ Torr.

Some interesting behaviors were visualized using the RGA during the EBM fabrication process. First, the humps seen in the beginning of the RGA plots indicated an increase in the partial pressures for gases during the build plate preheat and outgassing sequences. At the operating temperatures of $\sim 550^\circ\text{C}$ during these stages, gases that might have adhered to the powder escaped and showed this increasing behavior. Similarly, an increasing trend in the partial pressure for N_2 (red curve in Figure 5.4 b)) was noted as the fabrication time increased. Upon discussions with the PI of the project, it was concluded that the most feasible explanation for this behavior was a small leak into the A2 chamber coming from the valve connecting to the N_2 line that was later fixed. Finally, the RGA served to identify the stages during fabrication since each peak seen in the curve for hydrogen gas corresponded to the processing of one layer. The apex in each peak occurred while the melting step was being carried out.

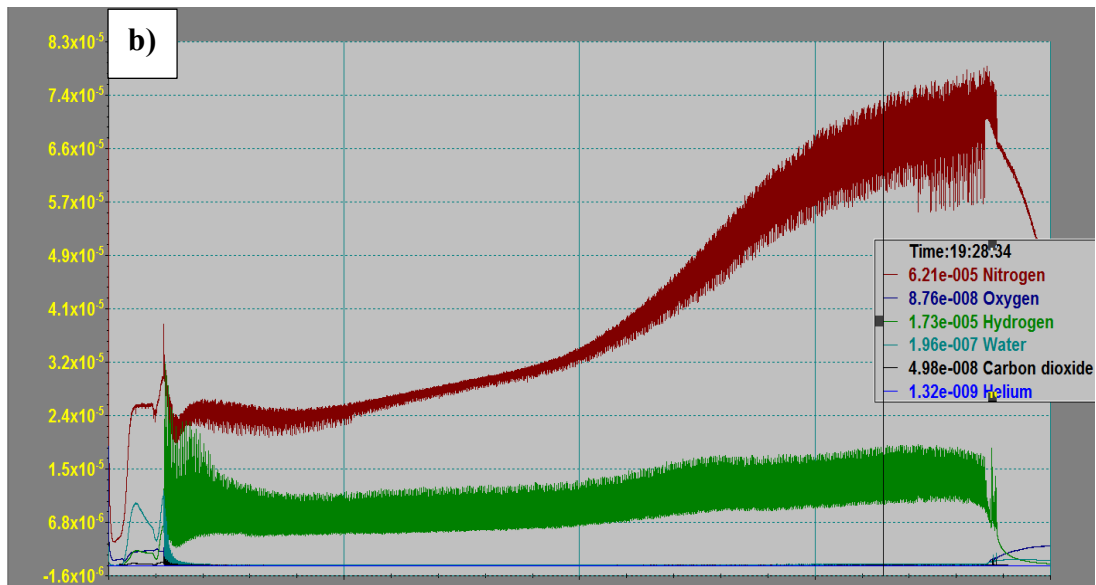
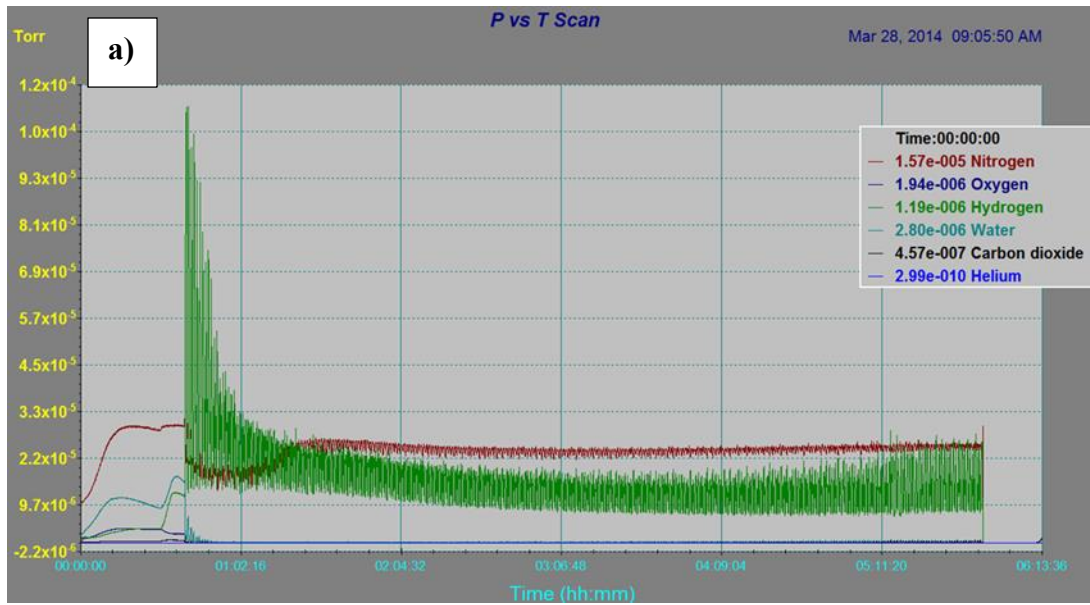


Figure 5.4 – a) Typical RGA plot observed during fabrication with niobium. b) Plot showing the increasing behavior in the partial pressure of nitrogen as the time of fabrication extended.

5.2.3 XRD Analysis

The purity of niobium was also traced from the precursor powder and after EBM fabrication using XRD. Figures 5.5 and 5.6 show the spectra for a) powder and b) the vertical cross section of an EBM block fabricated with Phase I and Phase II powder, respectively. In all XRD spectra shown, the signal was that of body centered cubic (BCC) niobium with a lattice parameter $a = 0.33\text{nm}$. The match in the position of the peaks indicated that impurities were not introduced into the niobium during the fabrication with EBM. The spectra for the vertical cross section of the EBM specimens exhibited two (Figure 5.5 b)) and four (Figure 5.6 b)) preferred orientations.

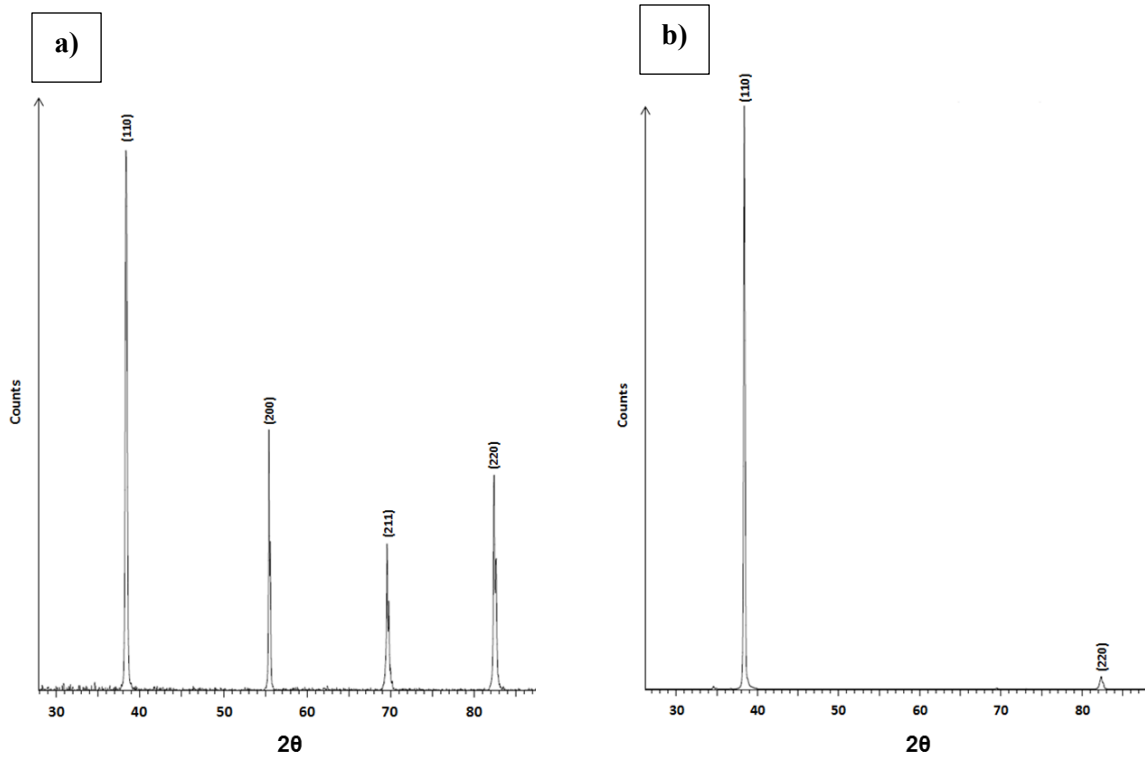


Figure 5.5 – XRD spectra for a) powder and b) EBM vertical cross section produced using Phase I powder.

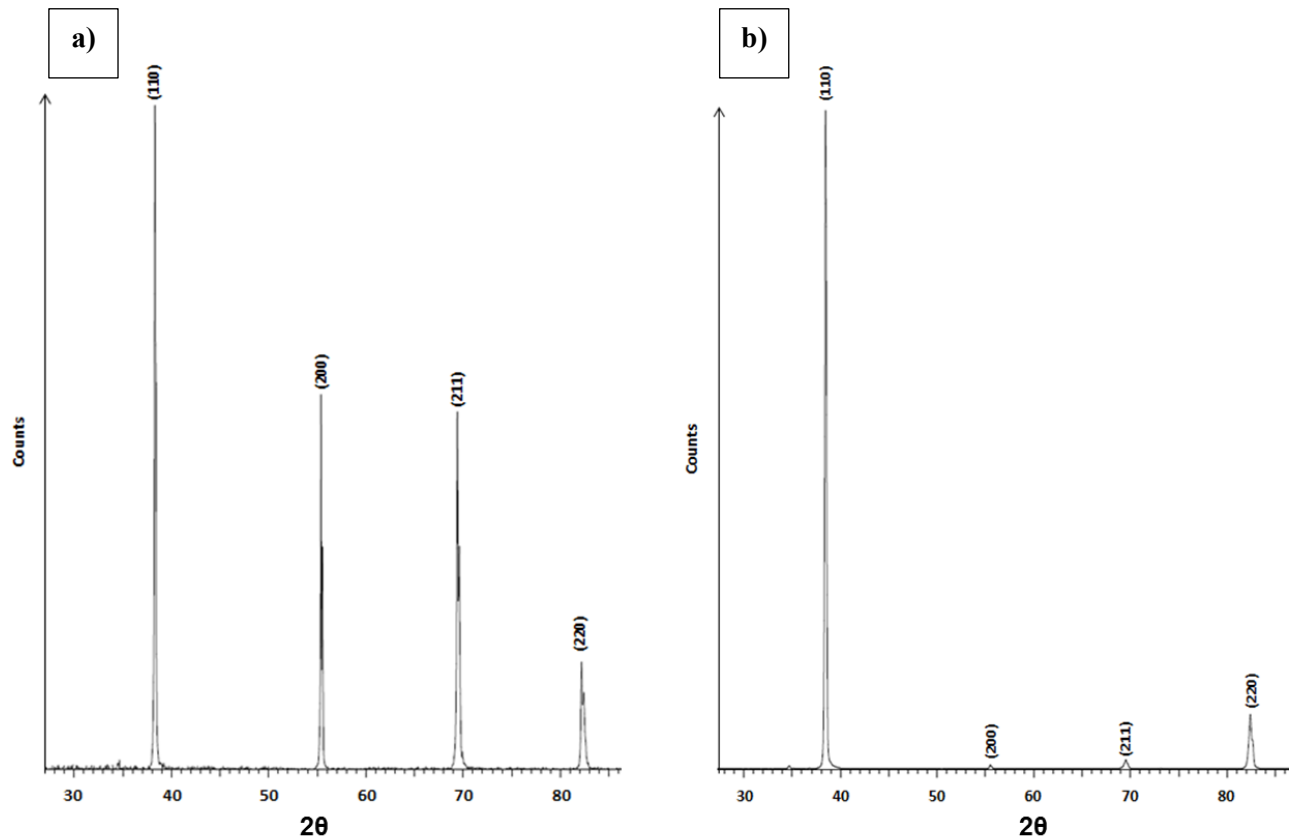


Figure 5.6 – XRD spectra for a) powder and b) EBM vertical cross section produced using Phase II powder.

5.3 Material Characterization

5.3.1 Powder

In Phase I, three powder batches with particle sizes of 25-45 μ m, 45-125 μ m and >125 μ m were mixed and used for fabrication. This mixed material was used in the initial tests carried out during Phase II. The Phase II powder consisted of powders with particle sizes only with distributions of 25-45 μ m and 45-125 μ m.

Measurements of the powder flow rate and apparent density for the niobium powders were performed after mixing the batches with different particle sizes that were provided by the powder's manufacturer. The measurements were performed following ASTM standards. Both properties provided a more clear indication of how the material would flow when processed by EBM. The apparent density and flow rate values were calculated as the average of three measurements recorded. The obtained values are listed in Tables 5.2 and 5.3 respectively. The powder from Phase I showed slightly higher average values for apparent density and flow rate in contrast to the powder from Phase II.

Table 5.2 – Calculated apparent density for niobium powders

	Powder sample	Mass cup (g)	Mass powder (g)	Volume (cm ³)	ADH (g/cm ³)	% Density change
PH I	1	137.78	268.23	30	4.35	50.74
	2	137.76	269.28	30	4.38	51.16
	3	137.75	268.5	30	4.36	50.86
	Average				4.36	50.92
PH II	1	137.75	265.47	30	4.26	49.68
	2	137.74	264.23	30	4.22	49.20
	3	137.75	265.38	30	4.25	49.64
	Average				4.24	49.51

Table 5.3 – Calculated values for powder flow rate

	Powder sample	Mass (g)	Flow rate (s/50g)
PH I	1	50.00	11.66
	2	50.01	11.67
	3	50.02	11.75
	Average		11.69
PH II	1	50.05	11.61
	2	50.00	11.42
	3	50.08	11.31
	Average		11.45

The particle morphology for the two powders used was studied. SEM images of niobium powders are shown in Figures 5.7 and 5.8 for Phase I and Phase II respectively. In both figures, the image a) corresponds to a magnification of 100x while image b) was taken at a magnification of 300x.

SEM images from both powders show different particle size distributions. The low magnification image for Phase II material (Figure 5.8 a)) shows smaller overall particle sizes in contrast to the corresponding low magnification image for Phase I powder (Figure 5.7 b)). In regards of the particle shapes, both batches of powder show similar spherical particles. The presence of small satellites and some inherent porosity can be observed in some particles as well. The porosity in the powder particles can be the cause of the increased H₂ release detected by the RGA during the melting step. As the particles were melted into solid material, the trapped gas was released from the material and detected as a sharp peak in the RGA plot, as mentioned before. Another effect observed during fabrication trials with Phase II powder, was that smoke events occurred with more frequency and at relative higher build temperatures. Following a similar analysis as that done by (Mahale, 2009), this behavior can be explained as the smaller powder particles acquired negative charge faster compared to the bigger particles seen in Phase I powder. The small particles weighed less and offered less resistance to the repulsive forces leading to more smoke events.

The particle size distributions were measured from SEM images taken at a magnification of 150x for all powders used. The constructed histograms for the particle size distributions are shown in Figure 5.9 a) and b) for Phase I and Phase II powders respectively. The histogram for Phase I powder shows an approximate normal distribution while that of Phase II appears as a shifted normal distribution. The mean particle sizes for the powders were 140 μ m and 87 μ m.

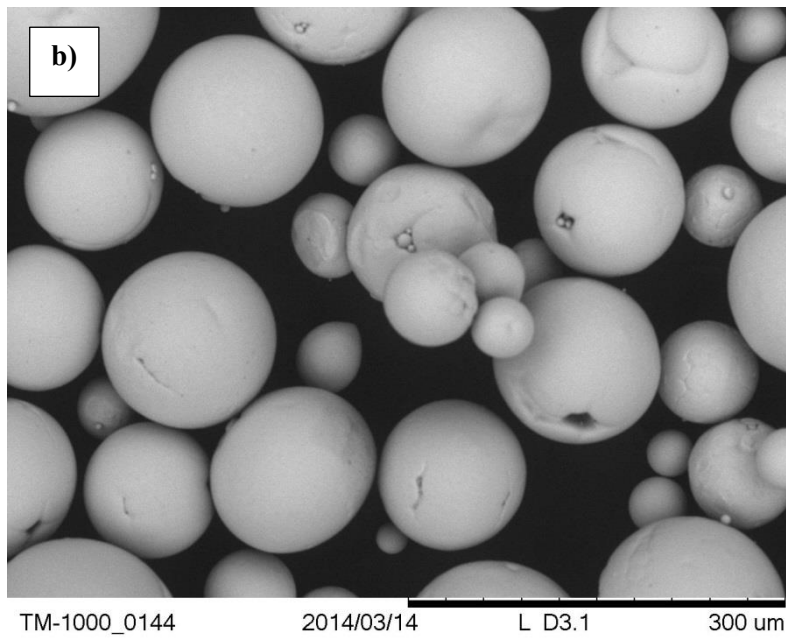
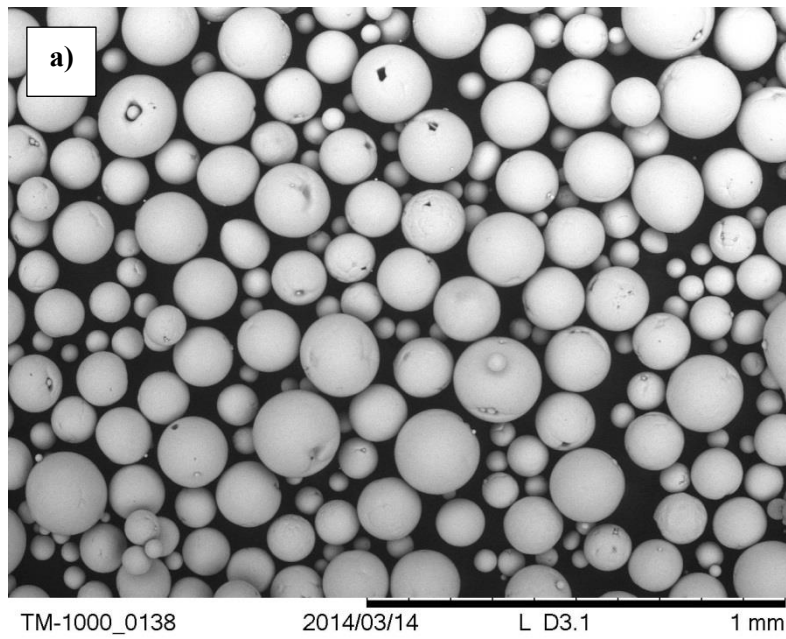


Figure 5.7 – SEM images obtained for Phase I powder at a) 100x and b) 300x.

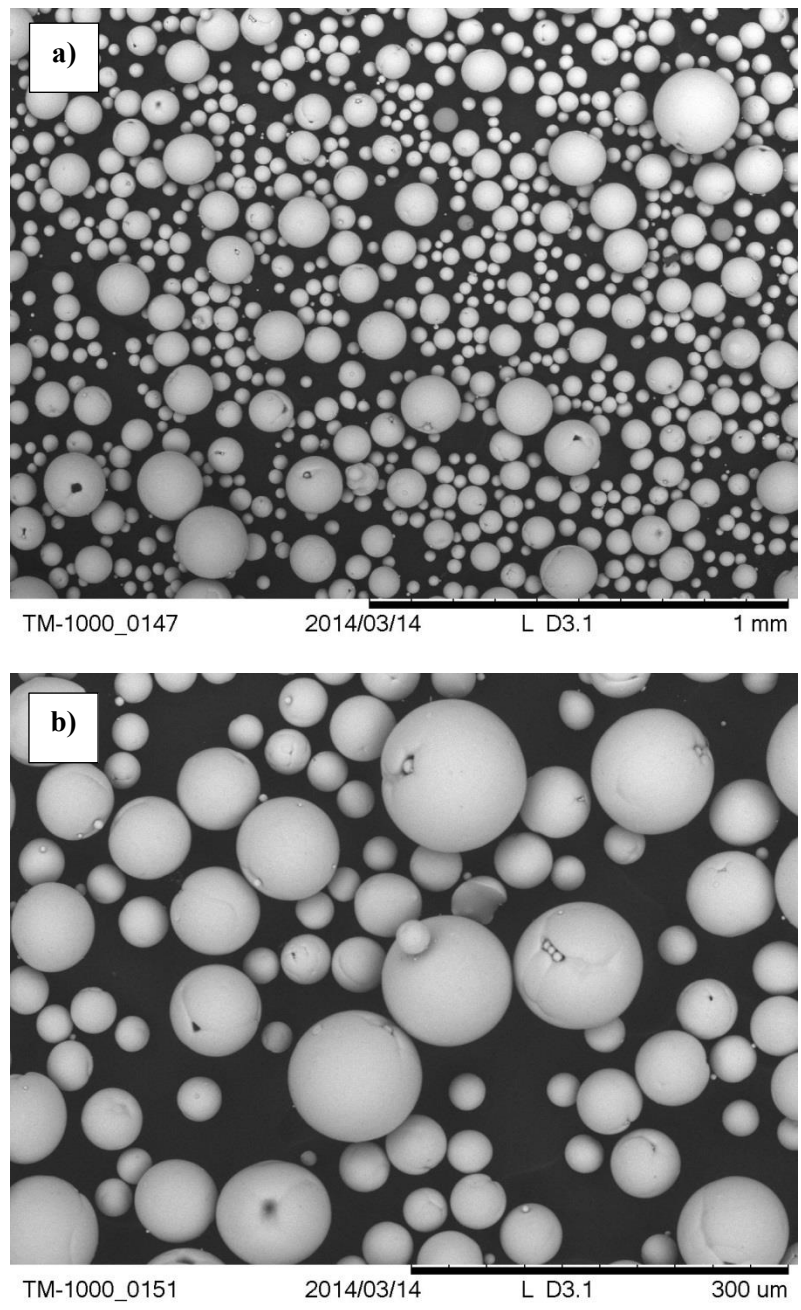


Figure 5.8 – SEM images for Phase II powder at a) 100x and b) 300x.

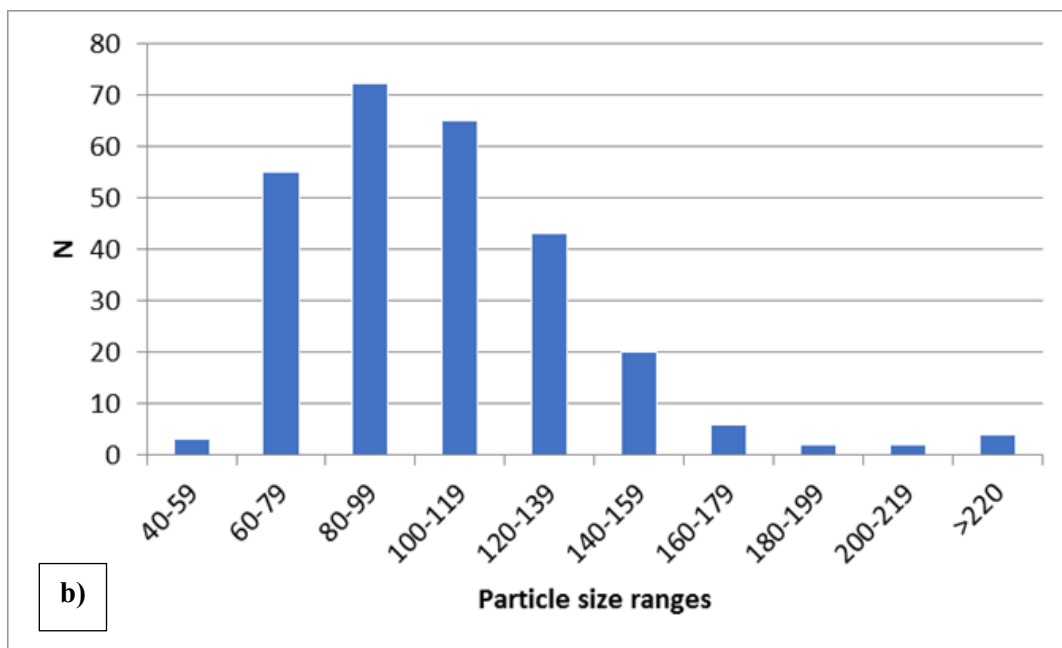
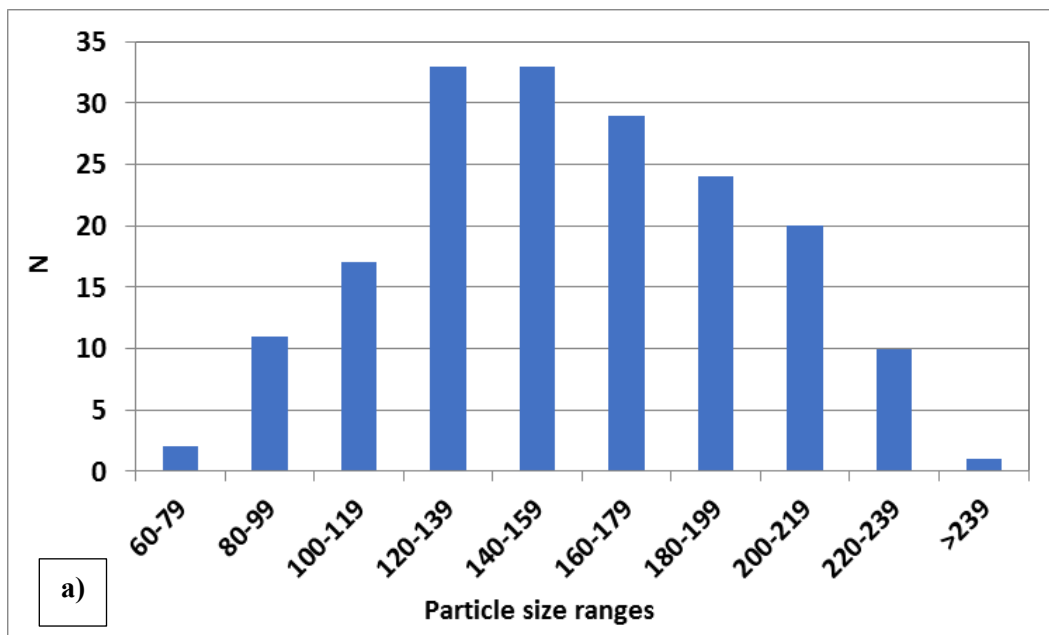


Figure 5.9 – Particle size histograms for Phase I a) and Phase II b) powders.

5.3.2 Microstructure of EBM Niobium

Light microscopy images taken from EBM niobium parts are shown in Figures 5.10 and 5.11 for the vertical and horizontal planes of reference. Parts a) and b) in both figures correspond to parts fabricated with Phase I and II powders respectively. The microstructure observed in the horizontal plane shows grains that are somehow equiaxed but also some grains of irregular shapes. The grain size for the microstructures analyzed estimated by the AGI method averaged $\sim 250\mu\text{m}$. Previously, (Martinez *et al.*, 2013) reported equiaxed grains with $\sim 200\mu\text{m}$ in size for the horizontal plane of EBM fabricated niobium parts.

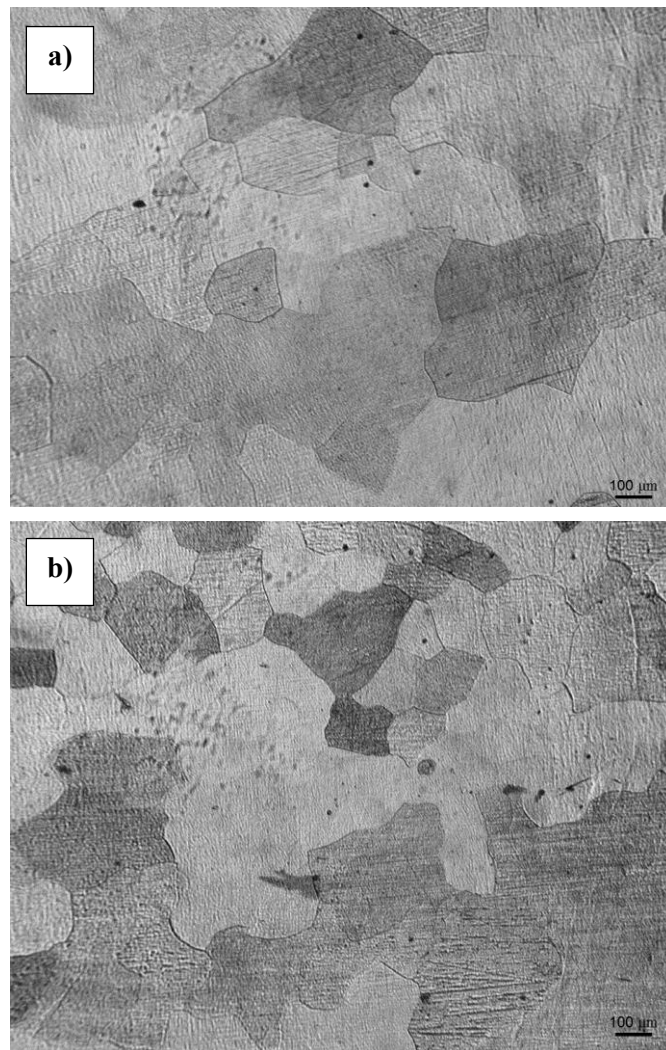


Figure 5.10 – Grain microstructure observed for EBM fabricated parts with a) Phase I and b) Phase II powder in the horizontal plane of reference.

The microstructure in the vertical reference plane shows the characteristic columnar grains which elongate parallel to the build direction of the EBM process. It is interesting to note that some of these grains span multiple layers. In the microscopy images shown in Figure 5.11, the lengths of some grains cover the entire height of the figure corresponding to approximately 20 layers. Although the boundaries are well defined and constant for most columnar grains, others appear to vary and merge with contiguous grains. Still, such grains grew several layers.

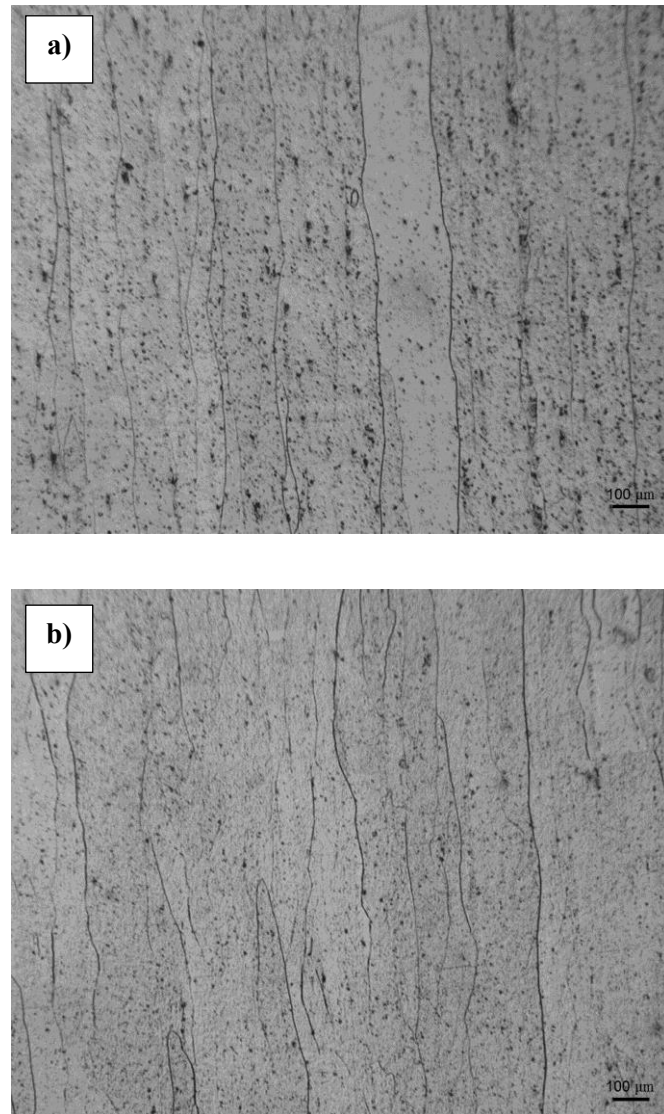


Figure 5.11 – Columnar grains observed in vertical plane of reference of EBM parts fabricated with a) Phase I and b) Phase II powder.

For comparison, the microstructure of wrought reactor grade niobium (WRG) is shown in Figure 5.12. The grain morphology observed corresponds to equiaxed grains in all directions of the material.

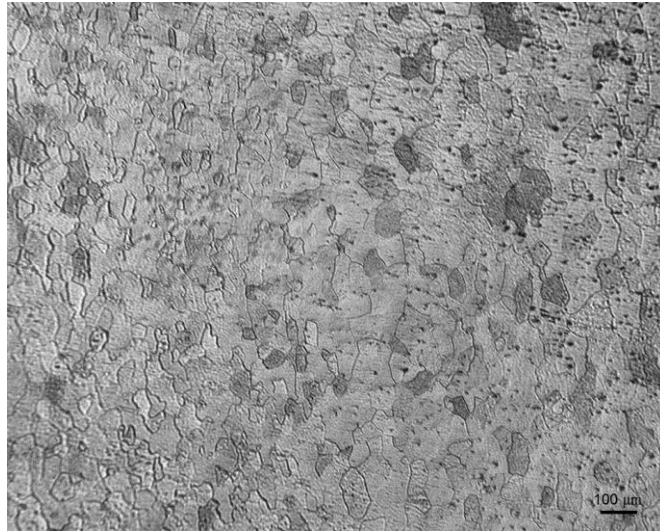


Figure 5.12 – Microstructure of wrought reactor grade niobium showing equiaxed morphology of grains.

5.4 Mechanical Properties

5.4.1 Yield and Ultimate Tensile Strengths

Tensile testing was performed for the first time for EBM-fabricated niobium and compared to results from testing of specimens machined from reactor grade niobium. Four specimens were machined from EBM bars that were built in the z-direction using the powder from Phase I. Five specimens were also fabricated and tested for WRG niobium obtained from RadiaBeam. Table 5.4 shows the compiled results for yield, UTS, percent elongation, and approximate percent area reduction of the EBM and the WRG specimens tested.

The stress-strain curves for EBM specimens are shown in Figure 5.13. Average values were calculated for yield strength at the 0.2% offset and for the UTS which resulted in ~140MPa and ~225MPa respectively.

The stress-strain curves for specimens fabricated using the equiaxed WRG niobium are shown in Figure 5.14. The average 0.2% yield and UTS for this material were calculated at ~135MPa and ~205MPa respectively.

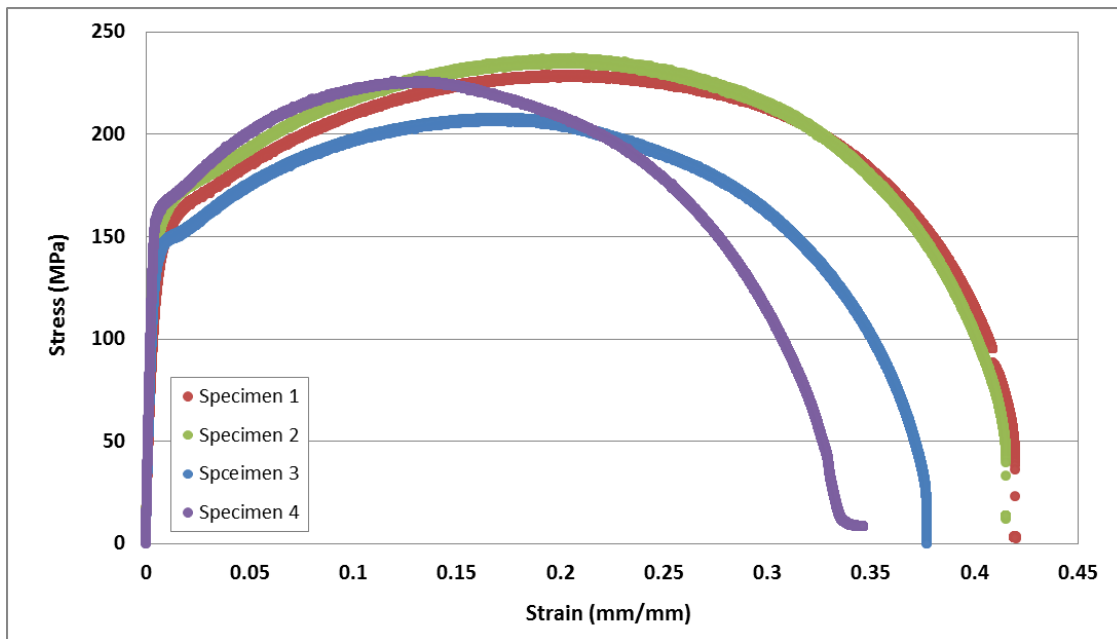


Figure 5.13 – Stress-strain curve for EBM niobium specimens.

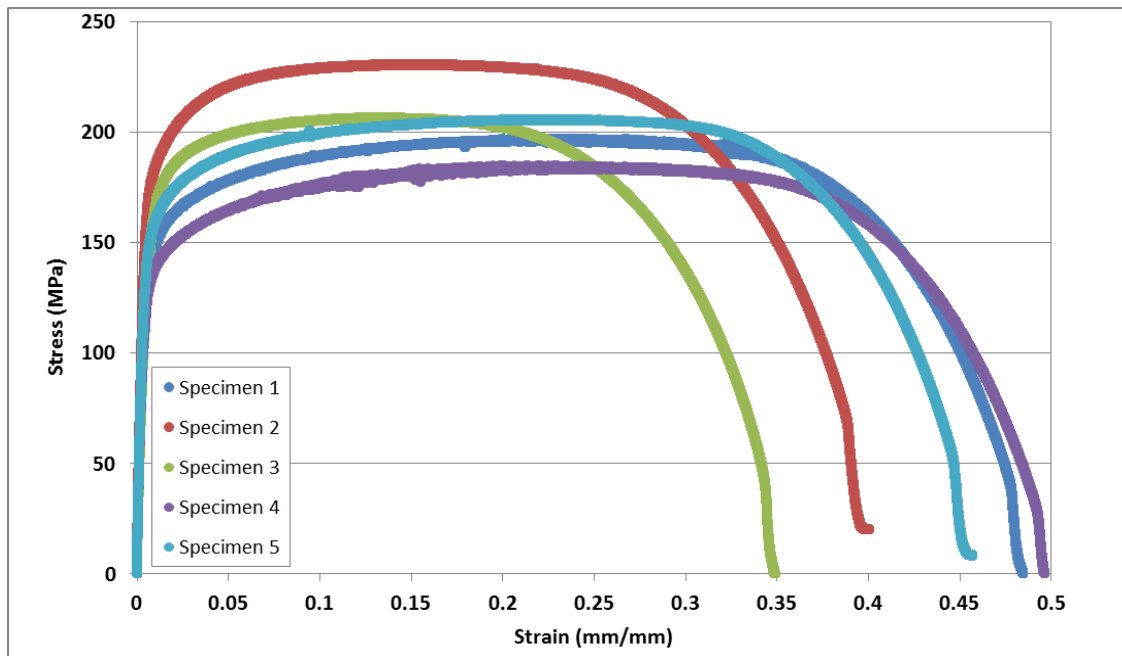


Figure 5.14 – Stress-strain curves for reactor grade niobium.

Reference is made to Appendix B for the plots showing the linear region (0.04 maximum strain) of the stress–strain curve of each tensile test that aided in obtaining the 0.2% offset yield strength values. Calculated R^2 coefficient, from the linear regression fit are also shown in each plot.

From the stress-strain curves for both materials it can be stated that the WRG niobium specimens exhibited a more plastic behavior since the material elongated for more time (flat region in the curves) as the material reached the UTS. By contrast, the curves for EBM specimens followed a steady descent right after the UTS was reached. This corresponds with the higher elongation observed for the WRG niobium as explained in the following section.

5.4.2 Percent Elongation

As it has been stated before, an extensometer was not used for measuring the axial displacement or elongation of specimens during the tensile test. The values for the percent elongation were approximated by recording video during testing of each specimen and the initial and final frames analyzed to calculate the differences in distance between two gage or punch marks. The use of manual measurements has been described as a suitable method to evaluate elongation from tensile tests (Davis, 2004). This approach has been used in elongation measurements for niobium and titanium materials for SRF applications (Walsh *et al.*, 1999).

In each tested specimen, the distance between gage marks, before and after loading, was measured in units of pixels (px) by analyzing each image in Matlab. Figure 5.15 shows the initial and final frames of the video recorded for one test specimen with the measured distances between the gage marks for each image. The average percent elongation for EBM niobium specimens was calculated as 34%. For the reactor grade niobium, the percent elongation was 45%. Manual measurement of elongation has been associated to a couple of percent above values obtained from digital devices (Davis, 2004).

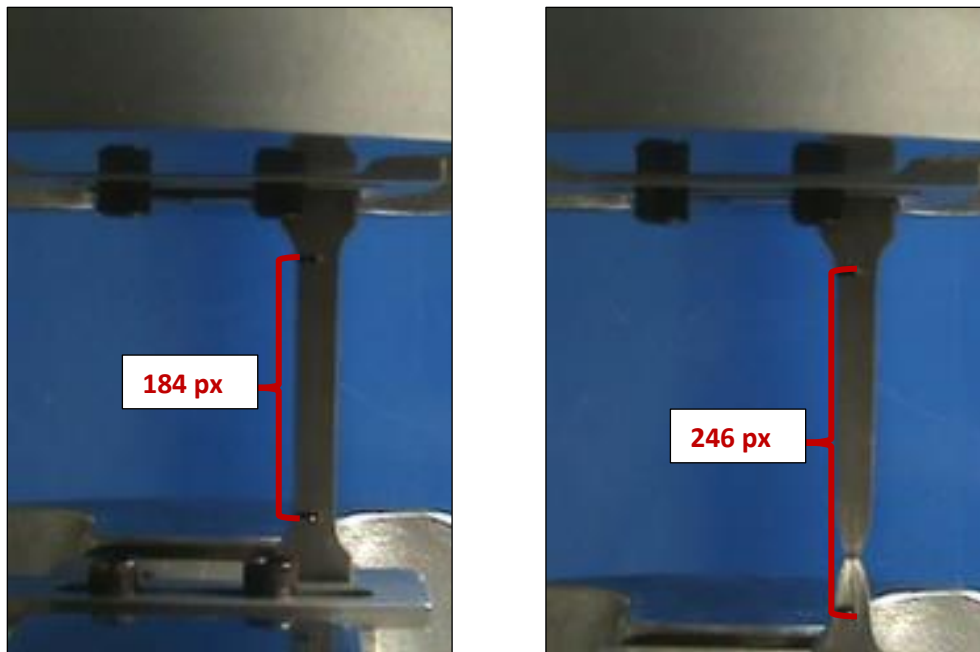


Figure 5.15 – Measured distance in pixels to evaluate elongation of tensile specimens.

5.4.3 Percent Area Reduction

Figure 5.16 shows the results obtained by the Matlab boundary detection code with one original fed image and the detected boundary. As described in the methodology section, the detected area in pixels was multiplied times the area of a single pixel in mm^2 to calculate and approximate the area reduction in the correct units. Measurements for the original areas of specimens and after fracture are included in Table 5.4. The calculated average percent reduction in areas was very close for both EBM and the reactor grade niobium with $\sim 98\%$ and $\sim 97\%$ respectively. The obtained measurements might be within ~ 0.5 to less than 1% error as it was obtained for the boundary detection code and explained in the methodology section.

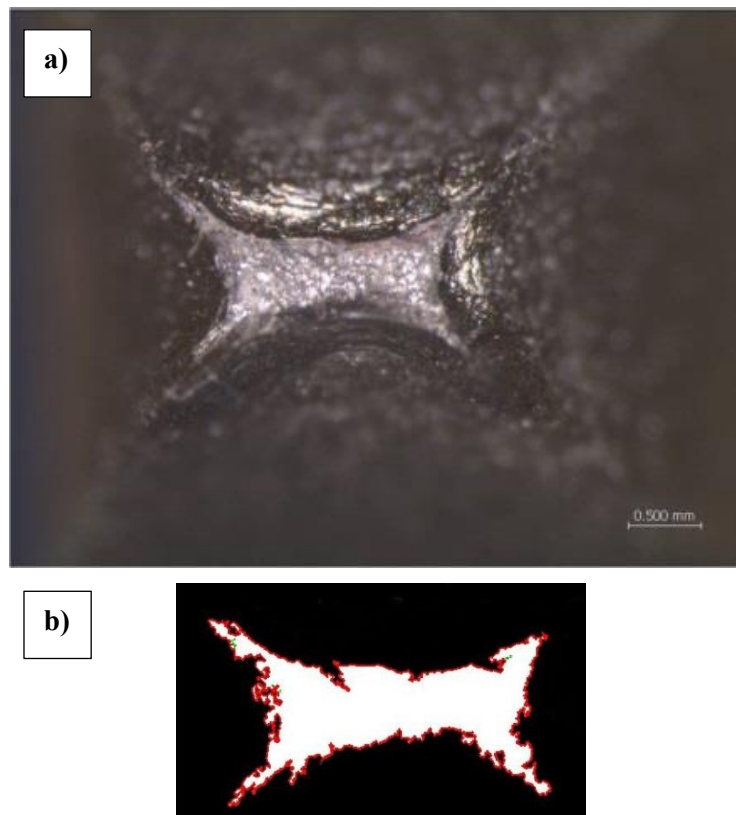


Figure 5.16 – a) Stereomicroscope image fed into the boundary detection code and b) the detected area in pixels.

Table 5.4 – Results from the tension test of EBM and WRG niobium materials.

Specimen	UTS (MPa)	Yield (0.2%) (MPa)	% Elongation	A ₀ (mm ²)	A _f (mm ²)	% Area reduction
EBM1	229	125	37	32.61	0.37	98.9
EBM2	237	145	33	32.89	0.56	98.3
EBM3	208	136	34	32.79	0.67	98.0
EBM4	226	159	33	32.72	0.67	98.0
AVERAGE	225	141	34.25	32.75	0.57	98.27
WRG1	197	121	51	32.01	0.75	97.7
WRG2	231	163	46	31.96	1.01	96.8
WRG3	207	132	34	32.5	1.02	96.9
WRG4	185	121	51	32.6	0.73	97.8
WRG5	206	137	44	33.3	0.97	97.1
AVERAGE	205	135	45.2	32.47	0.90	97.24

Comparable results from tensile tests for EBM high purity niobium are not available in literature. A comparison can be made to tensile testing of specimens extracted from niobium stock sheets having uniform equiaxed grains with sizes from 29-59 μ m and with RRR values in the range from 30 to 492 have shown varying results for tensile properties. Compton found average yield strength of 185MPa and UTS of 322MPa for niobium with RRR=30, and lower average values of 74MPa and 200MPa for niobium with RRR=492. The author also reported percent elongation of 63% and 51% for the two grades of niobium (Compton, 2000). In a similar study, yield strength, UTS and elongation ranges for niobium with RRR>250 were 43-86MPa, 169-187MPa and 56-67% respectively (Jiang *et al.*, 2007).

The large percent reduction in area obtained for the specimens tested in this work indicates high ductility for both EBM and WRG niobium. It is interesting to note that while the percent elongation was higher for the WRG niobium, the EBM niobium exhibited 1% higher reduction in area. The values for the yield strength were comparable for both materials with only a few MPa (6MPa) difference. In the case of the UTS, the EBM niobium specimens exhibited higher values overall. This was attributed to the different microstructure of the studied materials since the columnar grains present parallel to the fabrication direction of EBM niobium provided more resistance to deformation during the tensile testing as compared to the uniform equiaxed morphology shown by the WRG niobium.

Analysis of fracture surfaces for tensile specimens was also performed using the SEM. Figure 5.17 shows SEM images at 50x magnification for the top section of tested specimens for a) EBM and b) WRG niobium looking down directly in the vertical direction. The WRG specimen exhibited the type of deformation commonly described for rectangular specimens with an aspect ratio that still resembled a rectangle while the fracture surface of EBM specimens showed more of a square shape.

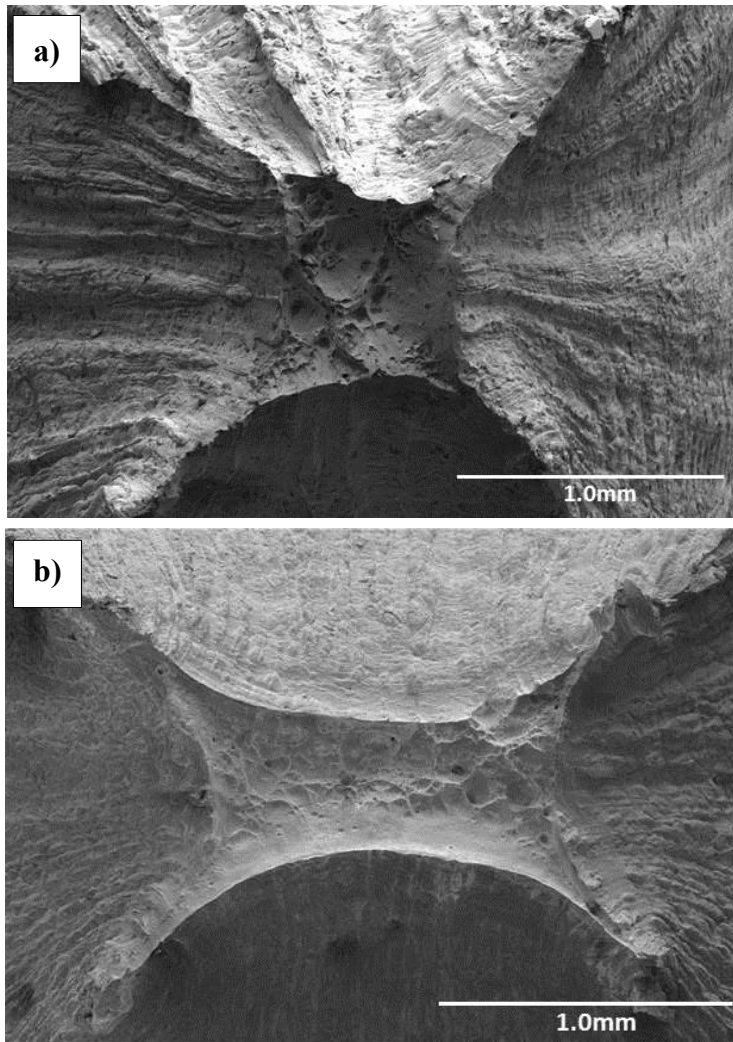


Figure 5.17 – SEM images at 50x magnification showing fracture surfaces of a) EBM and b) WRG niobium tensile specimens.

Figure 5.18 shows SEM images at 150x for the same fractured specimens shown in the previous figure; a) is for EBM and b) for the WRG niobium respectively. At this magnification, sites of possible porosity were identified (indicated by red arrows in the images) which might have contributed to early failure of some tested specimens such as EBM number 4 and WRG number 3. More porosity sites could be observed in WRG niobium specimens.

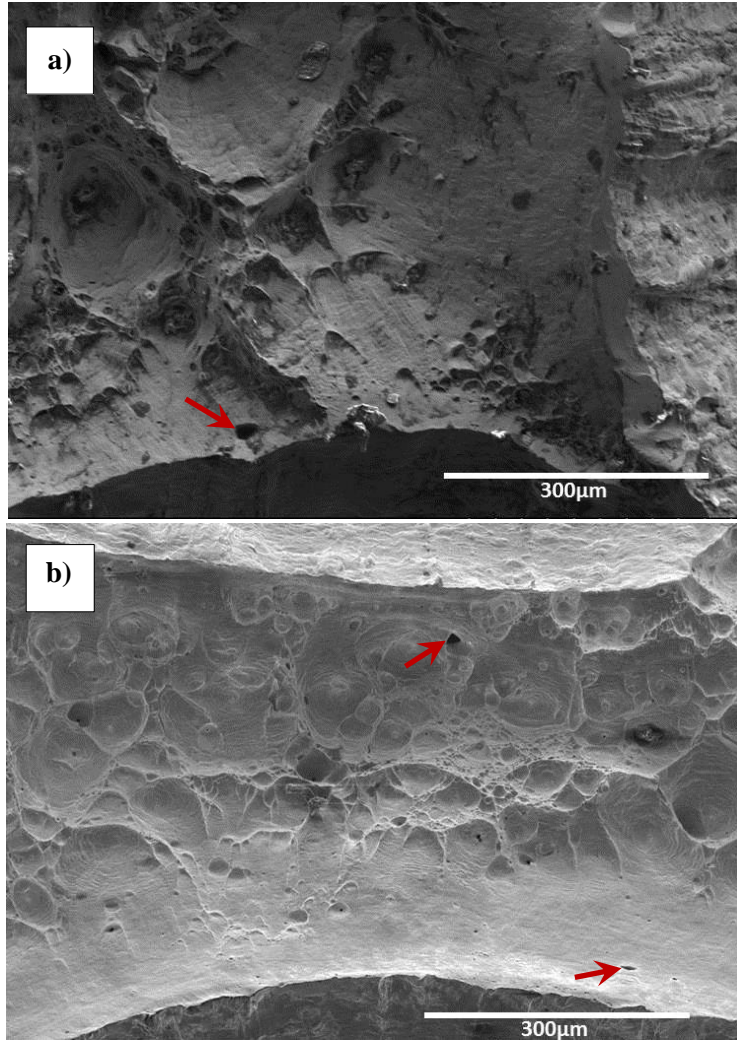


Figure 5.18 – 150x SEM pictures showing identified sites of possible porosity in the material pointed by red arrows.

The ductility of both EBM and WRG niobium materials investigated in this work was implied from the values of percent elongation and percent area reduction measured in tensile specimens. Although the ductile features were not as prominent as in materials with similar percent elongation as Inconel 625 (Xu *et al.*, 2013), the SEM images looking at the fracture surface reveal the presence of dimples and micro-void coalescence (Figure 5.19).

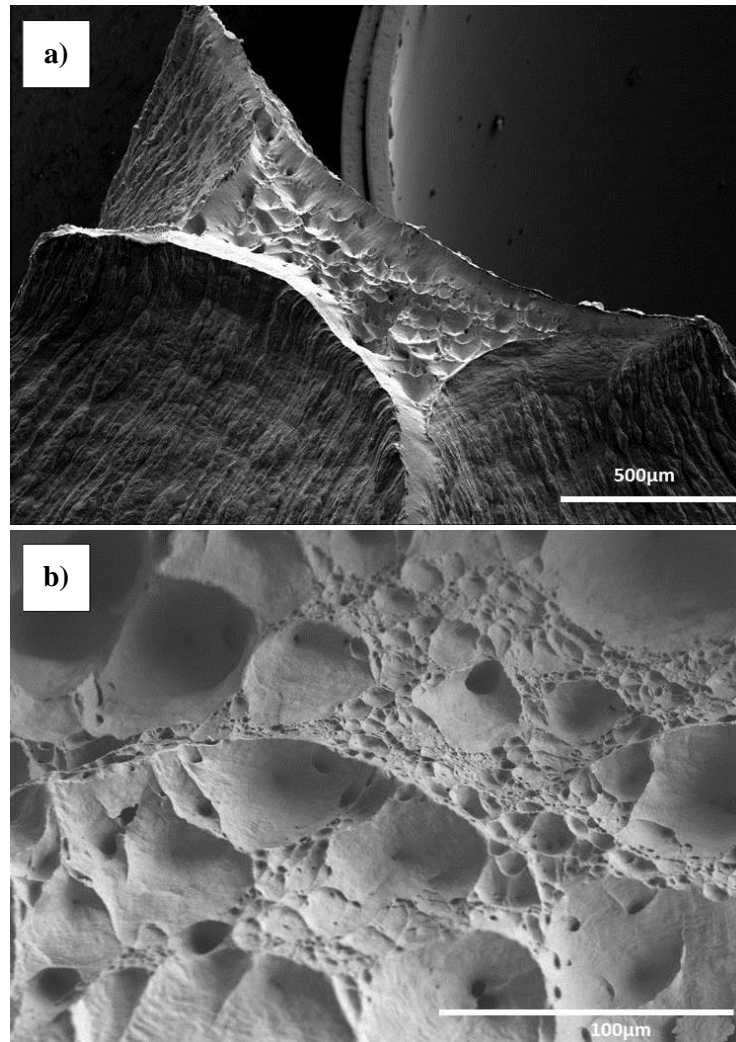


Figure 5.19 – a) SEM image at 60x showing fractured surface of specimen at 45 degrees. b) SEM image at 500x for a WRG specimen showing the micro-void coalescence and dimple formation.

In part a) of the figure, a 60x magnification of the fracture surface oriented at ~ 45 degrees can be seen. The image shows big dimples that pinpoint to the fracture initiation sites. Part b) shows an SEM image with a higher magnification of 500x normal to the fracture surface for a WRG specimen where dimples and micro-voids are better seen. A possible explanation for the difference in the fractures surfaces shown by Xu *et al.* for Inconel 625 compared to niobium is that rectangular specimens were used in the work presented in this dissertation. The use of

cylindrical tension specimens might depict similar ductile fracture features, which is the reason they are recommended for future work in Chapter 6.

5.4.4 Hardness

For EBM niobium, in the horizontal plane, average hardness values converted to the Vickers scale were 0.79GPa (69 HRF) and 0.74GPa (63 HRF) for Phase I and Phase II respectively. For the vertical plane of reference, the average values were higher at 0.82GPa (73 HRF) and 0.81GPa (72 HRF). For WRG niobium, the hardness measured in all three directions averaged 0.79 GPa (69 HRF). Similar findings for the hardness of EBM niobium were described in RadiaBeam's Phase I report ranging from 0.82 to 0.86 GPa. Micro-indentation hardness values in the range from 0.92 to 1.1 GPa were reported in the study by (Martinez *et al.*, 2013).

Figure 5.20 shows measured values of hardness as a function of height for EBM parts ~50mm tall that were produced using both Phase I and Phase II powders. For Phase II, measured values appeared stable at ~70HRF. In the case of the hardness of parts produced with Phase I powder, most measurements recorded were at ~80HRF. Interestingly, at ~40mm, a sudden drop in hardness was observed for these measurements of the Phase I bars.

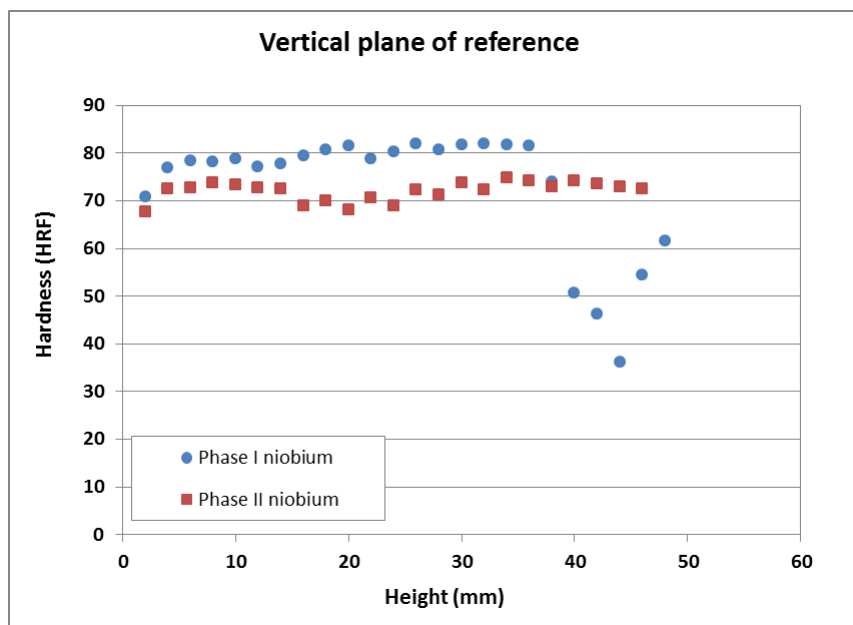


Figure 5.20 – Hardness measurements in the vertical plane for EBM niobium parts.

The explanation for this behavior was the presence of delamination and incomplete melting of powder that developed in the measured parts following an arc-trip or smoke event at that particular height. Figure 5.21 shows the photographs of the cross-sectioned bars used for taking the hardness measurements. Part a) for the Phase I bar showed the delamination occurring near the top of the part (red arrow). In part b), corresponding to the Phase II bar, no delamination or porosity was observed throughout the entire height.

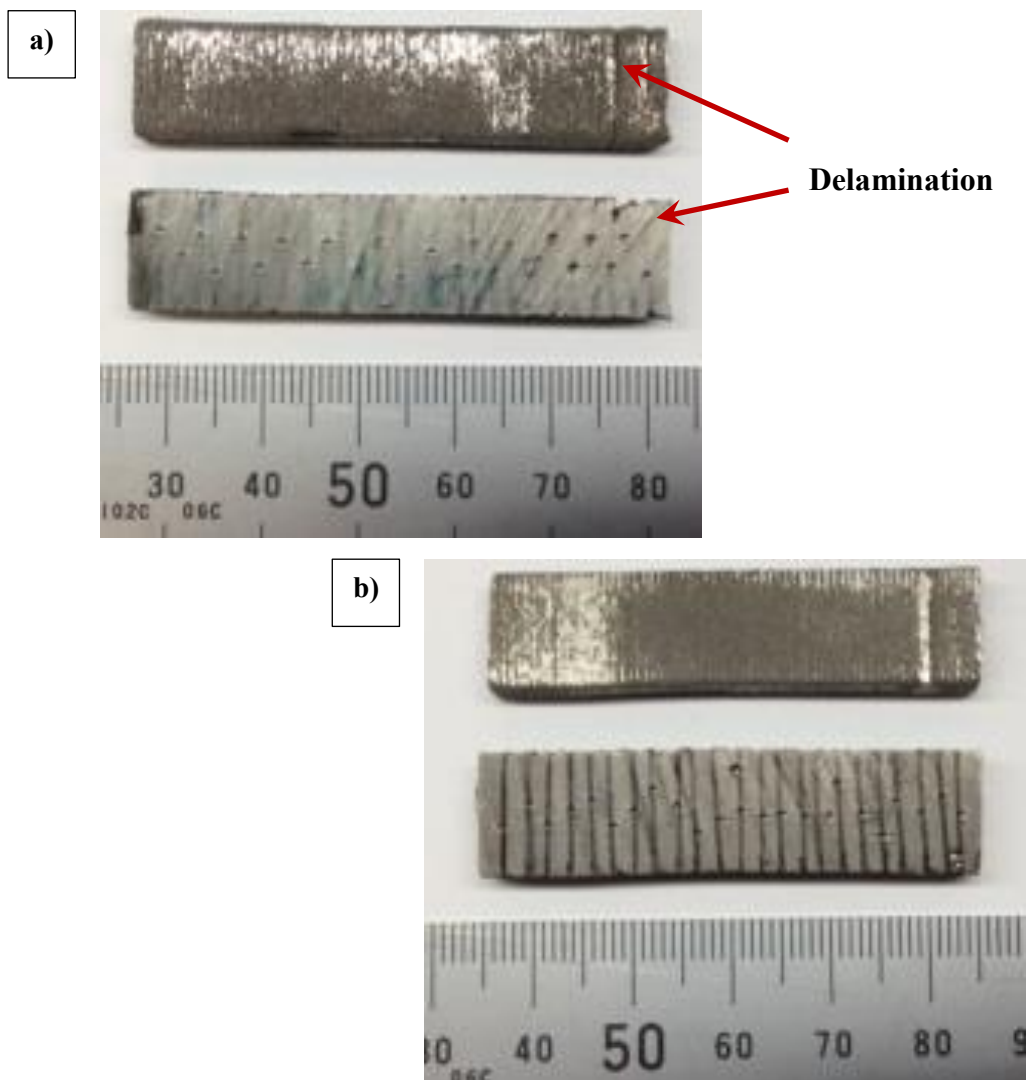


Figure 5.21 – a) Bar produced with Phase I powder showing the delamination that might have caused reduced hardness. b) Shows the bar from Phase II powder with no defects.

5.5 Physical Properties

5.5.1 Apparent Density

As described in the methodology, the density of the parts was improved using several iterative experiments. In each experiment, a grid of nine parts with different parameters was explored. As described before, dense parts improve the SRF properties of niobium. The percent relative density was calculated and compared against reactor grade material with a density of 8.57g/cm^3 . The set of figures from 5.22 to 5.24 show bar graphs of the values obtained for the measured apparent density and the percent relative density for the nine parts fabricated in each experimental trial. Appendix D provides a compilation of the parameter grid used in each experiment.

In Experiment # 1 (Figure 5.22), all parts had apparent densities below 8.5g/cm^3 (%RD<99%). The average apparent density was 8.08g/cm^3 (94.2% RD). The densest part in this set was # 1 with an apparent density of 8.48g/cm^3 (98.9% RD) and its fabrication parameters used as base point for the second experiment.

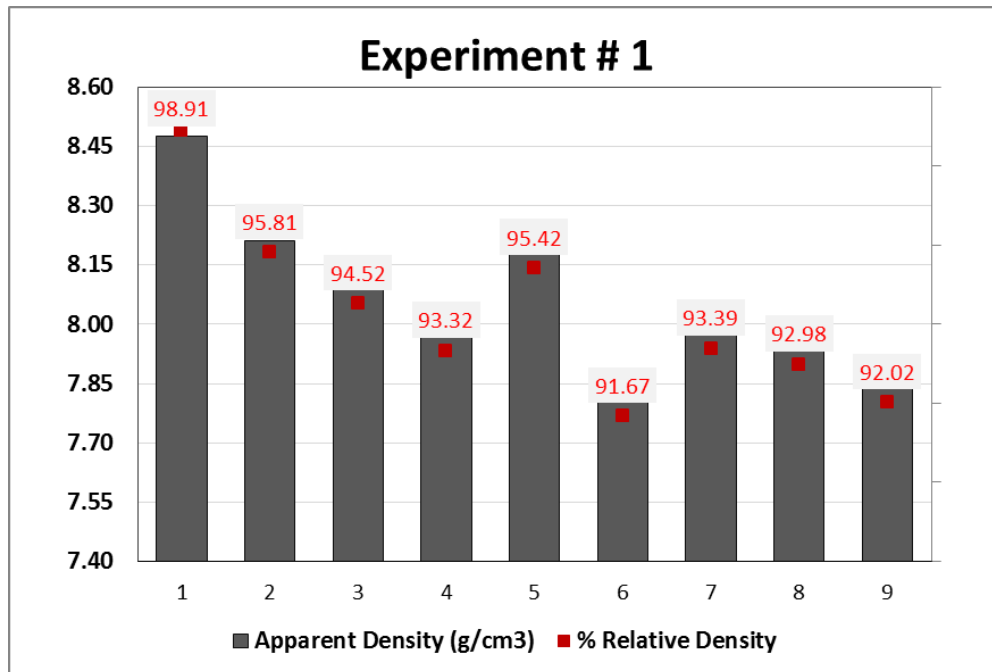


Figure 5.22 – Apparent density and %RD values obtained in Experiment # 1.

Figure 5.23 provides the results for the density values obtained in Experiment # 2. An improvement in the density for several parts was observed. The average apparent density for the parts in this experiment was 8.43g/cm³ (98.5% RD). The highest density values were observed for parts in the middle row of the (parts 4, 5 and 6) with measured apparent density values at or above 8.50g/cm³ and %RD over 99%. From this set, part # 5 was the densest at 8.53g/cm³ (99.5 %RD).

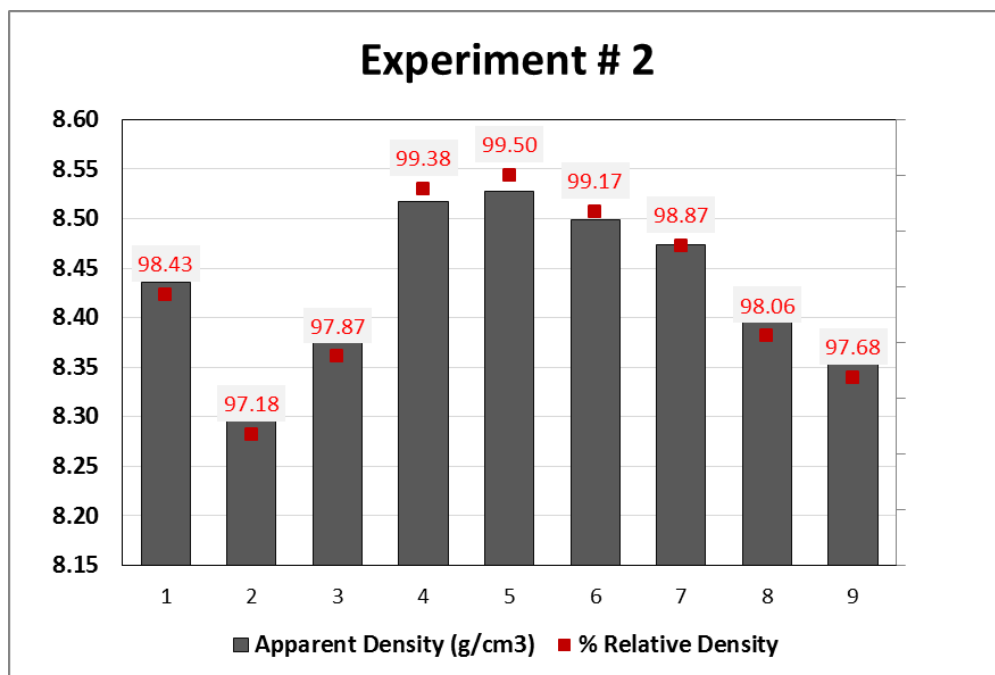


Figure 5.23 - Apparent density and %RD values obtained in Experiment # 2.

The measured values for density of Experiment # 3 are shown in the bar graph in Figure 5.24. As explained with more detail in Appendix D, the focus offset for all parts fabricated in Experiment # 3 was set at 31mA, and only variations in beam speed and current were explored. The resulting average apparent density was 8.45g/cm³ (98.6% RD). The maximum density was measured for part # 7 with 8.55g/cm³ (99.7% RD). The fabrication parameters for part # 7 were used in subsequent builds as they provided the highest density for parts.

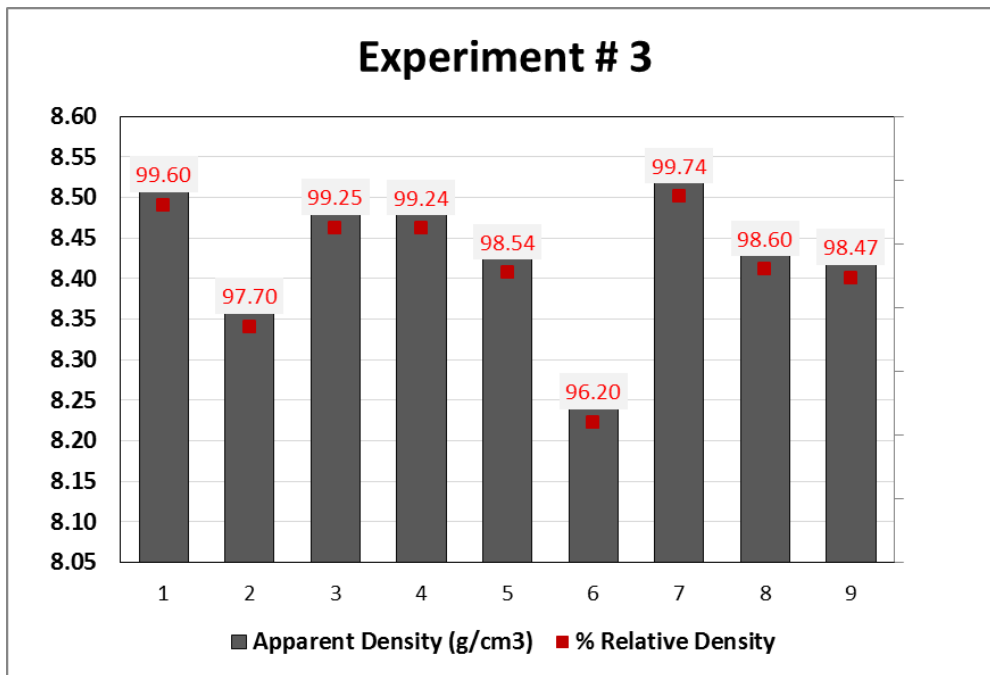


Figure 5.24 – Apparent density and %RD values obtained in Experiment # 3.

With the experimentally determined “best” fabrication parameters a build consisting of eight square bars measuring 12x12mm per side and a part specific consisting of a probe or antenna for RRR measurements were fabricated. One square bar was machined to remove the contours from the part and cut into five sections. Measurements were done of the density of these parts and the resulting values are shown in Figure 5.25.

The average apparent density for the five piece set was 8.55g/cm³ (99.8% RD). Although smaller values were measured in the bottom and top sections, the results indicated the produced material to be nearly fully dense after the machining operation to remove the contours. As it has been mentioned before, this is important since the more dense the material, the better the properties for SRF applications.

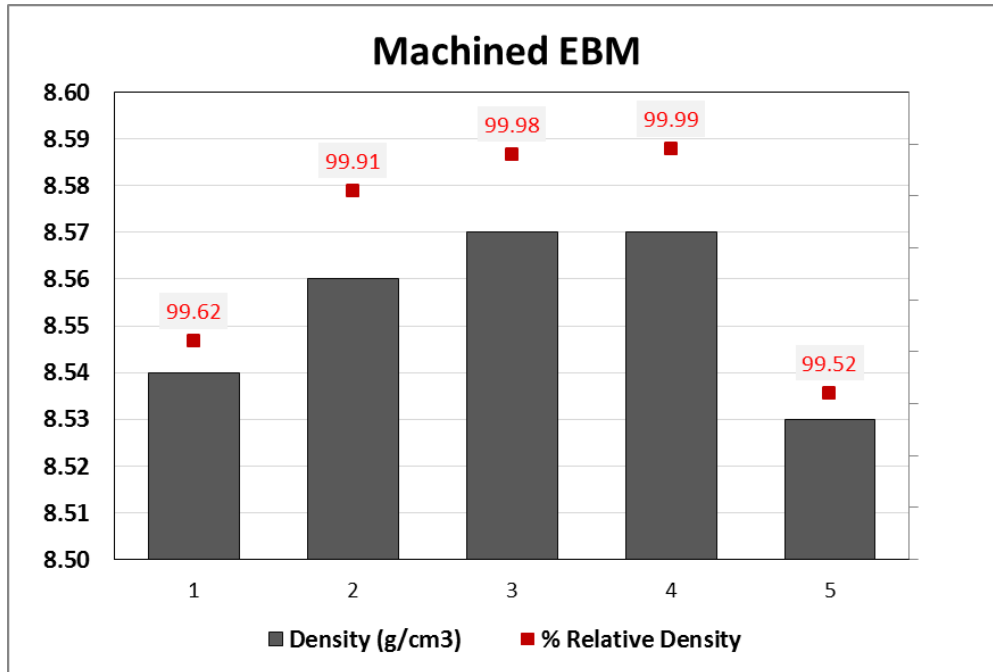


Figure 5.25 – Measured values of apparent density and %RD for five sections extracted from an EBM bar fabricated with optimized parameters.

5.5.2 Thermal Conductivity

As stated before, the best solution to prevent the quenching or thermal breakdown of the accelerating while experiments are running is by having niobium with a high thermal conductivity. The high thermal conductivity allows the defects in the niobium surface to tolerate more power dissipation before breaking the field.

The thermal conductivity for EBM niobium was measured by ThermTest Inc. using the TPS method. The averaged measured thermal conductivity was 49.7 W/m K. This value was within those normally found in high purity or reactor grade niobium with a nominal thermal conductivity in the range of 50-54.1 W/m-K (Matweb.com). Results from all measurements of the two niobium discs tested are shown in Table 5.5.

Table 5.5 – Thermal conductivity measurements reported by ThermTest Inc.

Sample	Thermal conductivity (W/m K)
Disc 1	49.91
	50.05
	50.59
	49.86
	49.74
	50.14
AVERAGE	50.05
Disc 2	48.95
	50.03
	49.40
	49.45
	50.11
	49.57
AVERAGE	49.16
	49.52

5.5.3 Residual Resistivity Ratio

Two blocks having dimensions of 10x50x35mm were sectioned at JLab for initial RRR measurements. All these parts were fabricated with Phase I powder. Results provided from JLab for the measurements of RRR indicated a value in the range of ~10-20. For comparison, components tested in Phase I had RRR of 19-24.7 as reported by RadiaBeam. Measurements of the RRR ratio for the Phase II powder have not been performed at this time as testing continues to fabricate suitable parts. Because of the implemented extra steps to maintain a cleaner environment for fabrication with the Phase II powder, higher RRR might be expected when results become available.

5.5.4 DC and RF Testing

Fabrication of two EBM niobium probes with dimensions of ~85mm was achieved. These pieces were provided to JLab for testing. At the time of this writing, only preliminary results had been made available through informal communications indicating the accelerating field obtained with one of the EBM probes used at a frequency of 3.585GHz was limited by heating. This indicates the EBM niobium still contains superficial defects after machining that lead to thermal breakdown. According to RadiaBeam, testing was inconclusive using the setup with the 85mm antenna and the recommendation was to work in the fabrication of a regular size probe measuring 120mm in height to proceed with RF testing at JLab. Testing will continue at JLab using the EBM niobium probes with the proper height.

Chapter 6: Conclusions and Recommendations

6.1 Conclusions

High purity niobium parts were fabricated using an Arcam A2 EBM system. The main components of the fabrication chamber were replaced and the system thoroughly cleaned prior to introducing the niobium powder to prevent its contamination. The powder material was also handled by implementing a protocol which included the use of a glovebox with a controlled nitrogen gas (N₂) atmosphere. With this system, powder exposure to environmental humidity or other sources of impurities was prevented. The purity of the niobium material was traced at several stages in its production route from the wire feedstock fabrication, plasma atomization and finally in parts fabricated with the EBM system. Several techniques were employed to characterize the purity of the material that included chemical analysis of powder samples and x-ray diffraction of both powder and solid EBM components. The RGA tool also helped to diagnose the quality of the vacuum inside the Arcam A2 chamber that was required to prevent contamination of the EBM-fabricated parts by the presence of gas species such as oxygen, carbon dioxide, helium, water vapor and nitrogen.

Due to the limited amount of niobium powder, a mini-vat configuration was employed to assist in the fabrication. This system, developed at the W.M. Keck Center for 3D Innovation, was helpful in the fabrication trials but limited the height of the parts that could be obtained to just below 90mm. The fabrication of niobium was performed using a delay theme that allowed the cool-down of the powder bed prior to the deposition of a fresh layer of powder. This was done to prevent powder agglomeration which was observed if raking of powder was carried out immediately after the melting step. With this setup, the fabrication of several parts was possible and the tallest EBM niobium structures, with maximum heights of ~85mm, fabricated for the first time.

An iterative experiment approach was used to improve the density of the EBM-fabricated niobium resulting in densification of the parts with average apparent density of 8.55g/cm³. This

value was comparable to the density for wrought reactor grade niobium of 8.57g/cm^3 . The improved density of EBM parts constituted and advance in the percent relative density (%RD) of the material from 98.6% in previous trials to 99.8% for parts produced in this work. The density of parts was measured using the water displacement method following ASTM standard B311-13.

Also, for the first time, characterization of the mechanical properties of the EBM niobium was performed. Tensile specimens with the dimensions from ASTM standard E8/8M were fabricated and the yield and ultimate tensile strengths obtained. A visual method was employed to measure the percent elongation and a computer code with edge and boundary recognition utilized in calculating the percent reduction in area for the tensile specimens. The average values obtained were 140MPa, 225MPa, 34%, and 98% for the yield strength, UTS, percent elongation and percent reduction in area, respectively. For comparison purposes, specimens of the same dimensions were also fabricated for wrought reactor grade niobium provided by JLab and average values for the mechanical properties were 135MPa, 205MPa, 45% and 97% in the same order as before. The hardness of EBM niobium was also measured for the horizontal and vertical planes of reference, average values were measured at $\sim 0.8\text{GPa}$ for both planes of reference.

Specific application parts were also fabricated in this study. These included niobium discs of $\sim 35\text{mm}$ in diameter and $\sim 8\text{mm}$ in height, and the fabrication of one probe with an internal cooling channel. The niobium discs were used to characterize the thermal conductivity of the material by the TPS method and the average value measured at $\sim 50\text{W/m-K}$ (comparable to that of reactor grade niobium). In the case of the fabricated probe or antenna, this part was machined by RadiaBeam and sent to JLab for measurement of the SRF properties of the material. Results are not conclusive at the time of this writing as testing continues at JLab. The residual resistivity ratio (RRR) was measured for EBM-fabricated niobium parts at JLab with values anywhere from 10 to 20.

The microstructures of the EBM niobium were characterized using optical microscopy. This analysis revealed grains had an average grain size of $\sim 250\mu\text{m}$ in the vertical plane of reference. In the vertical plane, columnar grains were observed that spanned for a length of at least 20 layers (1.4mm). The width of the columnar grains in microns was approximately the size of the grains observed in the horizontal plane.

During the fabrication trials, powder smoke was the principal cause of failed builds and/or defects in parts. Although several approaches were investigated to prevent this effect, the multiple factors that can affect the fabrication including different powder sizes, the variation in the thickness of the start plate, uneven distribution of the powder by the single sided raking strategy used can be traced as causes of errors. Similarly, issues with the grounding were prevalent in most experiments.

6.2 Recommendations

The EBM fabrication of niobium was a challenging process because the material tends to warp if processing temperatures are too high and it will tend to produce powder “smoke” during the preheat step if powder temperatures are too cold. Among the recommendations that can be extracted from this work are the following:

- Fabrication with bigger size start plates to see if this corrects the incidence of powder “smoking” by increasing the preheating area. The larger area will also allow fabrication of other parts that were not accomplished in this work such as the SRF cavity because of the limitations imposed by the mini-vat.
- The tensile testing performed in this work was carried out in less than ideal conditions mainly because of the reduce size specimens that could be machined out of fabricated parts. Thus, it is recommended that round specimens are fabricated that will permit more accuracy in the measurements for the reduction in area. Furthermore, the use of a suitable extensometer is recommended to obtain

more accurate values of elongation and that can later be contrasted with the measurements in this study.

- The cyclical loads imposed by the Lorentz' force that cause deformation could eventually lead to failure of components by fatigue. Therefore, testing of the fatigue properties for EBM-fabricated niobium is also recommended.
- Another recommendation is to ensure the connections to the nitrogen gas and prevent possible leaks of nitrogen from the glovebox environment along with the expedition of the powder recovery after a build is completed such that powder exposure to ambient elements as humidity is minimized.
- The obtained microstructure of EBM niobium with large average grain sizes in the horizontal direction and columnar grains in the vertical plane of reference might not be suitable for some SRF applications. Therefore, a recommendation for future work is to explore the recrystallization of EBM niobium parts by heat treatments and the measurement of SRF properties of these parts to see how they compare with as-fabricated EBM parts.
- Because of the powder “smoke” effect, some fabricated parts exhibited delamination and porosity. The use of hot isostatic pressing (HIPing) is recommended as a possible measure to reduce porosity in parts.
- As detailed in Chapter 4, powder overflow was traced as a root cause for warping of parts during fabrication using the IR camera setup. This relates to the uneven distribution of powder that might be caused by the excess material being moved during the rake step. Therefore, it is recommended that the regular fabrication method that includes the use of both hoppers and a triple raking strategy be implemented to prevent this effect.

References

- American Physical Society. 2007. APS News. Online. Vol. 16, No. 4.
<http://www.aps.org/publications/apsnews/200704/upload/Volume-16-Number-4.pdf>
- Arcam, Metal powders for EBM. Definitions and guidelines presentation. Presented by Ulf Ackelid. 2010
- ASM International. 1990. Metals Handbooks vol. 2: properties and selection, 10th ed. Metals Park, OH. Print.
- ASTM International. ASTM B212-09. Standard test methods for apparent density of free-flowing metal powders using the Hall Flowmeter Funnel. West Conshohocken, PA.
- ASTM International. ASTM B213-13. Standard test methods for flow rate of metal powders using the Hall Flowmeter Funnel. West Conshohocken, PA.
- ASTM International. ASTM B311-13. Standard test method for density of powder metallurgy (PM) materials containing less than two percent porosity. ASTM International. West Conshohocken, PA.
- ASTM International. ASTM B393. B10 Committee, 2009. Specification for Niobium and Niobium Alloy Strip, Sheet, and Plate. West Conshohocken, PA.
- ASTM International. ASTM standards E8/E8M. Standard test methods for tension testing of metallic materials. West Conshohocken, PA.
- ASTM International. ASTM E83-10a. Standard Practice for Verification and Classification of Extensometer Systems. West Conshohocken, PA.
- ASTM International. ASTM F2792-12a. F42 Committee, 2012. Terminology for Additive Manufacturing Technologies. West Conshohocken, PA.
- Aune, B., Bandelmann, R., Bloess, D., Bonin, B., Bosotti, A., et al., 2000. Superconducting TESLA cavities. Phys. Rev. ST Accel. Beams 3, 092001.
- Ayanda, O. S., Adekola, F. A., 2011. A Review of Niobium-Tantalum separation in hydrometallurgy. Journal of Minerals & Materials Characterization and Engineering. Vol. 10, No. 3. pp. 245-256
- Bardeen, J., Cooper, L.N., Schrieffer, J.R., 1957. Theory of Superconductivity. Phys. Rev. 108, 1175–1204. doi:10.1103/PhysRev.108.1175
- Bauer, W. 1980. SEAMLESS CAVITIES: the most creative topic in RF Superconductivity. Proceedings of the 1997 workshop on RF Superconductivity. Padova, Italy.
- Bednorz, J.G., Müller, K.A., 1986. Possible highT_c superconductivity in the Ba–La–Cu–O system. Z. Physik B - Condensed Matter 64, 189–193.
- Bieler, T. R., Wright, N. T., Pourboghrat, F., Compton, C., Hartwig, K. T., Baars, D., Zamiri, A., Chadrasekaran, S., Darbandi, P., Jiang, H., Skoug, E. Balachandran, S., Ice, G. E., Liu, W. 2010. Physical and mechanical metallurgy of high purity Nb for accelerator cavities. Physical Review Special Topics – Accelerators and Beams. 1.
- Champion, M.S., Cooley, L.D., Ginsburg, C.M., Sergatskov, D.A., Geng, R.L., Hayano, H., Iwashita, Y., Tajima, Y., 2009. Quench-Limited SRF Cavities: Failure at the Heat-Affected Zone. IEEE Transactions on Applied Superconductivity 19, 1384–1386.
- Chao, A., Tigner, M., 1999. Handbook of Accelerator Physics and Engineering. World Scientific Publishing. Singapore.

- Ciovati, G., Myneni, G. R., Morrone, M., Bundy, R., Clemens, B., Elliot, T., Slack, G., Turlington, L. 2007. A coaxial TE011 cavity and a system to measure DC and RF properties of superconductors. Proceedings of SRF 2007. Beijing, China.
- Compton, C., Bieler, T., Simkin, B., Jadhav, S., 2000. Measured properties of High RRR Niobium. National Superconducting Cyclotron Facility.
- Compton, C., Baars, D., Bieler, T., Bierwage, J., Bricker, S., Hartung, W., Pendell, D., York, R. 2007. Studies of alternative techniques for niobium cavity fabrication. Proceedings of SRF 2007. Beijing, China.
- Cooper, K.P., Minerals, M. and M.S., Materials Processing and Manufacturing Division, Minerals, M. and M.S., Meeting, S. on L.M.A.F. and P. (Eds.), 2000. Liquid metal atomization: fundamentals and practice: proceedings of a symposium held during the 2000 TMS Annual Meeting in Nashville, Tennessee, March 12-16, 2000. TMS, Warrendale, PA.
- Davis, J. R., 2000. ASM specialty handbook: nickel, cobalt, and their alloys. ASM International, Materials Park, OH. Print.
- Davis, J. R., 2004. Tensile Testing 1st ed. ASM International. Materials Park, OH. Print.
- Ding, X., Boucher, S., RadiaBeam Technologies, Berkeley. 2010. A method for establishing Q-factors for RF cavities. Proceedings of IPAC'10. Kyoto, Japan.
- Dinwiddie, R.B., Dehoff, R.R., Lloyd, P.D., Lowe, L.E., Ulrich, J.B., 2013. Thermographic in-situ process monitoring of the electron-beam melting technology used in additive manufacturing. p. 87050K–87050K–9.
- Eapen, B. Z., 2004. Combustion of aerosolized spherical aluminum powders and flakes in air. Thesis. New Jersey Institute of Technology.
- Entezarian, M., Allaire, F., Tsantrizos, P., Drew, R. a. L., 1996. Plasma atomization: A new process for the production of fine, spherical powders. JOM 48, 53–55.
- Gaytan, S. M., Murr, L. E., Ramirez, D. A., Machado, B. I., Martinez, E., Hernandez, D. H., Martinez, J. L., Medina, F., Wicker, R. B., 2011. A TEM study of cobalt-base alloy prototypes fabricated by EBM. Materials Sciences and Applications. 2, 355-363.
- German, R.M., 1996. Sintering theory and practice. 2nd ed. Wiley, New York. NY.
- Gibson, I., Rosen, D. W., and Stucker, B., 2009. Additive manufacturing technologies: rapid prototyping to direct digital manufacturing. Springer, New York, NY.
- Gupta, C.K., Suri, A.K., 1993. Extractive Metallurgy of Niobium. CRC Press. Boca Raton. FL
- Hardness Conversion Table for soft metals. Online. <http://www.gordonengland.co.uk/>. Accessed 4 April, 2014.
- Hernandez, J., Murr, L.E., Gaytan, S.M., Martinez, E., Medina, F., Wicker, R.B., 2012. Microstructures for Two-Phase Gamma Titanium Aluminide Fabricated by Electron Beam Melting. Metallogr. Microstruct. Anal. 1, 14–27.
- Kneisel, P., Palmieri, V., 1999. Development of seamless niobium cavities for accelerator applications, Proceedings of Particle Accelerator Conference, 1999. pp. 943–945 vol.2.
- Knobloch, J., 1997. Advanced Thermometry Studies of Superconducting Radio-Frequency Cavities. Dissertation. Cornell University
- Koethe, A., Moench, J. I. 2000. Preparation of ultra-high purity niobium. Materials Transactions. JIM. Vol. 41. No. 1. pp. 7-16
- Larsson et al., 2003. Rapid Manufacturing with Electron Beam Melting (EBM) – A manufacturing revolution? Proceedings of SFF 2003.

- Longuevergne, D., Gandolfo, N., Olry, G., Sagnac, H., Blivet, S., Martinet, G., Bousson, S., 2014. An innovative tuning system for superconducting accelerating cavities. *Nuclear Instruments and Methods in Physics Research Section A: Accelerators, Spectrometers, Detectors and Associated Equipment*. doi:10.1016/j.nima.2014.02.046
- Mahale, T. R., Cormier, D., Harryson, O., Ervin, K. 2007. Advances in electron beam melting of aluminum alloys. *Proceedings of SFF 2007*. Austin, TX USA
- Mahale, T.R. 2009. *Electron Beam Melting of Advanced Materials and Structures*, Ph. D. Dissertation. North Carolina State University.
- Mann, R., 2010. *An introduction to particle physics and the standard model*. CRC Press, Boca Raton. FL.
- Martinez, E., Murr, L. E., Hernandez, J., Pan, X. M., Amato, K., Frigola, P., Terrazas, C. A., Gaytan, S. M., Rodriguez, E., Medina, F., Wicker, R. B. 2013. Microstructures Niobium components fabricated by electron beam melting. *Metallogr. Microstruct. Anal.*
- Medina, 2013 *Reducing Metal Alloy Powder Costs for use in Powder Bed Fusion Additive Manufacturing: Improving the Economics for Production*, Ph. D. Dissertation. The University of Texas at El Paso
- “Metal Powders,” Arcam AB. <http://www.arcam.com/technology/products/metal-powders/>. Online. Accessed 20 Dec, 2013.
- Moffat, D., Barnes, P., Flynn, T., Graber, T., Hand, L., Hartung, W. Hayes, T., Kirchgessner, J., Knobloch, J., Noer, R., Padamsee H., Rubin, D., Sears, J. 1991. Studies on the nature of field emission sites. *Proceedings of the Fifth Workshop on RF Superconductivity*, DESY, Hamburg, Germany. pp. 245-284.
- Murr, L.E., 1975. *Interfacial phenomena in metals and alloys*. Addison-Wesley Pub. Co. Advanced Book Program, Reading, Boston. MA.
- Murr, L. E., Esquivel, E. V., Quinones, S. A., Gaytan, S. M., Lopez, M. I., Martinez, E. Y., Medina, F., Hernandez, D. H., Martinez, E., Martinez, J. L., Stafford, S. W., Brown, D. K., Hoppe, T., Meyers, W., Lindhe, U., Wicker, R. B., 2009. Microstructures and mechanical properties of electron beam-rapid manufactured Ti-6Al-4V biomedical prototypes compared to wrought Ti-6Al-4V. *Materials characterization*. 60, 96-105.
- Murr, L.E., Gaytan, S.M., Medina, F., Martinez, E., Martinez, J.L., Hernandez, D.H., Machado, B.I., Ramirez, D.A., Wicker, R.B., 2010. Characterization of Ti-6Al-4V open cellular foams fabricated by additive manufacturing using electron beam melting. *Materials Science and Engineering: A* 527, 1861–1868.
- Murr, L.E., Martinez, E., Pan, X.M., Gaytan, S.M., Castro, J.A., Terrazas, C.A., Medina, F., Wicker, R.B., Abbott, D.H., 2013a. Microstructures of Rene 142 nickel-based superalloy fabricated by electron beam melting. *Acta Materialia* 61, 4289–4296.
- Murr, L.E., Martinez, E., Pan, X., Meng, C., Yang, J., Li, S., Yang, F., Xu, Q., Hernandez, J., Zhu, W., Gaytan, S.M., Medina, F., Wicker, R.B., 2013b. Microstructures and properties of solid and reticulated mesh components of pure iron fabricated by electron beam melting. *Journal of Materials Research and Technology* 2, 376–385.
- Milberg, J., Sigl, M., 2008. Electron beam sintering of metal powder. *Prod. Eng. Res. Devel.* 2, 117–122. doi:10.1007/s11740-008-0088-2.
- Luther, Wolfgang. 2004. *Industrial application of nanomaterials – chances and risks*. Technology analysis. Future Technologies Division VDI. Germany.
- Niobium – high purity. *Matweb.com*. Online. <http://www.matweb.com>. Accessed 10 Jun, 2014.

- Padamsee, H., Knobloch, J., Hays, T., 1998. RF Superconductivity for Accelerators 2nd ed. Wiley. New York, NY. Print.
- Padamsee, H., 2001. The science and technology of superconducting cavities for accelerators. *Supercond. Sci. Technol.* 14, R28. doi:10.1088/0953-2048/14/4/202
- Palmieri, V. 1997. Fabrication of niobium cavities. Proceedings of SRF Workshop 1980. Karlsruhe, Germany.
- Posen, S., Liepe, M., 2012. Mechanical optimization of superconducting cavities in continuous wave operation. *Phys. Rev. ST Accel. Beams* 15, 022002.
- Ries, T., Fong, K., Koscielniak, S., Laxdal, R.E., Stanford, G., 2003. A mechanical tuner for the ISAC-II quarter wave superconducting cavities, in: Particle Accelerator Conference, 2003. pp. 1488–1490 vol.3. doi:10.1109/PAC.2003.1288570
- Ramirez, D. A., Murr, L. E., Martinez, E., Hernandez, D. H., Martinez, J. L., Machado, B. I., Medina, F., Frigola, P., Wicker, R. B., 2011. Novel precipitate-microstructural architecture developed in the fabrication of solid copper components by additive manufacturing using electron beam melting. *Acta Materialia*. 59. pp. 4088-4099.
- Rodriguez, E. 2013. Development of a thermal imaging feedback control system in electron beam melting. Master Thesis. The University of Texas at El Paso.
- Schwartz, M. 2012. Encyclopedia of Materials, Parts and Finishes, 2nd ed. CRC Press. Boca Raton, FL. Print.
- Singer, W., Brinkmann, A., Proch, D., Singer, X., 2003. Quality requirements and control of high purity niobium for superconducting RF cavities. *Physica C: Superconductivity* 386, 379–384.
- Singer, W., 2006. Seamless/bonded niobium cavities. *Physica C: Superconductivity* 441, 89–94.
- Singer, W., Ermakov, A., Singer, X. 2010. RRR-measurement techniques on high purity niobium. TTC Technical Report 2010-02.
- Sōmiya, S., 2013. Handbook of advanced ceramics materials, applications, processing, and properties, second edition. Academic Press, Waltham, Mass.
- Strondl, A., Fischer, R., Frommeyer, G., Schneider A., 2008. Investigations of MX and γ'/γ precipitates in the nickel-based superalloy 718 produced by electron beam melting. *Materials Science and Engineering. A480*, 138-147.
- USPAS. 2013. Brief introduction of RF superconductivity. Online. http://uspas.fnal.gov/materials/13Duke/SCL_Chap1.pdf
- Walsh, R.P., Mitchell, R.R., Toplosky, V.T. and Gentzlinger, R.C., “Low Temperature Tensile and Fracture Toughness Properties of SCRF Cavity Structural Materials,” Proc. of. 9th International Workshop on RF Superconductivity, Sante Fe, New Mexico, 1999, pp. 195-197.
- Wohlers Report 2009. Wohlers Associates. Fort Collins, CO.
- Wooten, J. and Dennies, D. P. Electron Beam Melting Manufacturing for Production Hardware. SAE International 2008, 08AMT-0061.
- Xu, F., Lv, Y., Liu, Y., Xu, B., He, P., 2013. Effect of Heat Treatment on Microstructure and Mechanical Properties of Inconel 625 Alloy Fabricated by Pulsed Plasma Arc Deposition. *Physics Procedia, International Federation for Heat Treatment and Surface Engineering (20th Congress)* 50, 48–54. doi:10.1016/j.phpro.2013.11.010
- Zah, M. F., Lutzmann, S., Kahnert, M., Walchshausl, F. 2008. Determination of Process Parameters for Electron Beam Sintering (EBS). Proc. of COMSOL Conference 2008. Hannover, Germany.

Appendix A: List of upgraded components for the Arcam A2 system

Table A-1- Components upgraded in Arcam A2 system.

	A1 Build Unit	
102366	Heatsink Cooling	1
102390	A1 BUILD TANK	1
102393	Powder Feeder System	1
102397	Rake Trap ASM	1
102427	Quadropod Insulation 250	1
102449	Sight Protection Shield A1	1
102461	Insulated Heat Shield A1/A2X	1
102473	Ceramic Rope Build Tank A1	1
102474	Ceramic Rope Powder Hopper	2
102589	High Temp Connection Box	1
103073	Powder sensor asm R	1
103074	Powder sensor asm L	1
201280	Powder niple	2
201658	Powder cup large	2
202369	A1 Shield Actuator	1
202379	Lower Fitting	1
202424	Rail Hopper Outside	2
202437	Rail Heat Shield and Hopper	2
422136	A4-brb-6_4x12x1_5.prt	2
440612	A4-MC6S-M6-12H	2
440650	A4-MC6S-M6-50	4
470812	A4-K6S-M8-12H	8
511995	Thermo Couple Connect Female	1
512086	Thermo Couple Connector Male	2
521061	Thermo couple	1.5
	A1 Linear Actuator	
102214	Ceramic Rope Rake Bearing	4
102285	Lubricated Rake bearing	4
102336	Axle mount actuator	2
201316	Shaft Linear Axle	2
201317	Linearvessel	1
201319	Tension mount	1
201320	Chain tensioner	2

201325	Coverplate	2
201649	Sensortrigger	1
422137	A4-brb-6_7x14x1_5.prt	4
440612	A4-MC6S-M6-12H	4
450612	A4-MF6S-M6-12H	4
203459	Drive chain 455RF 161 Links	1
200854	Cable cover	1
421835	Chain joint	1

Appendix B: Plots of linear region for stress-strain diagrams obtained from tensile testing experiments

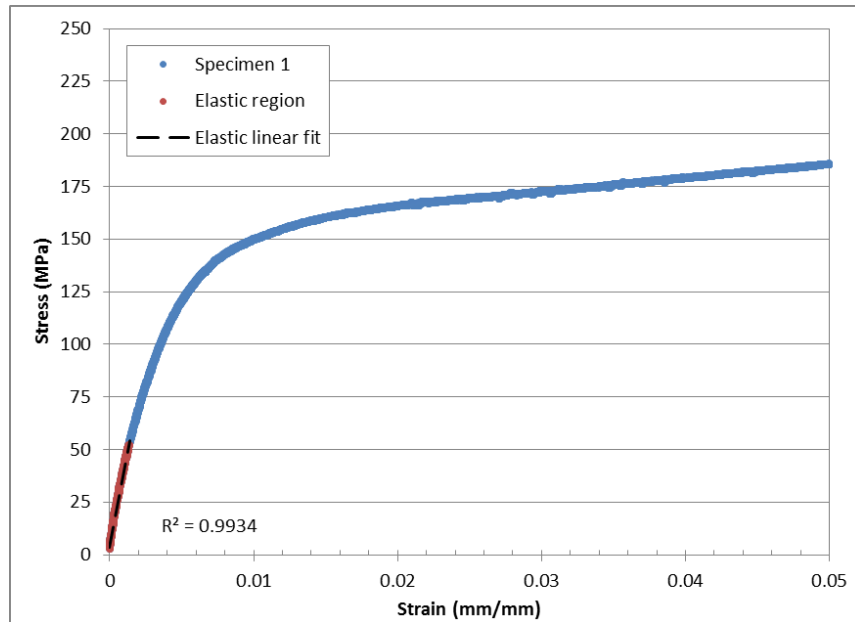


Figure B-1 – Linear region of stress-strain diagram for EBM1 specimen

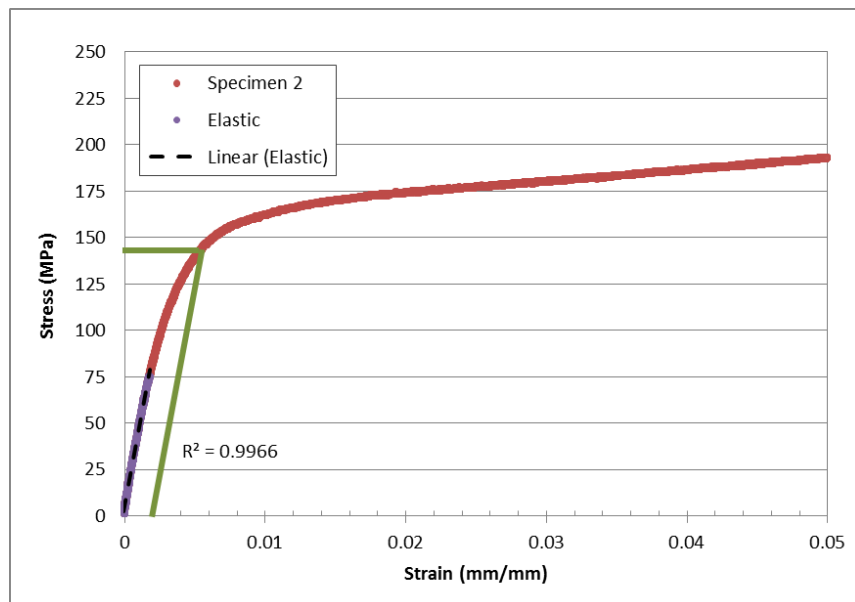


Figure B-2 – Linear region of stress-strain diagram for EBM2 specimen

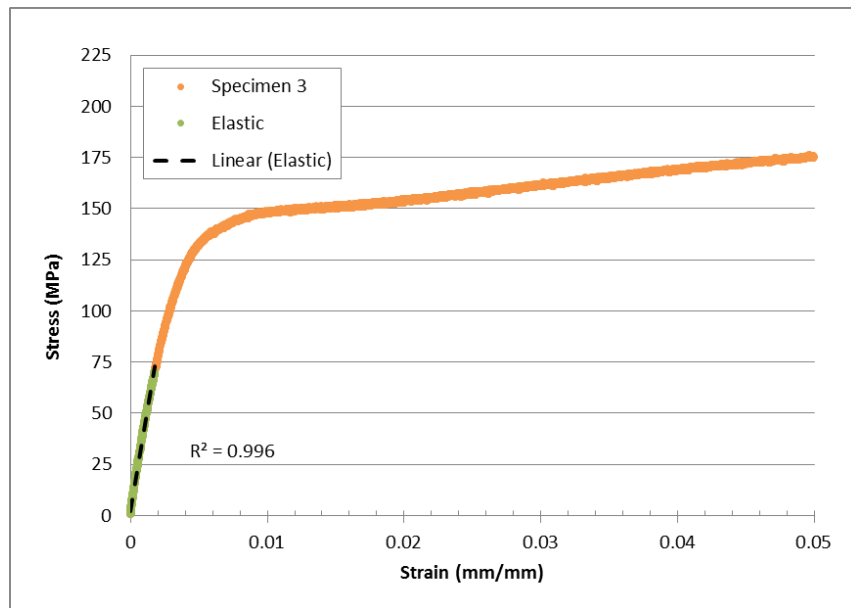


Figure B-3 – Linear region of stress-strain diagram for EBM3 specimen

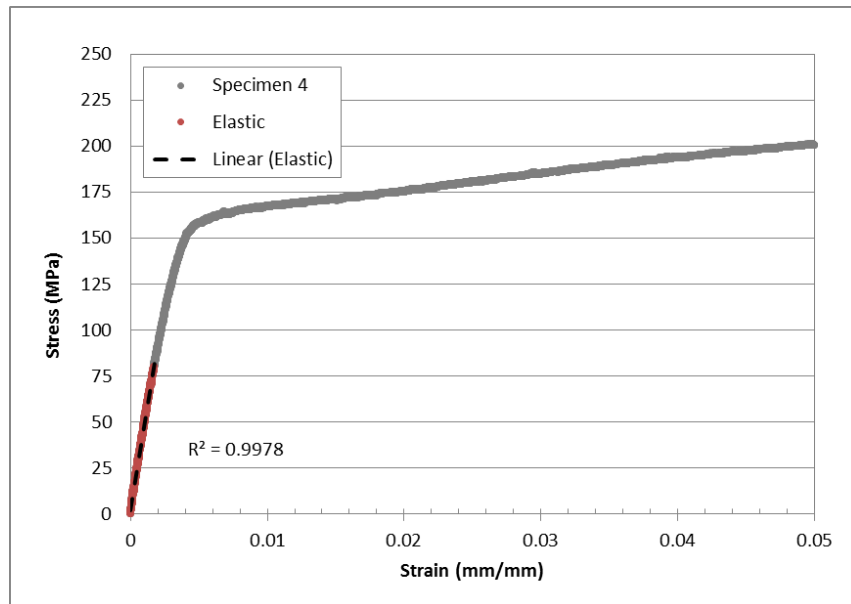


Figure B-4 – Linear region of stress-strain diagram for EBM4 specimen

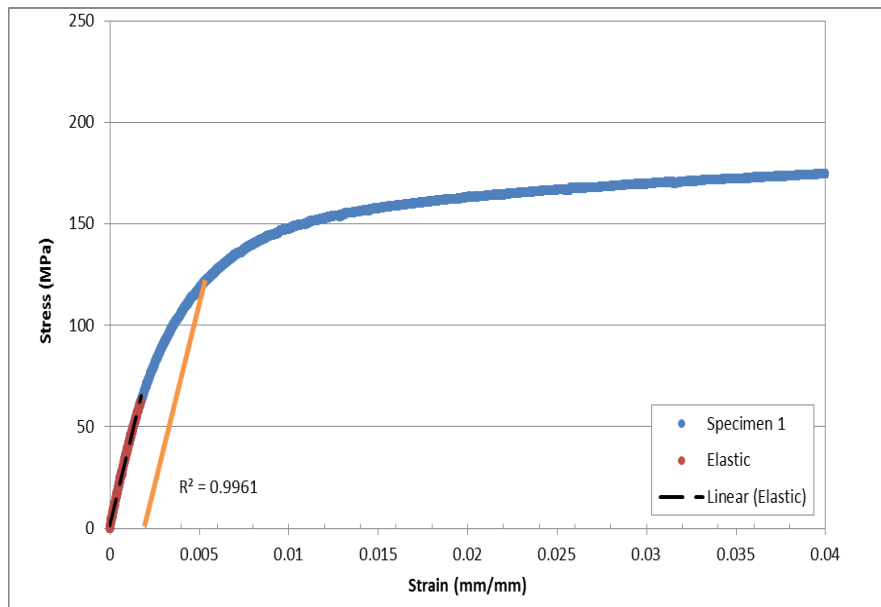


Figure B-5 – Linear region of stress-strain diagram for WRG1 specimen

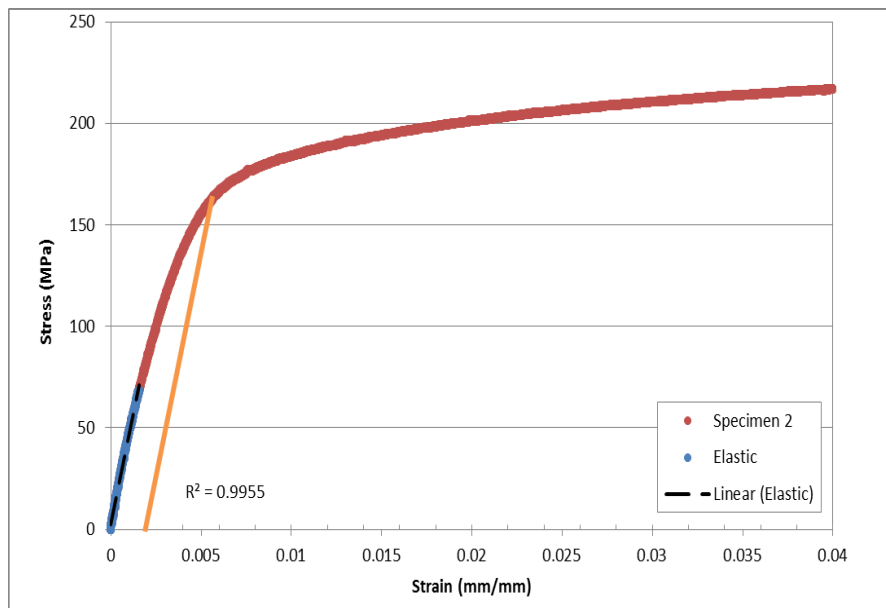


Figure B-6 – Linear region of stress-strain diagram for WRG2 specimen

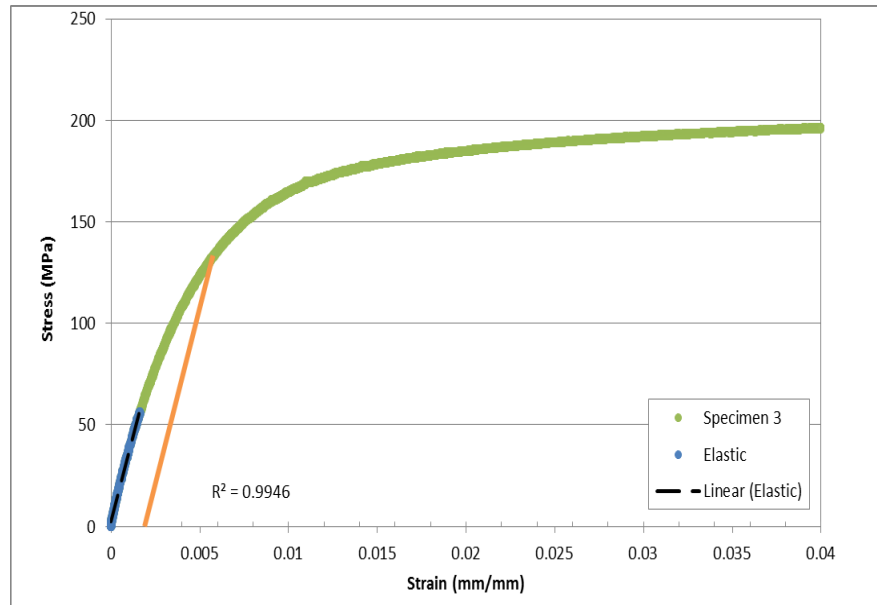


Figure B-7 – Linear region of stress-strain diagram for WRG3 specimen

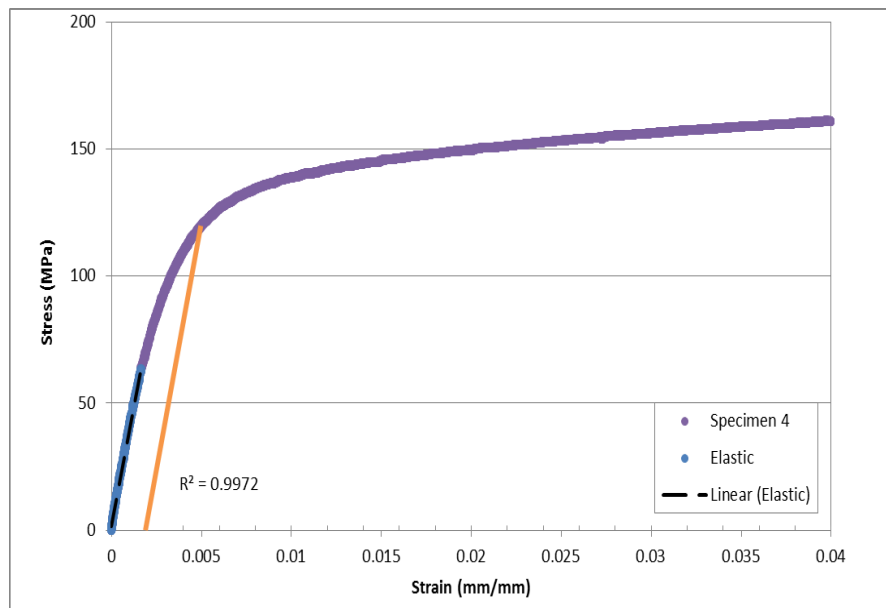


Figure B-8 – Linear region of stress-strain diagram for WRG4 specimen

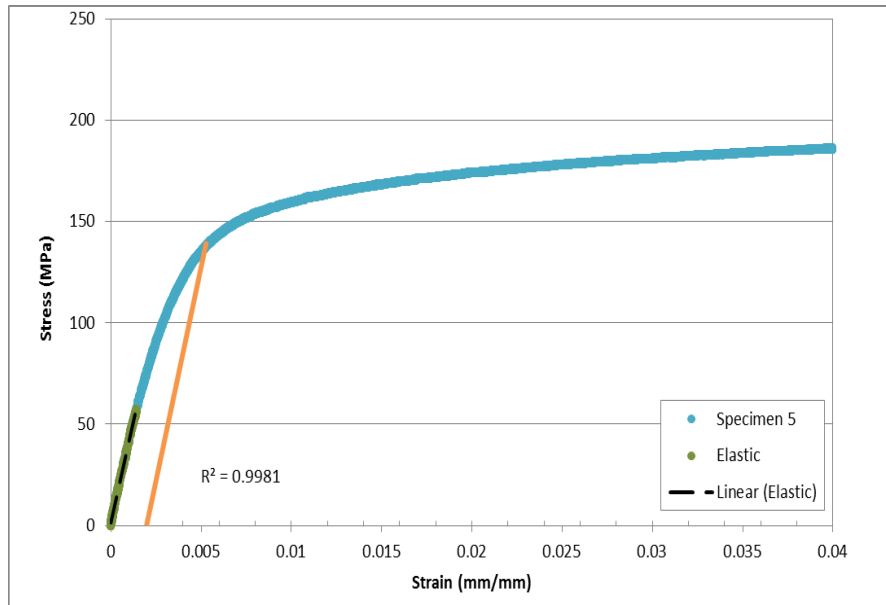


Figure B-9 – Linear region of stress-strain diagram for WRG5 specimen

Appendix C: Grid of parameters explored for densification of EBM niobium and measured values of apparent and relative densities

Table C-1 – Fabrication parameters and density measurements for Experiment # 1

Part	Focus offset (mA)	Average current (mA)	Beam Speed (mm/s)	W-air (g)	W-water (g)	Apparent Density (g/cm ³)	% RD
1	31	20	170	7.312	6.431	8.477	98.9
2	33	20	170	7.289	6.399	8.211	95.8
3	35	20	170	7.647	6.692	8.100	94.5
4	31	18	165	7.080	6.206	7.998	93.3
5	33	18	165	7.054	6.165	8.177	95.4
6	35	18	165	7.333	6.409	7.856	91.7
7	31	16	160	7.069	6.183	8.003	93.4
8	33	16	160	6.997	6.103	7.968	93.0
9	35	16	160	7.335	6.386	7.886	92.0

Table C-2 – Fabrication parameters and density measurements for Experiment # 2

Part	Focus offset (mA)	Average current (mA)	Beam Speed (mm/s)	W-air (g)	W-water (g)	Apparent Density (g/cm ³)	% RD
1	30	20.5	172.5	11.563	10.195	8.436	98.43
2	31	20.5	172.5	11.307	9.952	8.328	97.18
3	30.5	20.5	172.5	11.615	10.233	8.388	97.87
4	30	20	170	11.401	10.065	8.517	99.38
5	31	20	170	11.048	9.755	8.527	99.50
6	30.5	20	170	11.301	9.974	8.499	99.17
7	30	21	175	11.504	10.149	8.473	98.87
8	31	21	175	11.275	9.936	8.404	98.06
9	30.5	21	175	11.668	10.277	8.371	97.68

Table C-3 – Fabrication parameters and density measurements for Experiment # 3

Part	Focus offset (mA)	Average current (mA)	Beam Speed (mm/s)	W-air (g)	W-water (g)	Apparent Density (g/cm3)	%RD
1	31	18.5	168	8.941	7.895	8.536	99.60
2	31	19	168	8.678	7.643	8.373	97.70
3	31	19.5	168	8.739	7.713	8.506	99.25
4	31	18.5	170	8.968	7.915	8.505	99.24
5	31	19	170	8.643	7.621	8.445	98.54
6	31	19.5	170	8.916	7.836	8.244	96.20
7	31	18.5	172	9.390	8.293	8.548	99.74
8	31	19	172	9.223	8.133	8.450	98.60
9	31	19.5	172	9.405	8.292	8.438	98.47

Table C-4 – Density measurements for five sections of EBM square bar using the best fabrication parameters from previous experiments

Piece #	W-air (g)	W-water (g)	Apparent Density (g/cm3)	%RD
1	13.225	11.684	8.535	99.6
2	13.290	11.744	8.560	99.9
3	11.469	10.156	8.565	99.9
4	12.421	10.980	8.561	99.9
5	12.891	11.391	8.526	99.5

Curriculum Vita

César Terrazas was born on January 23, 1985, in Cd. Juárez, Chihuahua, México to José Miguel Terrazas and Araceli Nájera. He studied all his education from elementary to high school in Cd. Juárez, attending Colegio de Bachilleres 5 prior to joining The University of Texas at El Paso from where he received a Bachelor of Science in Mechanical Engineering in 2008. He also received his Master of Science in Mechanical Engineering from the same institution in 2010. Starting in 2011, he started doctoral studies in Materials Science and Engineering at The University of Texas at El Paso as well. During the time as a doctoral student, César joined the W. M. Keck Center for 3D Innovation as a research assistant where he focused his research on developing processing parameters for metallic materials to be used in the additive manufacturing process of electron beam melting. Also, during this time he taught an undergraduate class in engineering dynamics at the El Paso Community College campus Valle Verde.

Research performed by Cesar at the Keck Center was presented at the Solid Freeform Fabrication Symposium and it was also published in the International Journal for Advanced Manufacturing Technologies.

César worked on his dissertation topic, Characterization of High-purity Niobium Structures Fabricated using the Electron Beam Melting Process, under the direction of Dr. Ryan Wicker. Upon finishing his doctoral degree, César will join a spin-off company located in Hartford, CT within the additive manufacturing sector where he will be involved in all matters related to engineering. There, he will continue to research materials to be processed by the electron beam melting process including superalloy materials for use in aerospace applications.

Permanent Address:

Yautepec 1823 sur. Colonia Cuernavaca. Cd. Juárez, Chih. México. CP 32510

This dissertation was typed by César Adrián Terrazas Nájera.